Failure Due to Delamination in Composite Structures with Ply-drops

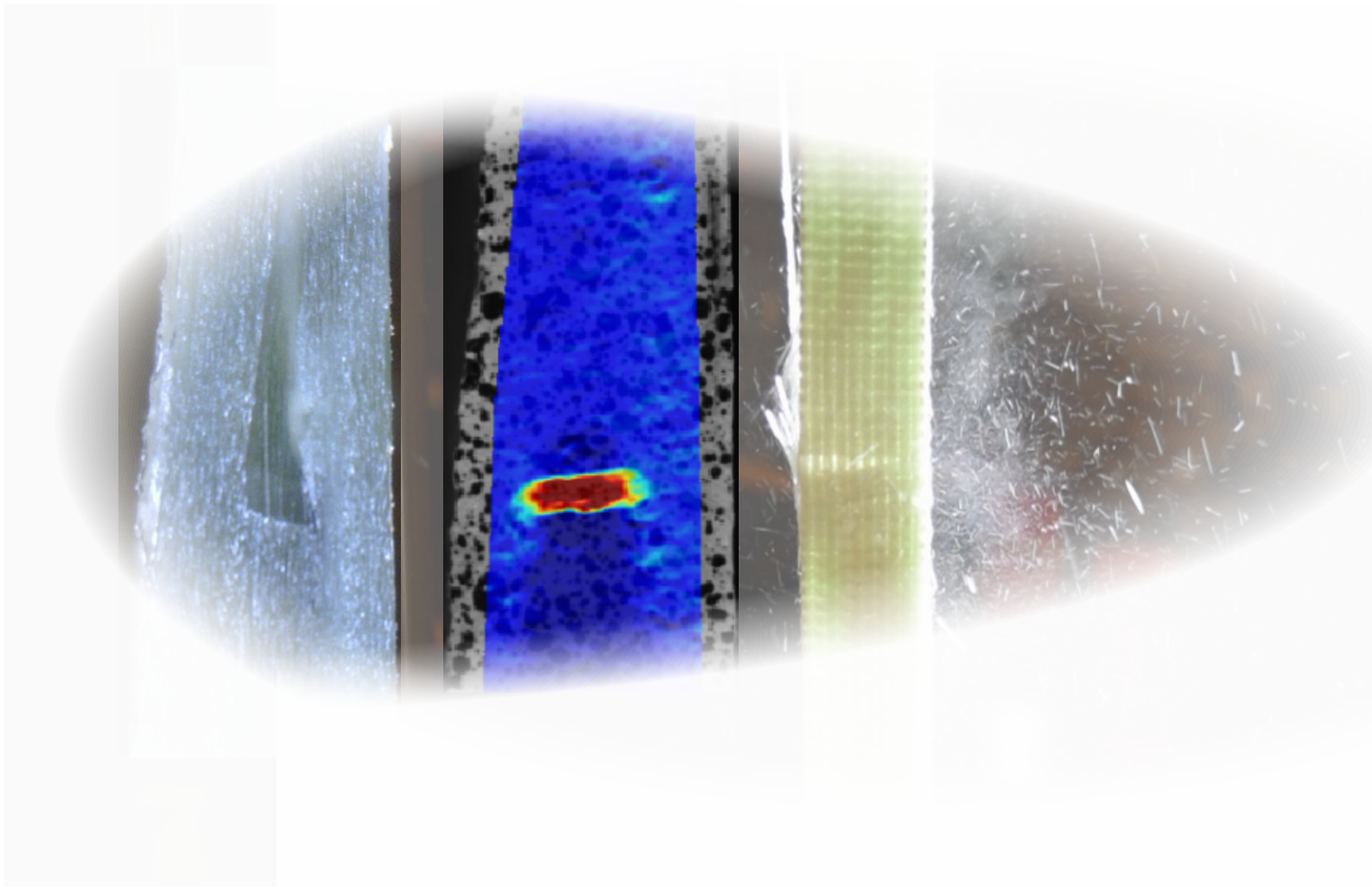

Jakob Bisgård Jensen
Søren Rindom Andersen

Master's thesis
Design of Mechanical Systems
Aalborg University
1st June 2016

AALBORG UNIVERSITY

STUDENT REPORT

Study Board of Industry and Global Business Development
Fibigerstræde 16
DK - 9220 Aalborg øst
Phone: +45 99 40 93 09
Mail: lft@m-tech.aau.dk
Web: www.en.ses.aau.dk

Title: Failure Due to Delamination in Composite Structures with Ply-drops

Project period: Spring 2016

ECTS: 30 per student

Supervisor: Johnny Jakobsen

Projectgroup: DMS4 - Pon103/3.116X

Participants:

Jakob Bisgård Jensen

Søren Rindom Andersen

Number of copies: 3

Number of pages: 90

Appendix: 4

Completed: 01-06-2016

Synopsis:

Lack of knowledge on how ply-drops affect the strength of a laminate means that laminated composite structures usually are oversized. The goal of this master's thesis is to develop a model for predicting failure of laminates with ply-drops.

The project is initiated with a experimental study on failure of laminates with ply-drops.

The model is created in the context of the finite element method combined with linear elastic fracture mechanics.

A geometrical non-linear finite element model with linear elastic materials is created and is then validated using digital image correlation. The model is then extended using the finite crack extension method.

When comparing the model results with experimental data similiar crack growth is observed in the thick section of the ply-drop this is however not the case in the thin section. The comparison also shows similiar failure loads.

Resumé

Dette kandidatspeciale omhandler modellering af ply-drops i laminerede fiber kompositter. Modelleringen sker med henblik på at bestemme brudstyrken af et laminat, som indeholder et ply-drop. Forud for modelleringen udføres eksperimentielt arbejde for at opnå viden omkring, hvor og hvordan et laminat indeholdende et ply-drop fejler. Med denne viden kan modelleringen fokusere på de effekter, som er observeret under forsøgene og dermed opnå en så simpel model som muligt.

Det eksperimentielle arbejde indledes med fremstilling af test emner i forskellige konfigurationer afhængig af formålet. Der fremstilles laminater til både enakset træk og tryk til bestemmelse af brudstyrke og revnevækst ved både statiske og udmattelses laster. Revnevæksten monitoreres ved hjælp af et USB mikroskop. Under både de statiske og udmattelses forsøgene indlægges pauser således, at der kan tages et billede med USB mikroskopet. Forsøgene indikerer, at delaminering er styrende for udvikling af skade i laminaterne. Skades initieringen er dog afhængig af last situationen, om emnet er lastet statisk eller i udmattelse.

Som en del af det eksperimentielle arbejde foretages også en undersøgelse af geometrien af et laminat indeholdende et ply-drop med henblik på modellering af geometrien.

Før modelleringsarbejdet påbegyndes undersøges lineær elastisk brudmekanik og hvordan denne kan håndteres i elementmetodeteorien. Herunder undersøges Finite Crack Extension Method (FCEM), Crack Closure Method (CCM) og Virtual Crack Closure Technique (VCCT).

Selve modelleringsarbejdet deles op i to dele. I den første del modelleres geometrien i en forsimplet udgave fordi geometrien omkring ply-droppet varierer mellem emner skåret af den samme plade. Det elastiske respons sammenlignes med resultater opnået ved hjælp af Digital Image Correlation (DIC) for at validere både geometrien og de elastiske materiale parametre. Det

viser sig, at modellen afviger fra DIC-resultaterne. På grund af ønsket om at bevare den forsimplede geometri anvendes invers modellering og en acceptabel afvigelse mellem model og målinger opnås.

I den sidste del af modelleringsarbejdet implementeres brudmekanikken i modellen. Først afprøves VCCT, da den metode foruden energifrigørelsesgraden også beregner mode mixitien. Det viser sig dog, at VCCT ikke kan anvendes, da der på grund af bi-materiale grænsefladen opstår oscillerende spændinger omkring revnespidsen. Af samme grund afprøves CCM ikke fordi den ligesom VCCT er baseret på lokale værdier. Som det næste afprøves FCEM, som i modsætning til VCCT kun beregner energifrigørelsesgraden, men da den er baseret på globale værdier, er den ikke følsom overfor de oscillerende spændinger. Den kritiske energifrigørelsesgrad afhænger af mode mixitien hvorfor VCCT, til trods for problemerne, anvendes i kombination med FCEM.

Når modellen sammenlignes med forsøgsresultaterne ses at revnevæksten i den tykke ende af ply-drop stemmer overens. Dette er dog ikke tilfældet i den tynde ende af ply-droppet. Fejlen i den tynde ende tilskrives den forsimplede geometri. Ydereligere sammenligning viser at modellen forudsiger brudlasten 10% lavere end den målte.

Preface

This Master's thesis documents the work performed by the two authors during the last semester of the Master's programme "Design of Mechanical Systems" at Aalborg University. The thesis covers a workload of 30 ECTS per author making a total workload of 60 ECTS.

LM Wind Power has supplied glass fibre and polyester-resin for the experimental part of the project.

A special thanks is directed to Ph.D student Jens Ammitzbøll Glud and Ph.D student Seyed Aydin Raeis Hosseiny for giving useful inputs and suggestions to the project.

Reading Guidelines:
References to litterature is in the report given as a number encapsulated in square brackets. Each number corresponds to an entry in the bibliography at the end of the report before the appendix.

References to figures and tables are given as two numbers seperated by a dot. The first number indicate the chapter in which the figure or table is located. The second number is a sequential number for the chapter.

References to equations follow the same approach as for figures and tables except that the reference is encapsulated in parentheses.

Contents

1 Introduction

Laminated fibre composites are ideal for structures that requires high strength and low weight such as wind turbine blades and aeroplanes. This is due to a superior strength and stiffness to weight ratio when comparing with traditional metallic materials [1]. Another advantage of laminated fibre composites is the tailoring capabilities which allows for adding stiffness in the directions needed.

Theory regarding neat laminates is well-founded but theory with respect to details, such as load introductions, mechanical joints and change in thickness, is lacking. The lack of theory means that laminated composite structures is oversized. If the blades of a wind turbine are oversized the hub and tower will increase in size, which is unfavourable from an economical point of view.

The loads affecting a structure is usually not evenly distributed throughout the structure. This means that different material thicknesses are needed in the structure. The thickness change in laminated composite structures is achieved by creating a ply-drop (see figure 1.1). A ply-drop is a termination of a ply.

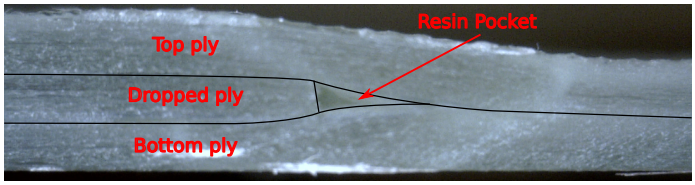

Figure 1.1: Picture of a ply-drop.

The notation used in this project to describe different ply-drop configurations is, as shown in figure 1.2, n_{bot}-n_{drop}-n_{top}.

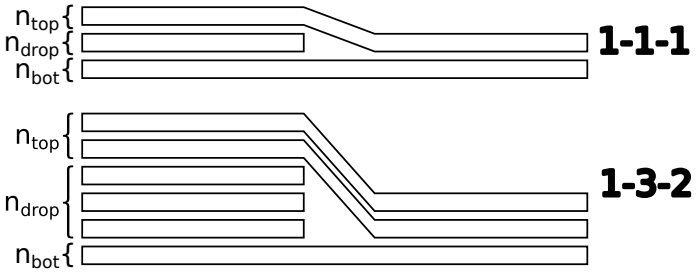

Figure 1.2: Two different ply-drop configurations.

Figure 1.3 shows experimentally obtained load-displacement curves for two different ply-drop configurations. From figure 1.3 it is seen that the failure load is higher for the 1-1-1 ply-drop. This is dispite the 1-3-2 ply-drop having more continuous plies. This indicates that a ply-drop has a negative effect on the laminate. The goal of this project is therefore to develop a model that can be used to predict failure of a ply-drop.

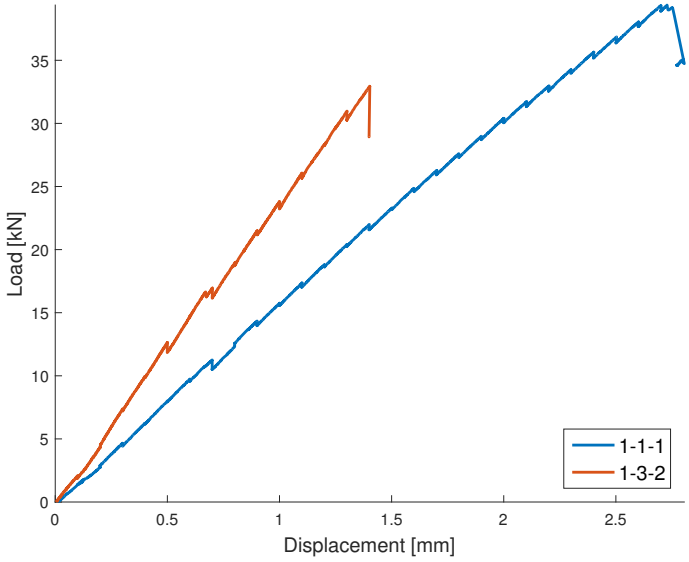

Figure 1.3: Load displacement curves for two different ply-drop test specimen configurations.

Experimental Characterisation of Failure in Ply-drops in Static Tension

2

When creating models knowledge about the physics, geometry and loads is needed for a model to be able to display the correct behavior. However the physics with respect to failure in composite structures is a complicated matter. According to the European Space Agency [2] twelve different failure modes exists. It is not feasible to model and evaluate all of these failure modes in one single simulation. Experiments are therefore needed to determine the failure modes, the sequence of failure modes and where failure occurs. Furthermore will experiments provide benchmark values for evaluating the accurarcy of the model such as failure load and any occuring crack growth.

This chapter will first describe the manufacturing process for the test specimens followed by an examination of the specimen geometry which will aid the modelling. Next a failure hypothesis for a ply-drop in static tension is developed. The failure hypothesis is then used to help plan the experiments such that measurements are performed in the areas where failure is likely to occur. Lastly the experiments are evaluated to obtain the needed information: failure modes, failure sequence and location of failure.

2.1 Manufacturing of Test Specimens

Wind turbine blades are according to Lund and Overgaard [3] produced with the process called vacuum assisted resin transfer moulding (VaRTM). This and the fact that Aalborg University has the necessary equipment for VaRTM means that the specimens are manufactured using this process.

The glass fibre mat weighs approximately 1.4 $\left[\mathrm{kg/m^2}\right]$ per square meter. The measurement details are seen in appendix A. To keep the fibres together the mat has backing fibres in the 90°-direction. Therefore the fibre mat is having a front and back. The front of the mat is showed in figure 2.1 and the back in figure 2.2.

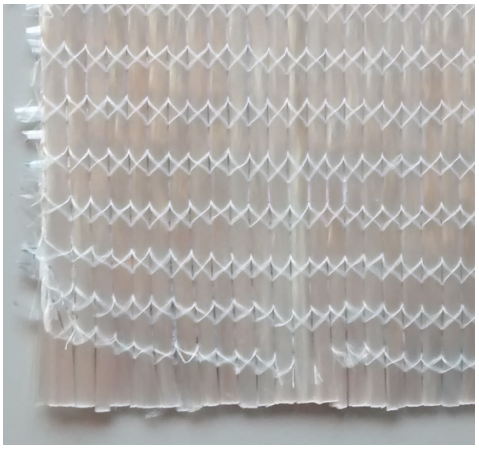

Figure 2.1: Front of the mat.

Figure 2.2: Back of the mat with backing fibres.

The resin is a polyester called Polylite 413-577 and the hardener is called NOROX MCP-75. The mixture used for all the infusions are 2% hardener to polyester. This results in a pot life of at least one hour. All produced specimens are cured at least 24 hour at 20°C.

2.1.1 Manufacturing of Plates

This section describes the manufacturing procedure used in this project.

1. Cut out the different materials needed for the infusion process. The sizes of each material are specified in appendix B
2. Prepare a aluminium plate with slip foil as shown in figure 2.3. The slip foil on the plate can be reused for several infusions.

Figure 2.3: Aluminium plate with slip foil.

3. First, place one layer of butyl-band around the slip foil as shown in figure 2.4 and press it unto the aluminium plate to ensure an airtight seal. Butyl-band is a rubber band with adhesive on both sides, which is used to repair air leaks or as an airtight gasket between plates.

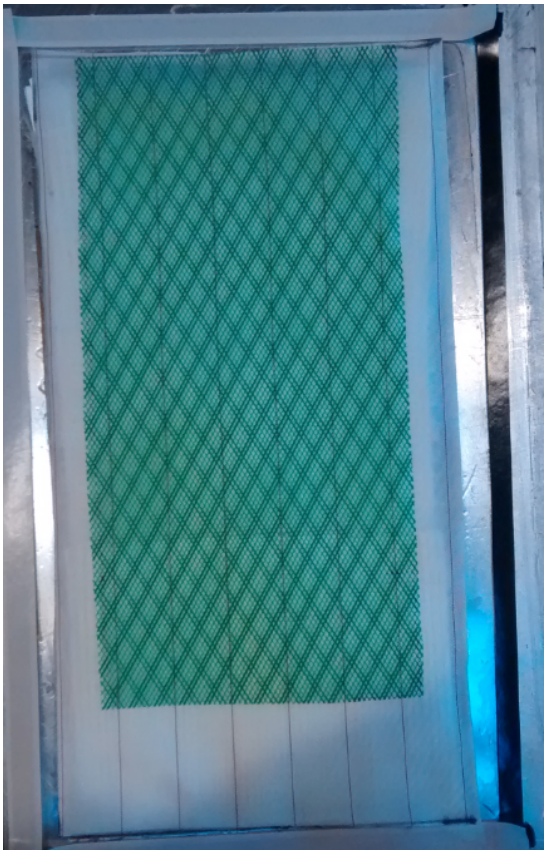

Figure 2.4: Aluminium plate with slip foil, one layer of butyl, fibre mats, peel ply and distribution medium.

4. Cut off a tube for both the inlet and outlet. The ends of the tubes to be positioned inside the infusion chamber must be prepared by wrapping the end with 2-3 layers of butyl as shown in figure 2.5. A piece of distribution medium is inserted into the end of the tube. The distribution medium must be long enough to ensure contact from the tube to the distribution medium as shown in figure 2.6 for the inlet tube. For the outlet tube the piece of distribution medium has to be long enough to make contact with the peel ply as shown in figure 2.7.

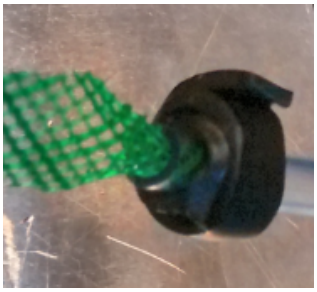

Figure 2.5: Tube with butyl wrapped around the end and distribution medium inserted into the tube opening.

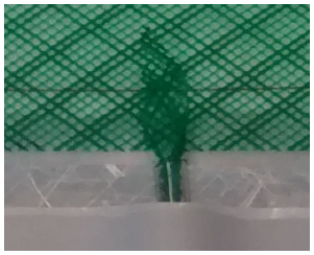

Figure 2.6: The inlet tube connected to the distribution medium and peel ply.

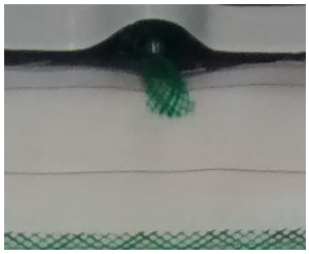

Figure 2.7: The outlet tube distribution medium in contact with the peel ply.

5. Attach the tube to the first layer of butyl and apply another layer on top. The region around a tube is shown in figure 2.8.

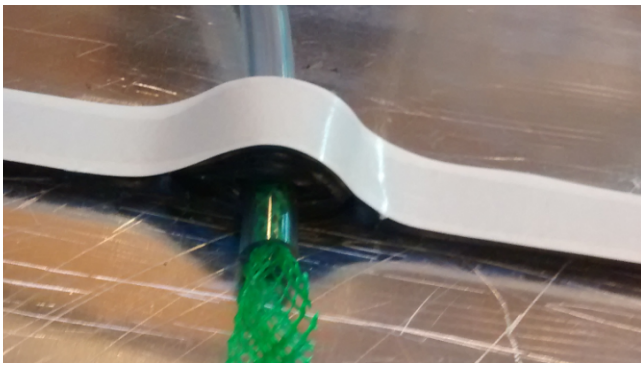

Figure 2.8: The region around a tube with the second layer of butyl.

6. Attach the vacuum bag to the butyl to make the infusion chamber airtight. A vacuum bag is attached to the second layer of butyl is shown in figure 2.9.

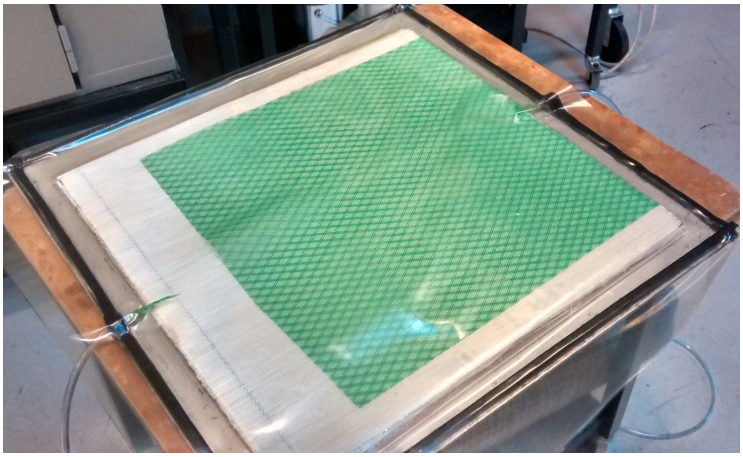

Figure 2.9: Vacuum bag attached to butyl.

7. Prepare for the vacuum test by attaching the outlet tube to the vacuum pump, as shown in figure 2.10, and the inlet tube to the vacuum gauge as shown in figure 2.11.

Figure 2.10: Outlet tube attached to the vacuum pump.

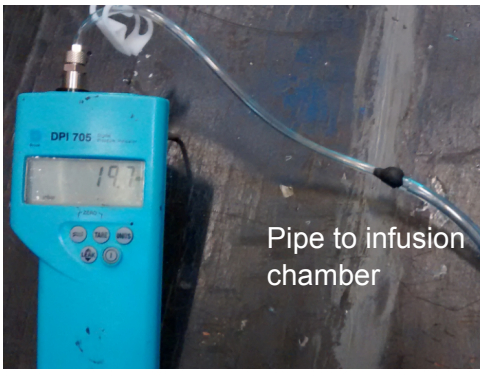

Figure 2.11: Inlet tube attached to the pressure gauge.

8. Perform a vacuum test by bringing the pressure under 25 [mbar] and

then block the tube connected to the vacuum pump. The test is passed if the pressure rises less than 5 [mbar] after 5 minutes.

9. The resin without the hardener is poured into a cup and degassed. The cup with resin inside the degassing chamber is shown in figure 2.12. The resin is degassed to minimize the void content.

Figure 2.12: Degassing chamber.

10. The outlet tube is raised to have a high point 700 mm above the infusion chamber. This is done as shown in figure 2.13. The 700 mm are chosen because of a clamp in the workshop results in this length. Different lengths could have been chosen. It has to be the same length for every plate to ensure similar plates. The high pointing is done to ensure no air travels back into the infusion chamber when the tube are closed.

Figure 2.13: High point of the tube.

11. The hardener is added to the degassed resin and stirred carefully until a homogeneous liquid is obtained.
12. The resin is sucked through the infusion chamber while a technician controls the inlet ensuring air is removed from the chamber. Figure 2.14 shows how the inlet is controlled.

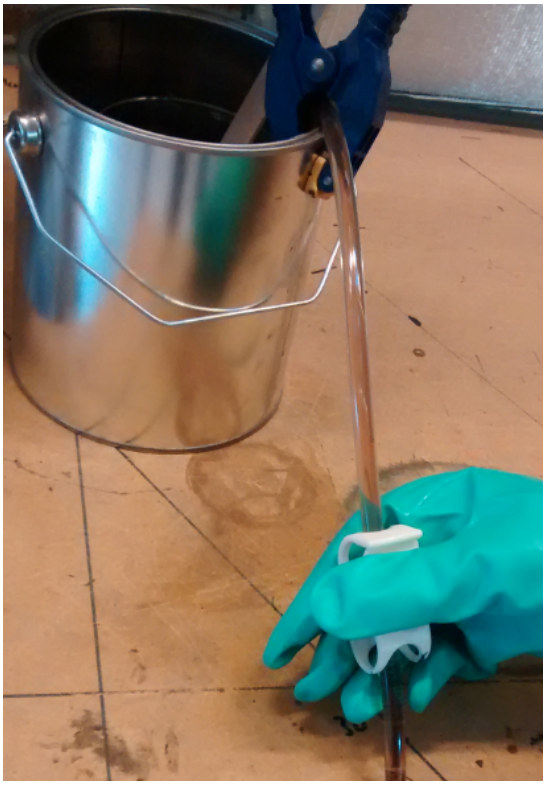

Figure 2.14: Inlet control.

13. The vacuum is kept at full pump capacity which is around 20 mbar (denoted as 100% vacuum) until the resin reaches the high point of the outlet tube then the vacuum pump is adjusted to 60%. This causes the resin to retreat back through the tube. This is shown in figure 2.15 and 2.16

Figure 2.15: Vacuum pump at 100% and resin at high point.

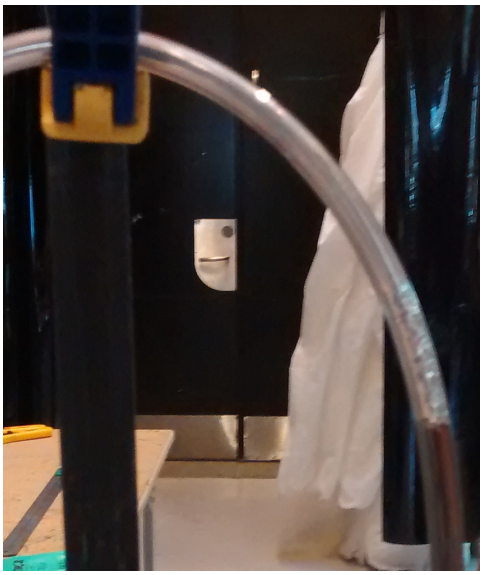

Figure 2.16: Vacuum pump at 60% and resin lower than figure 2.15

14. The inlet tube is closed.
15. When the resin again reaches the high point of the tube as shown in figure 2.15 the outlet tube is closed. Because the inlet tube is closed this step will determine the fibre volume fraction since resin is removed from the infusion chamber. If the outlet tube is closed immediately after the inlet tube the fibre volume fraction will be minimized for this set-up. If the outlet tube is never closed the fibre volume fraction will will be maximized for this set-up.
16. The plate is cured at least 24 hours at 20°C.
17. The peel ply is stripped from the plate and the plate can be cut into specimens.
18. Inlet and outlet side are marked on the plate.

2.1.2 Preparation of Specimens

Before the plate can be cut into test specimens a line, the "0-line", parallel with the fibres is drawn. This ensures that fibres in the specimens are aligned with the specimen length direction. A 0-line is shown in figure 2.17. The

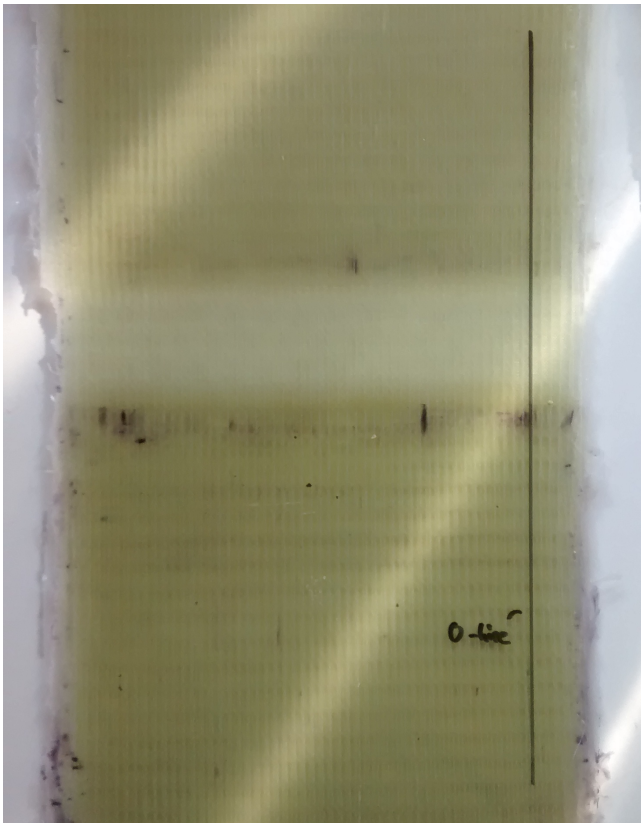

Figure 2.17: 0-line and non-aligned fibres.

plate is trimmed to ensure only the neat laminate remains. Visual inspection is used to determine which sections of the rough plate that is unwanted. All cuts are made on a circular saw with a Hawera Supertec Ø250 vw 80 blade.

When cutting plates, fibre tear out has been observed in cases where the backing fibres are located outwards from the specimen as shown in figure 2.18. If the fibre tear out can not be avoided the specimens is abraded.

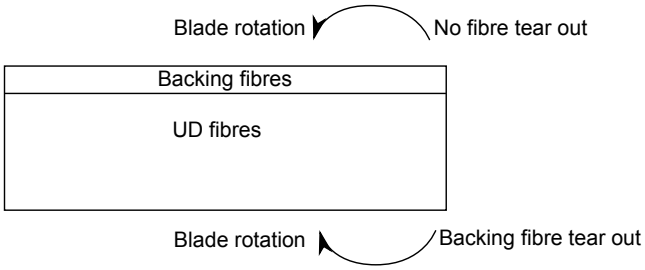

Figure 2.18: Cutting directions and resulting fibre tear out.

2.1.3 Plate for Material Tests

For determining the elastic material parameters a neat laminate plate is manufactured. The sizes of each infusion chamber layers is listed in appendix B. The layup of the fibres is shown in figure 2.19 and the layup of the infusion chamber is shown in figure 2.20.

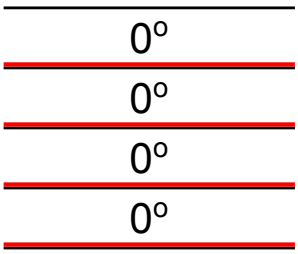

Figure 2.19: Layup of fibres the red denotes the backing fibre surface.

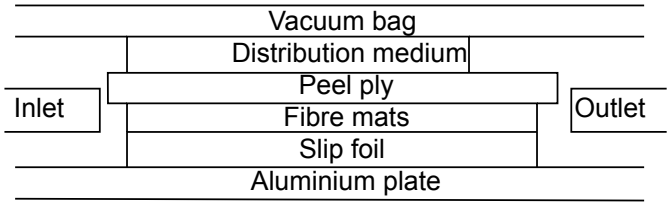

Figure 2.20: Infusion chamber layup of the material plate.

Calculation of Fibre Volume Fractions

To calculate the fibre volume fraction the inlet and outlet zones are weighed. The resin is then incinerated in an oven at 400°C and the remains are then reweighed. The fibre volume fraction is then calculated using equation (2.1), (2.2) and (2.3). The density for polyester ($\rho_{polyester}$) and glass (ρ_{glass}) is found in ESAComp material database [4].

$$m_{fiber} = m_{afterBurn} - m_{bucket} \tag{2.1}$$

$$W_f = \frac{m_{fiber}}{m_{specimen}} \tag{2.2}$$

$$V_f = \frac{W_f/\rho_{glass}}{W_f/\rho_{glass} + (1-W_f)/\rho_{polyester}} \tag{2.3}$$

For the material test plate the fibre volume fraction of the inlet is found to be 58.1% and 55.6% for the outlet. The data used for calculating the fibre volume fraction is found in appendix B.

2.1.4 Plate for Ply-drop Specimens

The plates for ply-drop specimens are 400 mm long and since the specimens are 200 mm long 100 mm at each end of the plate is used for the fibre volume fraction calculation. The layup of the plates are shown in figure 2.21, 2.22 and 2.23. Each plate is associated with an identifier which is found in the caption of the figure. The sizes of each infusion chamber layers are listed in appendix B. The layup of the infusion chamber is shown in figure 2.20. The fibre volume fractions for the ply-drop plates are listed in table 2.1.

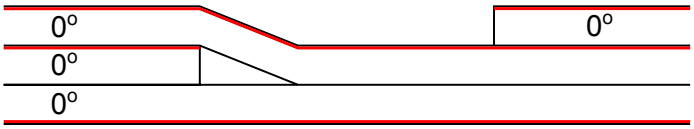

Figure 2.21: Layup of fibres of the ply-drop plate 1-1-1 130316, the red denotes the backing fibre surface.

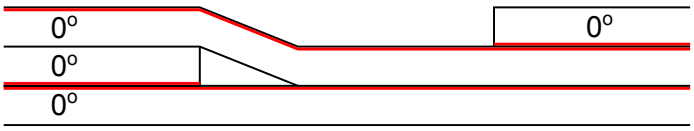

Figure 2.22: Layup of fibres of the ply-drop plate 1-1-1 120416 and 220416, the red denotes the backing fibre surface.

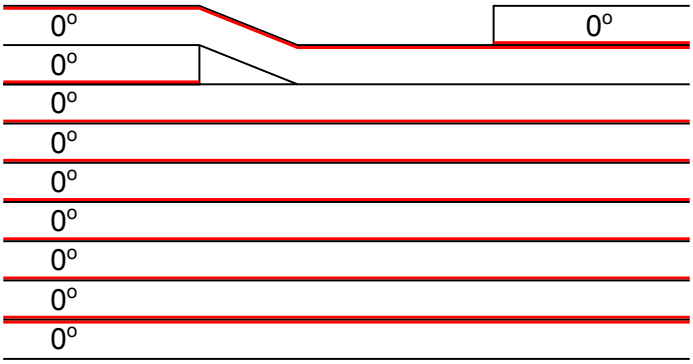

Figure 2.23: Layup of fibres of the ply-drop plate 7-1-1 230316 and 220416, the red denotes the backing fibre surface.

Identifier	V_f^{in}	V_f^{out}
1-1-1 130316	54.9 %	56.1%
7-1-1 230316	55.7 %	57.1 %
1-1-1 120416	55.1 %	54.3 %
1-1-1 220416	54.6 %	55.5 %
7-1-1 220416	56.5 %	57.9 %

Table 2.1: Fibre volume fractions for the ply-drop plates.

2.2 Geometry of a Ply-drop

To further examine the ply-drop a 1-1-1 specimen is studied in a microscope. This is done to study the different geometrical effects of backing fibres, stitches and the geometry of of the ply-drop. A microscope picture of the region around the ply-drop with notation of the different parts is shown in figure 2.24. The ply-drop consists of a thin and thick section and a resin pocket with no fibres where the dropped ply ends.

The fibre mats contains backing fibres resulting in different thicknesses in the laminate as shown in figure 2.25 and 2.26. In the thin section the thickness varies with 0.1 mm and in the thick section with 0.25 mm. The slip foil side is straight and the peel ply side consists of waves made by the peel ply.

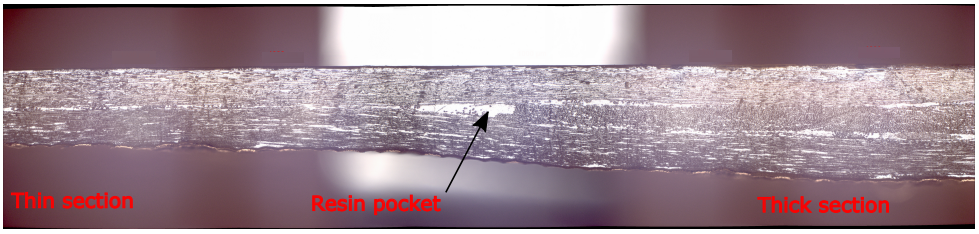

Figure 2.24: Microscope picture of the ply-drop with 2.5X magnification.

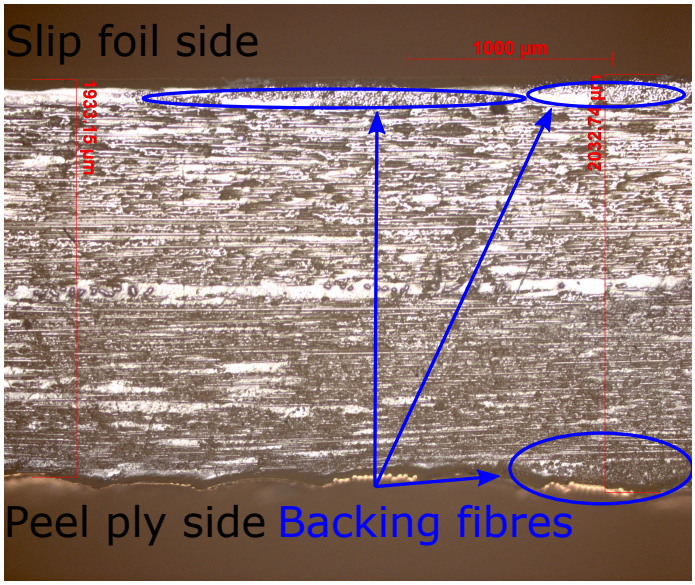

Figure 2.25: Thin section with 5X magnification.

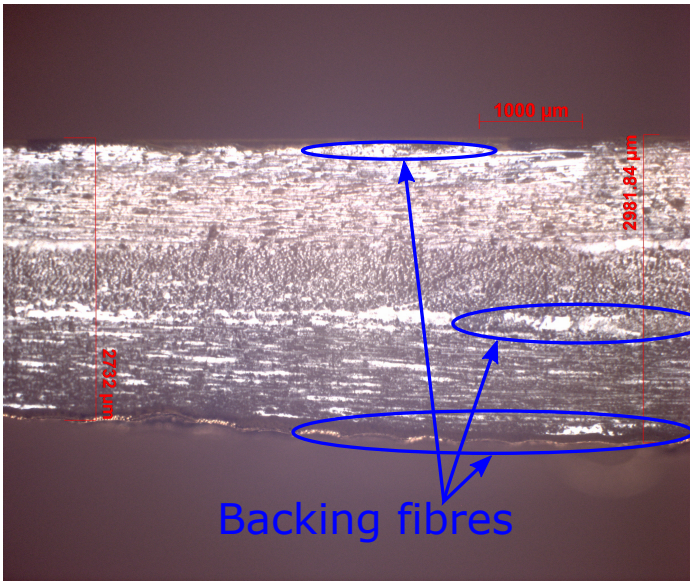

Figure 2.26: Thick section with 2.5X magnification.

The resin layer between two plies with no backing fibres, is shown in figure 2.27. The green circle marks the stitches in the mat.

A microscope picture of the resin pocket with measurements is shown in figure 2.28. Fibres are pulled into the resin pocket during manufacturing this is marked with blue in figure 2.28. It should be noted that the thickness of the dropped ply at the resin pocket is approximately 0.5 mm compared to the thickness of the plies which is approximately 0.9 - 1.0 mm depending on if it is measured with or without backing fibres. The length of the resin pocket is measured to be approximately 3.2 mm.

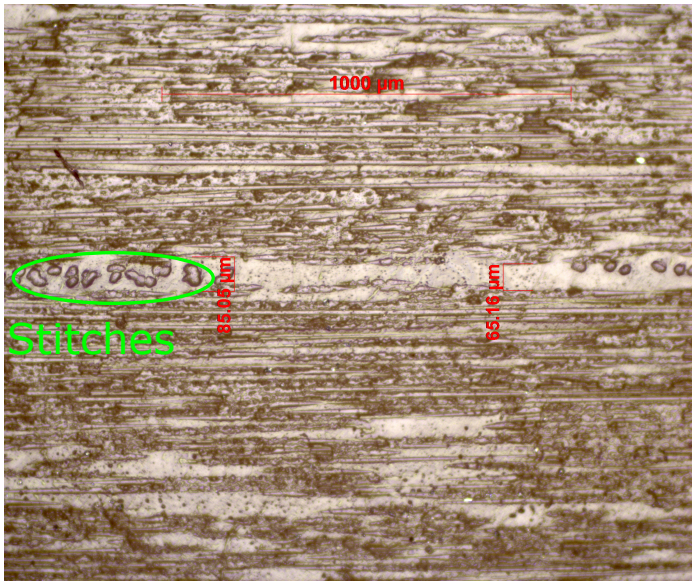

Figure 2.27: Resin layer in the thin section with 10X magnification.

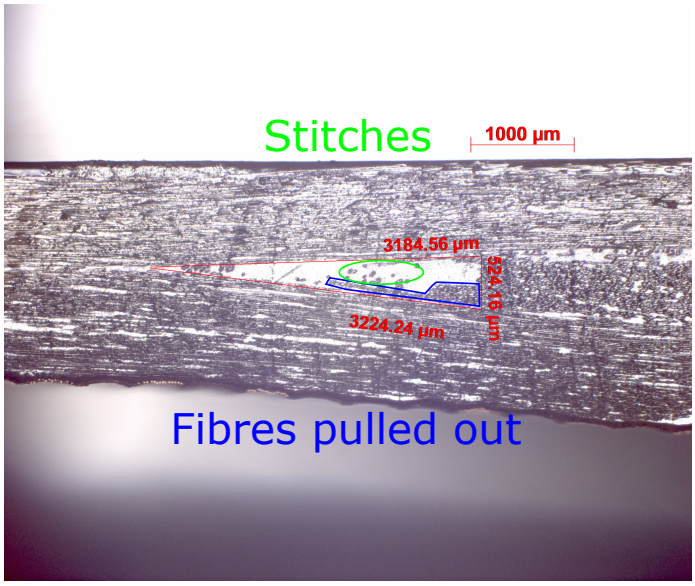

Figure 2.28: Region around the resin pocket with 2.5X magnification.

2.2.1 Geometric Modelling Considerations

As it is seen in the microscope pictures the details of the geometry of the ply-drop specimen is varying and will be different for each specimen. The varying

geometry makes it impossible to model the geometry in a way that will be work for all ply-drops. It is therefore necessary to simplify the geometry into a more general applicable form.

When modelling the geometry it is assumed that all plies are separated by a thin layer of resin. From the microscope images it seems reasonable to set the thickness of a ply to be 0.9 mm and the thickness of the resin layer to be 0.1 mm. This resin layer is used to represent the backing fibres and the pure resin layer in the specimen.

The resin pocket is simplified to a triangle with the height of the dropped ply and a length of 3 mm. This is only applicable for the case where one ply is dropped.

The simplified geometry of a 1-1-1 configuration ply-drop specimen is shown in figure 2.29.

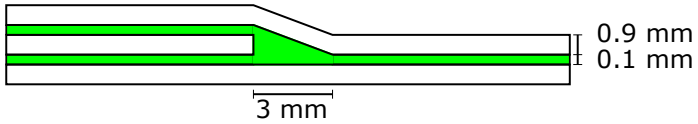

Figure 2.29: The simplified geometry.

2.3 Failure Hypothesis for a Ply-drop Test Specimen in Uniaxial Tension

Experiments are time consuming and it is therefore important to plan experiments such that as much useful data as possible is obtained. Since the topic of this project is predicting failure of composite structures with ply-drops experiments should return information about how, where and when failure occurs.

To assist in planning the experiment and the data acquisition a failure hypothesis is developed. This will help focus attention on areas where failure is likely to occur. The hypothesis is developed based on a thought experiment that illustrates the possibility of ply-drops being cause of delamination. When applying tension loading to the ply-drop the upper ply will have a tendency to straighten out which will induce compressive interface stresses in the thick

end of the ply-drop and induce tension interface stresses in the thin end of the ply-drop. This of course is a simplistic view on the loadings which is only true when no non-linear effects are present. The tension interface stresses will open a crack and potentially cause the crack to grow and thereby cause delamination. In case the ply-drop does not affect the composite, fibre failure is expected, but extensive work has already gone into failure criteria for fibre failure [5].

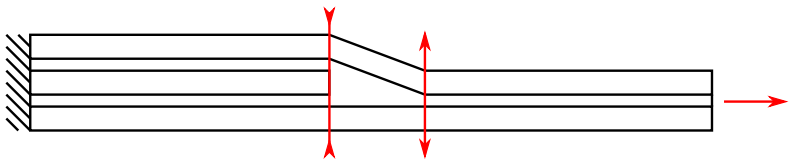

Figure 2.30: Illustration of the tension and compression regions of the ply-drop.

The failure hypothesis is:

1. A crack will initiate in the thin section of the specimen at the ply-drop where opening stresses are present (see figure 2.30).
2. The crack will propagate parallel with the top fibre mat in both directions. The crack will not grow past the dropped ply due to compressive stresses (see figure 2.30).
3. The growing crack will cause a redistribution of stresses and eventually the fibres reach the critical stress limit and the specimen fails.

2.3.1 Obtaining the Necessary Data

The failure hypothesis contains three parts that needs to be checked. Each part is associated with its own set of difficulties and considerations.

Checking Crack Initiation Site

Cracks are usually not visible to the naked eye and magnification is needed. However not knowing the exact location of crack initiation sets a limit on the magnification. Besides being small, cracks can grow in an unstable manner. A literature study on unstable crack growth rates did not reveal information on growth rates in laminated composites.

To capture the crack initiation a USB microscope is used along with manual control of the displacement of the tensile test machine. In case of unstable

crack growth an exact initiation site may not be possible to capture with the above method in which case captured data is interpolated.

Checking Crack Propagation

Crack propagation will occur from crack initiation to final fracture and will involve an area larger than needed for the crack initiation study. As with locating the crack initiation site the microscope is used to attempt capturing the crack propagation.

Checking the Final Failure

The failure hypothesis does not state anything about the location of the final failure. It only states the failure mode. Fibre failure will not create a clean fracture plane as seen in metals. The best option to check the final failure is therefore believed to be by visual inspection.

Specimen Selection

The specimen used for the static tension test is an 1-1-1 specimen. This is considered the simplest specimen since it has two continuous plies and one dropped.

2.3.2 Results of Static Tension Tests

The results of each of the static tension tests can be seen in appendix C.1, C.2, C.8 and C.9. The failure sequence is listed below and illustrated in figure 2.31. Figure 2.33 shows the different failure steps as pictures taken with the microscope.

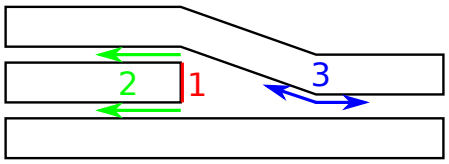

Figure 2.31: Illustration of the failure sequence of the 1-1-1 static tension test specimen.

1. A crack appears in the interface between the dropped ply and the resin pocket. This happens around half the failure load.

2. The crack at the end of the dropped ply extends in both directions causing crack growth into the thick section of the ply-drop both above and below the dropped ply. These cracks grow steadily as the load increases.
3. A new crack appears where the top ply meets the bottom ply. This is not observed on all specimens because it happens quite close to failure sequence four.
4. All cracks grows unstable leading to delamination. The cracks along the dropped ply grows until the clamps of the tensile test machine while the last crack grows approximately half way to the clamps in the thin section of the specimen.
5. Further delamination and fibre failure.

The load displacement curve for the 1-1-1_8 is showed in figure 2.32. There are two drops in the load the first one being delamination of the specimen the next is fibre failure.

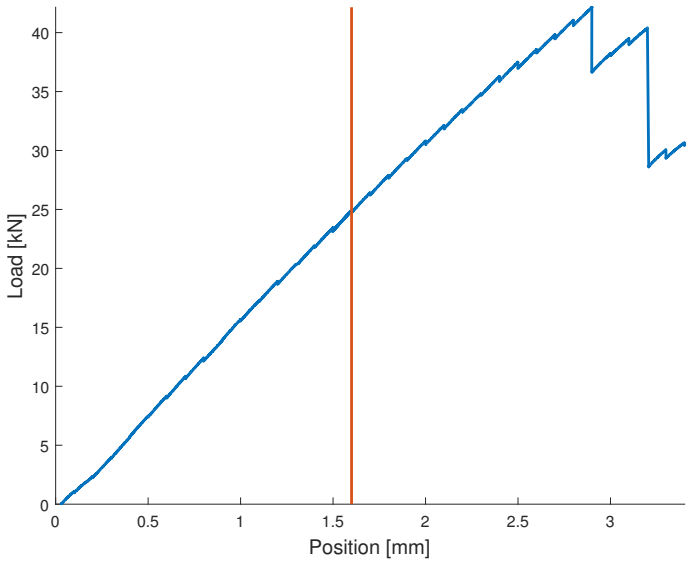

Figure 2.32: Load displacement curve for the test. The vertical red line indicates the first observed crack.

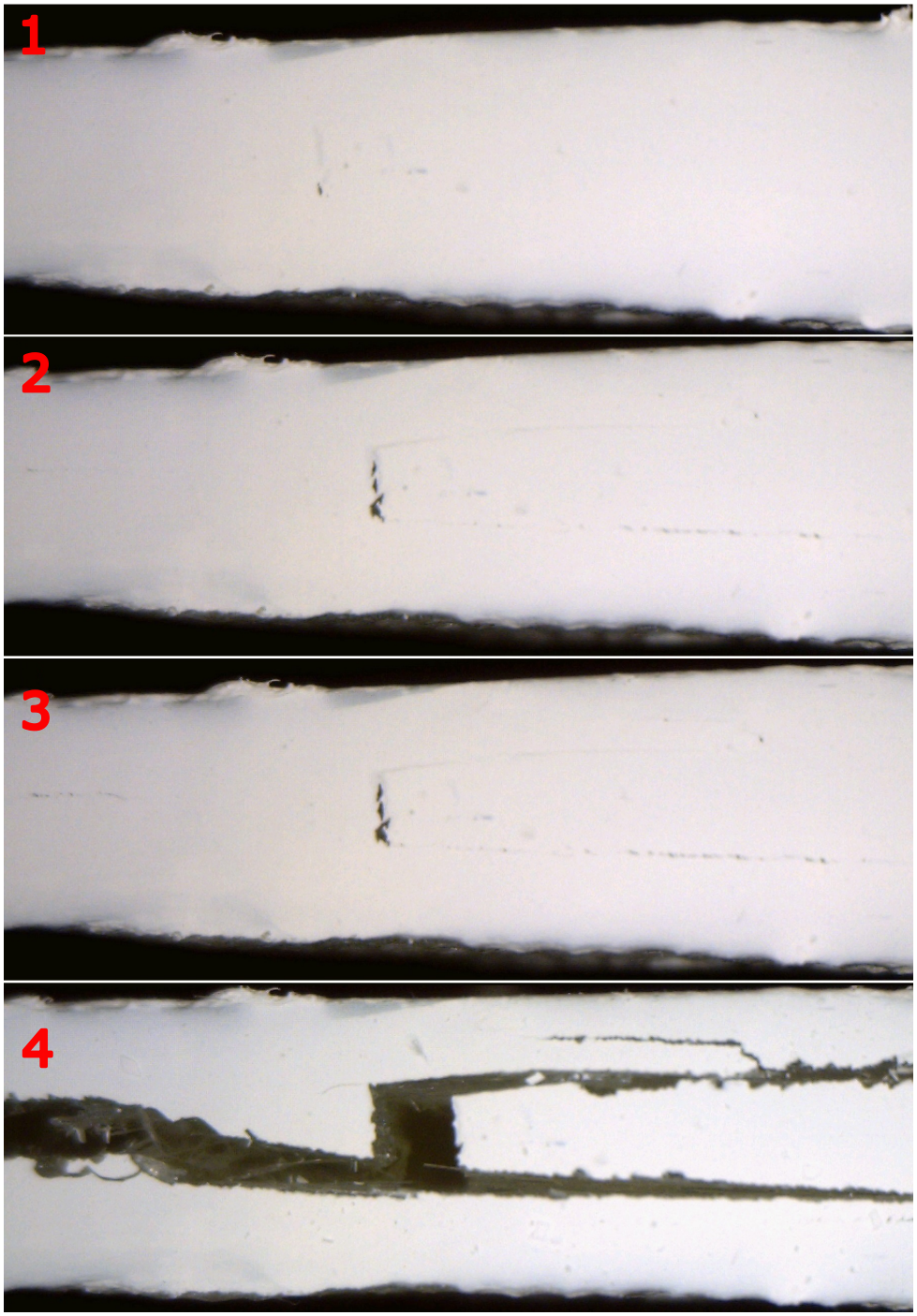

Figure 2.33: Pictures of failure sequence of the 1-1-1_9 static tension test specimen.

The crack lengths are measured by counting the pixels and converting it to mm. This is plotted with respect to the force of each load step as shown in figure 2.34.

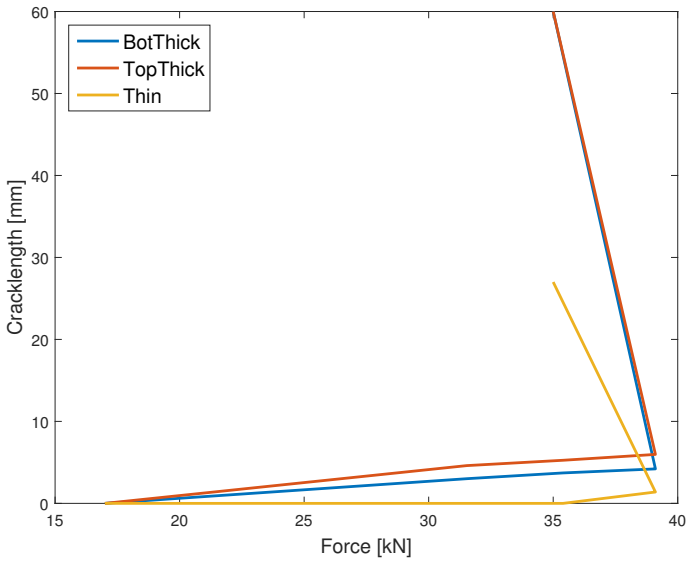

Figure 2.34: Load vs crack length curve for the experiment 1-1-1_9.

From a physical point of view failure in a laminated composite can only exist in three locations, fibres failing, matrix failing or the interface between the matrix and fibres failing. These failures will start at the micro level while the designer typically want to design at macro level. ESA composite handbook [2] has classified 12 possible failure modes for UD composites. Below is explanations of the failure modes observed during the static tension experiment.

Longitudinal tension This is known as fibre failure where the fibres are torn apart, an illustration of fibre failure is shown in figure 2.35. This is often the final failure leading to catastrophic collapse of the structure. This is an intralamiar failure mode where the failure is occurring inside the layer.

Transverse tension This failure mode is in the interface between the fibres and matrix when debonding occurs as illustrated in figure 2.36. This can also happen at the ends of the fibres if a mat is discontinued mid laminate.

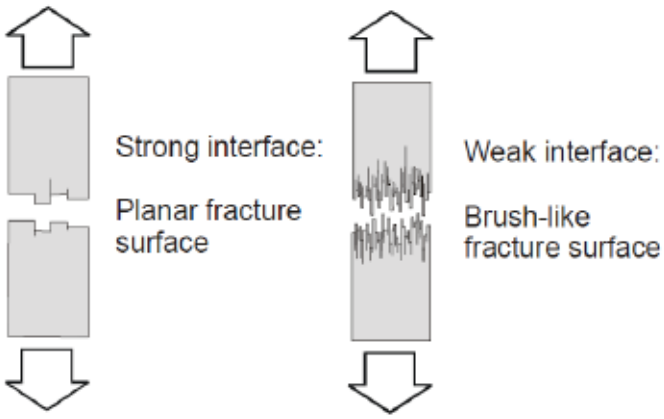

Figure 2.35: Drawing of fibre failure. [3]

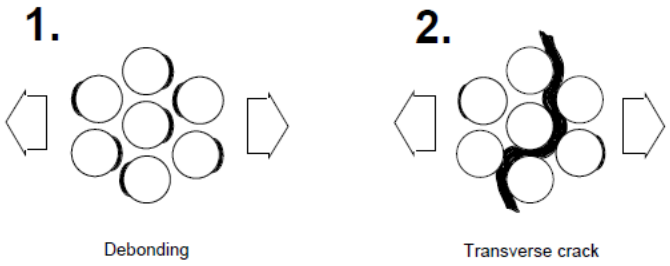

Figure 2.36: Drawings of debond between fibres and matrix. [3]

Short transverse tension This is also know as delamination in mode I where a crack opens in tension. This is an interlaminar failure mode where the crack propagates between layers. Even though the crack grows between layers fibre bridging may occur.

Short transverse shear This is also know as delamination in mode II where a crack opens in shear. This is an interlaminar failure mode where the crack propagates between layers. Even though the crack grows between layers fibre bridging may occur.

2.4 Conclusion on the Static Tension Test

The following parts of the failure hypothesis showed to be incorrect.

1. *A crack will initiate in the thin section of the specimen at the ply-drop where opening stresses are present (see figure 2.30).* This happens but

it is not the first crack that initiates.

2. *The crack will propagate parallel with the top fibre mat in both directions. The crack will not grow past the dropped ply due to compressive stresses (see figure 2.30).* The crack in the thin section does propagate in both directions parallel to the top ply. The hypothesis about it being stopped by the compressive forces is however wrong.
3. *The growing crack will cause a redistribution of stresses and eventually the fibres reach the critical stress limit and the specimen fails.* This happens but as it is seen in test 1-1-1_8 in figure 2.32 the load does not reach above the initial failure load.

The final conclusion of the static tension test is that delamination is the main failure mode in the ply-drop test specimens. Based on the experience obtained during the static tension tests a premise for the finite element modelling is made in regards to crack propagation. When predicting the crack propagation a pre-existing crack is added between the dropped ply and the resin pocket. The crack propagation can be studied with different modelling techniques which is discussed in the next section.

Linear Elastic Fracture Mechanics 3

As stated in chapter 2 delamination is the main failure mode. Delamination is a crack propagating between layers in laminated composite structures. Fracture mechanics is a tool for analysing cracks in solids.

This chapter will present the parts of linear elastic fracture mechanics that is utilized in this project. The presentations will mostly follow the derivations by Andreasen [6] and Zehnder [7] and be for the 2D case since it is being used in the project.

3.1 Energy Release Rate

The concept of energy release rate is presented in this section along with the relation to the total elastic potential. The concept of energy release rate is useful when crack growth needs to be evaluated.

To develop the concept of energy release rate consider figure 3.1. The case of prescribed displacement boundary conditions is considered first. In figure 3.1a the specimen is gradually loaded by a force, P. During loading the force performs work that is stored as strain energy in the material. In the next step (figure 3.1b) the crack grows a small amount, δa, while still complying with the prescribed boundary. In the third step (figure 3.1c) the specimen is unloaded returning the stored strain energy. Under the assumption of elastic materials the strain energy released most be due to the crack growth process. This released energy is $-\delta U$ and marked with red in figure 3.1c. From the definition of the energy release rate the following is derived:

$$G = -\frac{1}{t}\frac{\delta U}{\delta a} \tag{3.1}$$

where G is the energy release rate, t is the width of the specimen. The energy release rate is a measure of the energy released per unit crack growth.

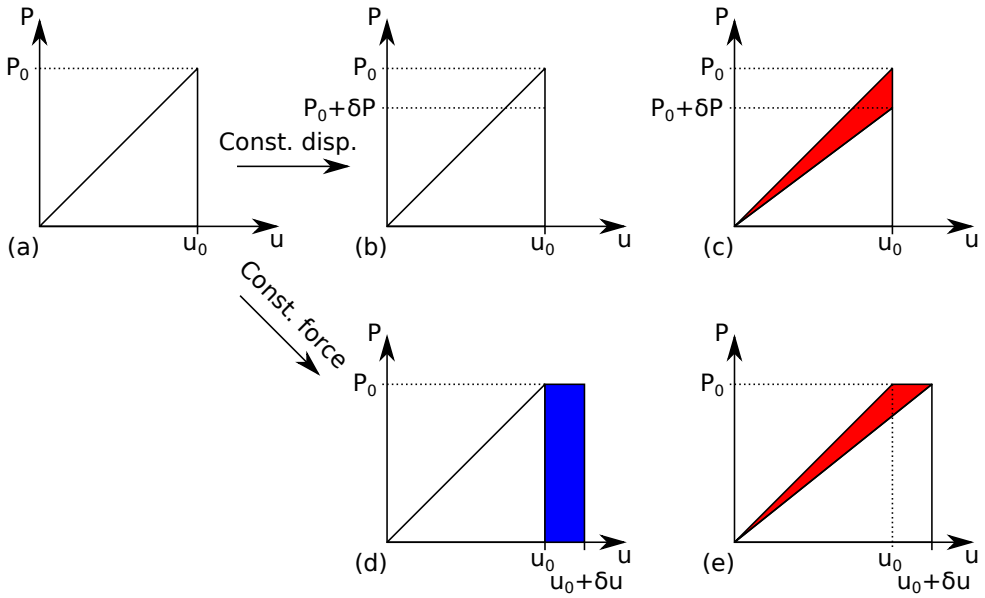

Figure 3.1: Energy released during fracture for the two common boundary conditions, prescribed load and prescribed displacement.

Another common boundary condition is prescribed load. In case of prescribed load the specimen is again gradually loaded storing the work as strain energy. In the next step the crack is grown under constant force as shown in figure 3.1d where it is seen that the force performs additional work, δW. When the specimen is unloaded part of the strain energy is returned. Again an amount of energy, $-(\delta U - \delta W)$, is released during the crack growth process. This leads to the following formula:

$$G = -\frac{1}{t}\frac{\delta U - \delta W}{\delta a} \tag{3.2}$$

Next a more formal development of the energy release rate. The case of prescribed displacement is again treated first followed by prescribed loading.

In case of prescribed displacement the strain energy is written as a function of displacement and crack length as follows:

$$U = U(u, a) \tag{3.3}$$

From a Taylor series considering a small change in crack length the change in

strain energy is written as:

$$\delta U = \frac{\partial U}{\partial a}\delta a \tag{3.4}$$

Equations (3.1) and (3.4) are combined to obtain the following equation for the energy release rate in case of prescribed displacement.

$$G = -\frac{1}{t}\frac{\partial U}{\partial a} \tag{3.5}$$

In case of prescribed load the strain energy is again a function of displacement and crack length. The displacement is however a function of load and crack length. This is written as:

$$U = U(u(P, a), a) \tag{3.6}$$

From a Taylor series considering a small change in crack length the change in strain energy is written as:

$$\delta U = \frac{\partial U}{\partial u}\frac{\partial u}{\partial a}\delta a + \frac{\partial U}{\partial a}\delta a \tag{3.7}$$

where the first term is the additional work performed during crack growth and the second term is the strain energy released during the crack growth process.

By isolating the released strain energy term and replacing it with the result given in equation (3.5) the following can be obtained:

$$\delta U - \frac{\partial U}{\partial u}\frac{\partial u}{\partial a}\delta a = -Gt\delta a \tag{3.8}$$

$$\Updownarrow$$

$$\frac{\delta U}{\delta a} - \frac{\partial U}{\partial u}\frac{\partial u}{\partial a} = -Gt \tag{3.9}$$

and because $\frac{\delta U}{\delta a} = \frac{\partial U}{\partial a}$ when δa approaches zero the equation becomes:

$$G = -\frac{1}{t}\left(\frac{\partial U}{\partial a} - \frac{\partial U}{\partial u}\frac{\partial u}{\partial a}\right) \tag{3.10}$$

and since $\frac{\partial U}{\partial u} = P$:

$$G = -\frac{1}{t}\frac{\partial (U - Pu)}{\partial a} \tag{3.11}$$

and since $(U - Pu) = \Pi$ (Π is the total elastic potential):

$$G = -\frac{1}{t}\frac{\partial \Pi}{\partial a} \tag{3.12}$$

and since the total elastic potential reduces to U in case of prescribed displacement equation (3.12) can handle both prescribed load and displacement.

The Griffith crack growth criterion states:

$$G > G_c \Rightarrow \text{Unstable crack growth} \tag{3.13}$$

$$G = G_c \Rightarrow \text{Stable crack growth} \tag{3.14}$$

$$G < G_c \Rightarrow \text{No crack grwoth} \tag{3.15}$$

The critical energy release rate, G_c, is a material parameter and is a measure of the amount of energy required for extending the crack by a unit area.

3.2 Crack Opening Modes

When a specimen containing a crack is loaded the resulting crack opening can be seen as a combination of the three crack opening modes shown in figure 3.2. The mode mixity is used to describe the combination of crack opening modes. The mode mixity is given as:

$$m_i = \frac{G_i}{G} \tag{3.16}$$

where m is the mode mixity and $i = I, II, III$ indicates the mode mixity of interest. The mode mixity cannot be found from the total elastic potential because the total elastic potential is a global quantity whereas the mode mixity is related to local values. This is not an issue when working with isotropic brittle materials since the crack will grow in the direction of maximum energy release rate. For laminated composites this is not the case since the crack usually is forced to grow between the plies causing delamination in the laminate and the mode mixity becomes of interest.

Multiple models exists to describe how the mode mixity affects the critical energy release rate fx. the power law and the Benzeggagh-Kenane (BK) model [8]. The two models have been fitted to the data provided by Agastra [9] and plotted for the 2D case in figure 3.3. It is seen that the BK model provides

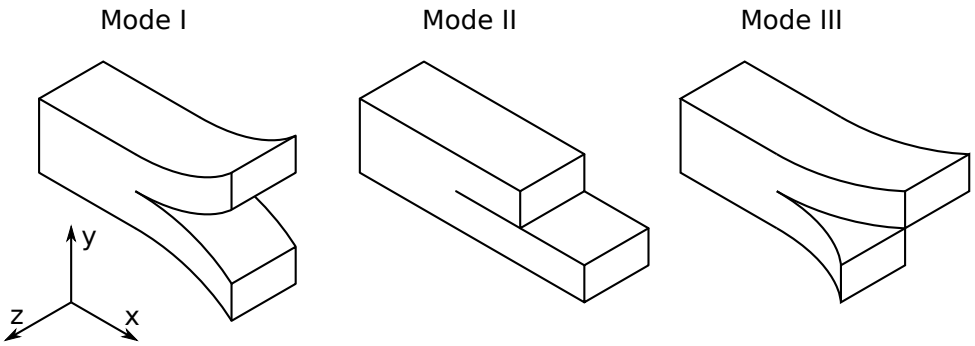

Figure 3.2: Illustrating the three different crack opening modes.

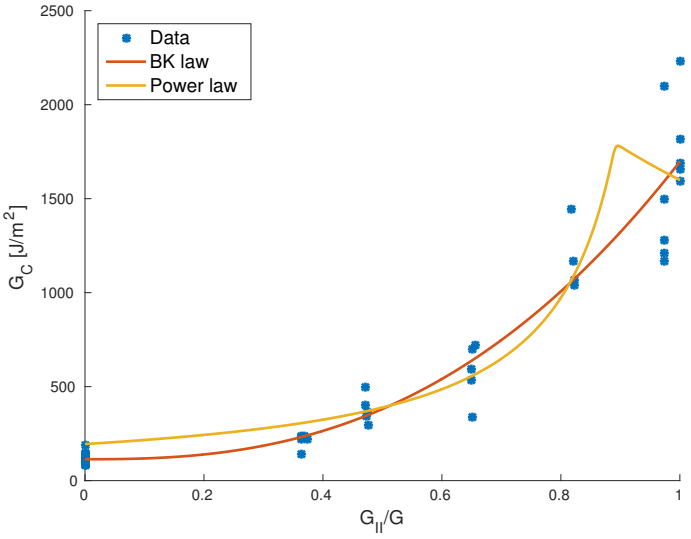

Figure 3.3: Plots of the B-K criterion and power law using different fitting parameters.

the best fit of the two models and is therefore used for determining critical energy release rates.

Next a local approach based on the stresses in the vicinity of the crack front is examined.

3.3 Crack Closure Integral

One of the deficiencies with calculating the energy release rate based on the total elastic potential is that the energy release rate cannot be associated

with an opening mode. Another approach is to study the local effects of crack growth instead of the global effects as with the approach based on the total elastic potential.

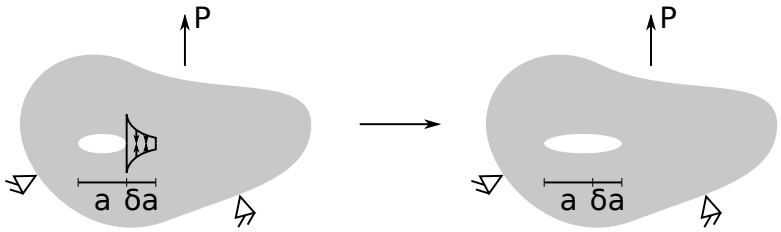

Figure 3.4: Crack growth process illustrating the local effects of crack growth.

The local effects in the crack growth process is illustrated in figure 3.4. Prior to any crack extension the material infront of the crack may be considered to be sustained by tractions, which "breaks" when the crack advances. Under the assumption that the material is elastic the crack growth process can be reversed by applying the interface tractions on the newly created crack surfaces. By this reasoning the energy released during crack growth is equal to the work performed by the interface tractions closing the crack.

The work performed by the interface tractions at the top and bottom fracture surfaces is written as:

$$W = \int_{A^+} dW^+ + \int_{A^-} dW^- \tag{3.17}$$

where the $+, -$ superscripts indicate the top and bottom crack surfaces, and dW is the work increment done by the tractions:

$$dW = \int_{u_i+\Delta u_i}^{u_i} \tau_i \, du_i \, dA \tag{3.18}$$

and under the assumption of linear elastic materials this becomes:

$$dW = -\frac{1}{2}\tau_i \Delta u_i \, dA \tag{3.19}$$

where τ_i is the interface tractions, u_i is the displacement field prior to crack growth, and Δu_i is the increment in displacement due to crack growth.

Equation (3.19) is inserted into equation (3.17):

$$W = -\frac{1}{2}\int_{A^+} \tau_i^+ \Delta u_i^+ \, dA^+ - \frac{1}{2}\int_{A^-} \tau_i^- \Delta u_i^- \, dA^- \tag{3.20}$$

This is simplified by introducing a midplane that is coincident with both crack surfaces before deformation. From Newtons third law it is seen that, $-\tau_i^- dA^- = \tau_i^+ dA^+ = \tau_i dA$:

$$W = -\frac{1}{2}\int_A \tau_i \Delta u_i^+ \, dA + \frac{1}{2}\int_A \tau_i \Delta u_i^- \, dA \tag{3.21}$$

$$= -\frac{1}{2}\int_A \tau_i (\Delta u_i^+ - \Delta u_i^-) \, dA \tag{3.22}$$

$$= -\frac{1}{2}\int_a^{a+\delta a} \tau_i (\Delta u_i^+ - \Delta u_i^-) t \, da \tag{3.23}$$

The work performed by the tractions when the crack grows a distance δa is associated with an average energy release rate. To obtain an instantanious value the energy release rate is evaluated in the limit as δa goes to zero:

$$G = \lim_{\delta a \to 0} -\frac{1}{2t\delta a}\int_a^{a+\delta a} \tau_i (\Delta u_i^+ - \Delta u_i^-) t \, da \tag{3.24}$$

The above equation is known as the crack closure integral. If the crack openings and tractions are evaluated in the coordinate system shown in figure 3.2 the above equation is expanded to:

$$\begin{aligned} G =& G_{II} + G_I \\ =& \lim_{\delta a \to 0} -\frac{1}{2t\delta a}\int_a^{a+\delta a} \tau_x (\Delta u_x^+ - \Delta u_x^-) t \, da + \\ & \lim_{\delta a \to 0} -\frac{1}{2t\delta a}\int_a^{a+\delta a} \tau_y (\Delta u_y^+ - \Delta u_y^-) t \, da \end{aligned} \tag{3.25}$$

This is an advantage over the global approach since the critical energy release rate is dependent on the mode mixity.

An assumption for the derivation is that the interface tractions only are present where the interface is intact. This is however not always the case in laminated composites where fibre bridging may occur (figure 3.5). Fibre bridging increases the strength of the interface since the fibers are stronger than the resin.

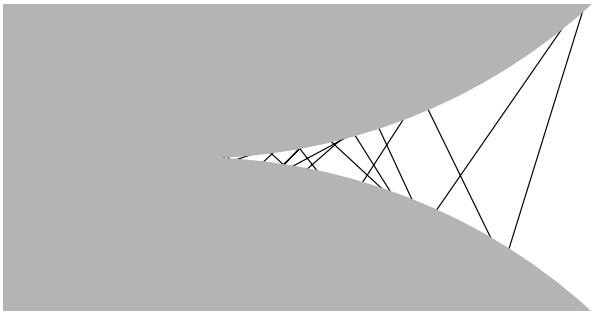

Figure 3.5: Fibre bridging is fibres crossing the interface where the crack grows.

3.4 Implementation in the Finite Element Method

To evaluate the energy release rate knowledge of the displacement field and the stress state of the continuum is needed. Analytical solutions are however rarely available. In these cases the finite element method is a valuable tool and some of the implemented techniques is explained in the following.

3.4.1 The Finite Crack Extension Method

The gradients of the total elastic potential in equation 3.12 may be determined using a finite difference scheme.

$$\Pi(a+\delta a) = \Pi(a) + \frac{\partial \Pi}{\partial a}\delta a \tag{3.26}$$

$$\Updownarrow$$

$$\frac{\partial \Pi}{\partial a} = \frac{\Pi(a+\delta a) - \Pi(a)}{\delta a} \tag{3.27}$$

Inserting equation 3.27 into equation 3.12 yields:

$$G = -\frac{1}{t}\frac{\Pi(a+\delta a) - \Pi(a)}{\delta a} \tag{3.28}$$

To evaluate the energy release rate two simulations are needed. One with crack length a and one with crack length $(a+\delta a)$.

3.4.2 The Crack Closure Method

This method is a finite element implementation of the crack closure integral, eq. (3.24). Due to the discrete nature of the finite element method the evaluation of the crack closure integral reduces to a point force. In the crack

closure method the limit is handled by using an element size small enough to keep the error within acceptable limits. This reduces the crack closure integral to:

$$G = G_{II} + G_I = -\frac{1}{2t\delta a}(P_x \Delta u_x + P_y \Delta u_y) \tag{3.29}$$

where $\Delta u_i = \Delta u_i^+ - \Delta u_i^-$, P_i is the constraint force. It is important to notice that the constraint force and nodal displacement is for the same node, as illustated in figure 3.6, meaning that two different models are needed to calculate G using the crack closure method.

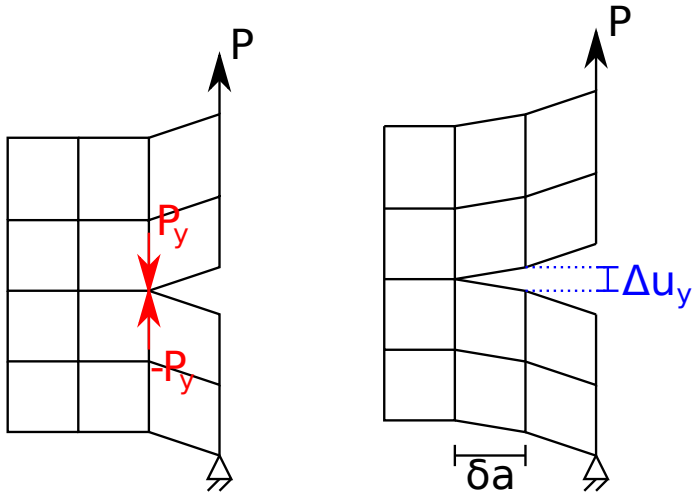

Figure 3.6: On the left is an initial analysis to get the constraint forces and on the right the crack has been increased by δa to get the nodal displacement.

3.4.3 The Virtual Crack Closure Technique

The crack closure method can be simlified by assuming self-similiar interface tractions as the crack grows. This assumption means that the constraint forces and nodal displacements can be taken from different nodes and thereby can G be calculated from one single analysis instead of two as required by the crack closure method.

$$G = G_{II} + G_I = -\frac{1}{2t\delta a}(P_x \Delta u_x + P_y \Delta u_y) \tag{3.30}$$

This method is more effecient than the crack closure method however there is no such thing as a free dinner. For the virtual crack closure technique the cost

is accuracy since the assumption of self-simliiar interface tractions is only valid when δa is small and the virtual crack closure technique is therefore highly mesh dependent.

Finite Element Modelling of Ply-drop Specimen 4

Modelling of the ply-drop specimen consists of two components. A model for the elastic response and an fracture mechanics extension of that model. Having two models provides the possibility of validating the model in steps.

4.1 Material Parameters

Table 4.1 contains the elastic material parameters for the test specimens. Each parameter is listed along with its value and origin. In the 2D FE-simulation only the material parameters marked with x are necessary. The values by

Constant	Value	Unit	2D FEM	Origin
$E11_{ply}$	40.2	[GPa]	x	Experimental
$E22_{ply}$	13.3	[GPa]		Experimental
$E33_{ply}$	8.5	[GPa]	x	ESAComp
$G12_{ply}$	3.5	[GPa]	x	ESAComp
$G13_{ply}$	3.5	[GPa]		ESAComp
$G23_{ply}$	3.27	[GPa]		ESAComp
$\nu 12_{ply}$	0.3		x	ESAComp
$\nu 13_{ply}$	0.3			ESAComp
$\nu 23_{ply}$	0.3			ESAComp
E_{resin}	3	[GPa]	x	ESAComp
ν_{resin}	0.316		x	ESAComp

Table 4.1: Elastic material parameters.

ESAComp [4] are for an isophathalic UD with a fibre volume fraction of 50 %. The values determined experimentally are determined using an extensometer and a tensile test machine. The elasticity modulus for each data point in the test is plotted in figure 4.1 for $E11_{ply}$ and figure 4.2 for $E22_{ply}$. The red line indicates the optimised modulus. The optimisation is based on a least square formulation.

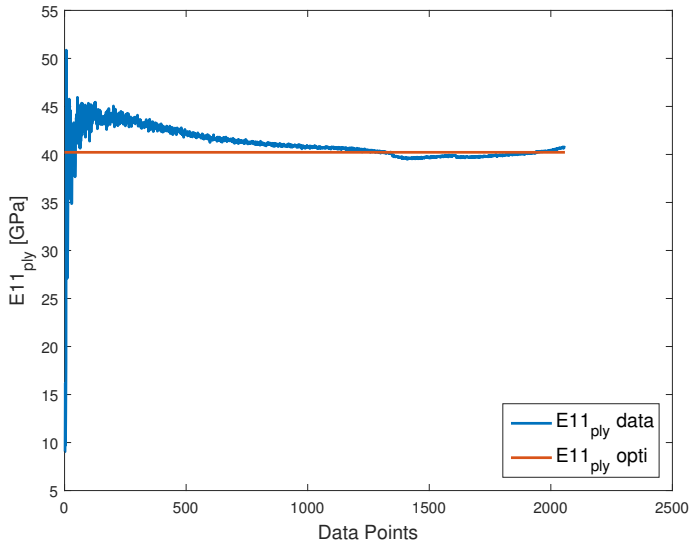

Figure 4.1: Plot of $E11_{ply}$.

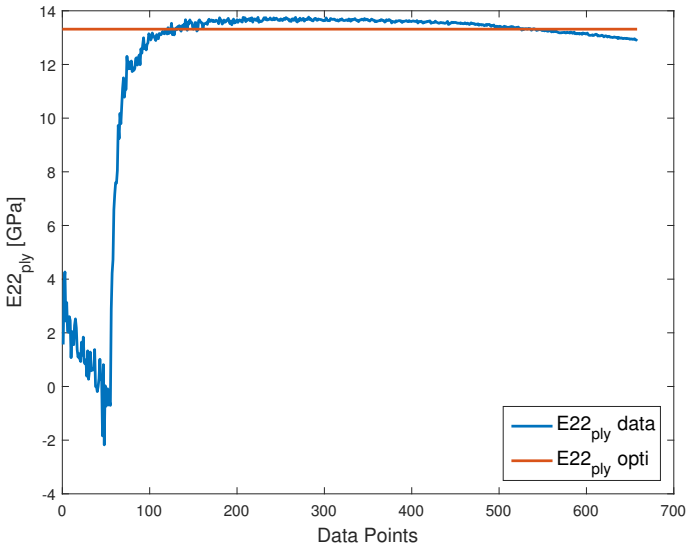

Figure 4.2: Plot of $E22_{ply}$.

As stated in section 3.2 a crack opening can be seen as a combination of three different modes. Thereby material data has to be obtained for different mode mixities. This is a comprehensive task and will not be conducted due to time restraints. Agastra [9] has already performed similar experiments and this project will rely on that data.

The critical energy release rates and standard derivation for each mode mixity is listed in table 4.2. The material parameters for pure mode I is obtained using the double cantilever beam specimen, the pure mode II using the end-notched flexure specimen and the rest using the mixed mode bending test. The specimens was produced with resin transfer moulding cured at 20°C for 24 hours, post cured for 6 hours at 65°C and had a fibre volume fraction of 36.7%.

4.2 Elastic Response

The elastic response of the FE-model is compared with digital image correlation (DIC) measurements. The geometry and boundary conditions are presented in figure 4.3. The length of the FE-model is found by inspecting the specimens for clamping marks and measuring the distance between them. The FE-model is a 2D-model in plane stress because the results will be compared

	G_{Ic} $[\mathrm{J/m^2}]$		G_{IIc} $[\mathrm{J/m^2}]$	
m_I	avg	std	avg	std
1	116	27	0	0
0.63	136	23	79	13
0.53	201	41	180	36
0.35	201	53	376	101
0.18	212	35	968	149
0.03	37	10	1412	374
0	0	0	1797	256

Table 4.2: Critical energy release rates Agastra [9].

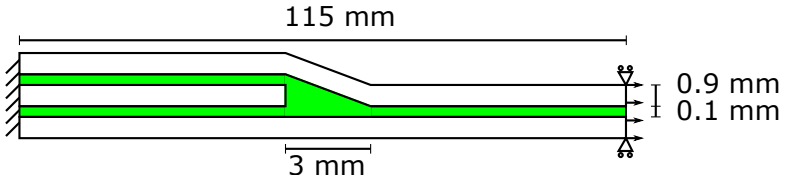

Figure 4.3: Geometry of the FE-model.

with DIC measuarements which are based on a surface which can have no out-of-plane stress component. The analysis is a non-linear geometric analysis with automatic time stepping. The model has the initial crack at the end of the dropped ply, because the crack in the majority of the tests have been visible around half the total failure load and Carrella-Payan et al. [10] have observed that the crack has emerged from the curing due to differences in thermal expansion.

To compare the elastic response with the DIC measurements the longitudinal displacement along three paths are compared. The three paths and their relative coordinates to the middle of the end of the dropped ply are shown in figure 4.4. The comparison is made on the displacement because there is less noise on the displacement compared to the strain from DIC.

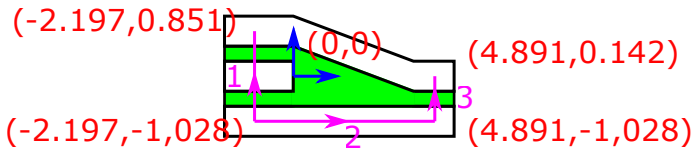

Figure 4.4: Paths in DIC compared with FE-model (Distances in mm).

4.2.1 Mesh Sensitivity Study

The mesh sensitivity study is based around the path plot along path 1 of the longitudinal displacement field. The study uses two kinds of elements: a Q4-element with reduced integration and a Q4-element with incompatible modes. The result from the study is seen in figure 4.5. The legend denotes the element and the first number is the number of elements in the thickness of the ply while the second number is the number of elements in the thickness of the resin. As it is seen from figure 4.5 the model is converged with regards to

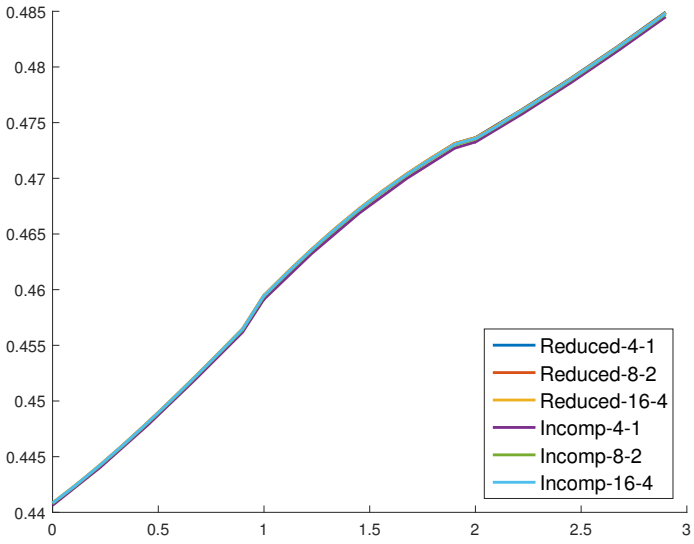

Figure 4.5: Mesh sensitivity.

the displacements along path 1. The worst performing mesh is the Incomp-4-1 mesh but it is still converged. Thereby all of these meshes can be used further.

4.2.2 Digital Image Correlation

The DIC measurements are performed using the DIC equipment available at the Department of Mechanical and Manufacturing Engineering at Aalborg

University. The DIC equipment is used along with NCORR an open-source software for MATLAB used to process the images. The result of the longitudinal displacements is shown in figure 4.6 while the transverse displacement and the strains are shown in appendix D.1 along with the image processing settings. Figure 4.6 shows the three paths from where data is compared with the FE-model.

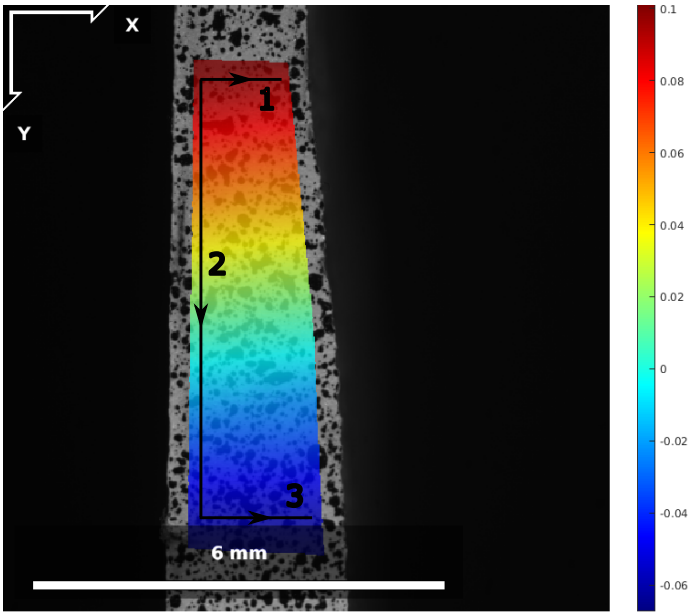

Figure 4.6: Contour plot of the longitudinal displacements.

The longitudinal displacement for each path is plotted in figure 4.7 to 4.9. Each plot contains a curve from the DIC measurements, a FE-model with a crack at the end of the dropped ply and a curve from the FE-model with no crack.

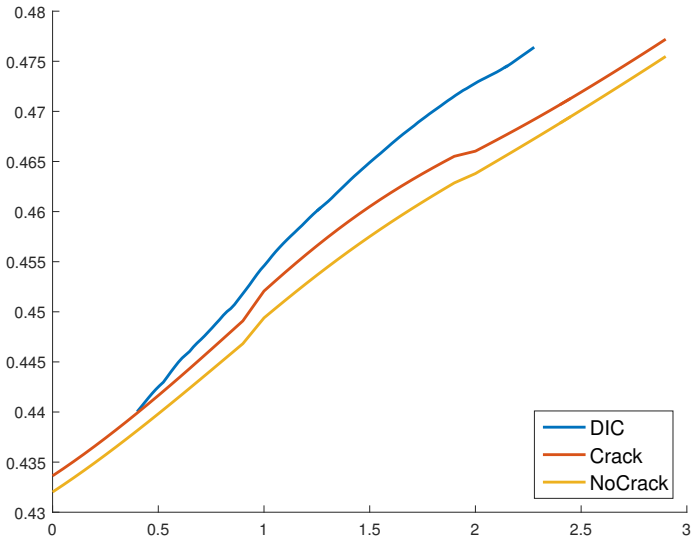

Figure 4.7: Path 1.

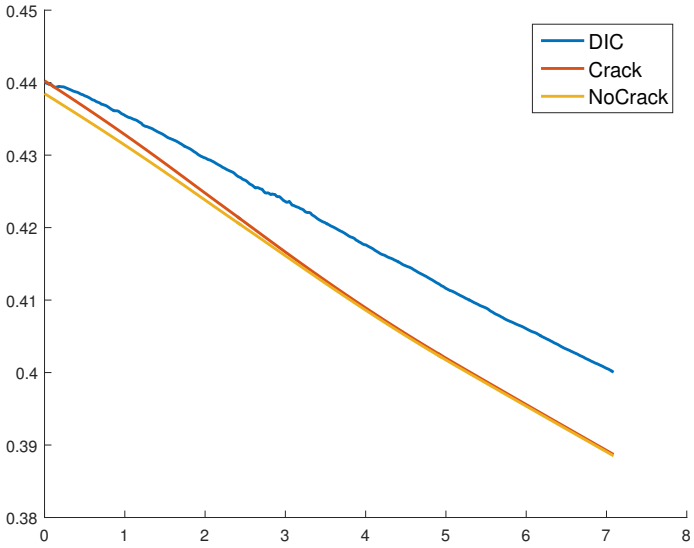

Figure 4.8: Path 2.

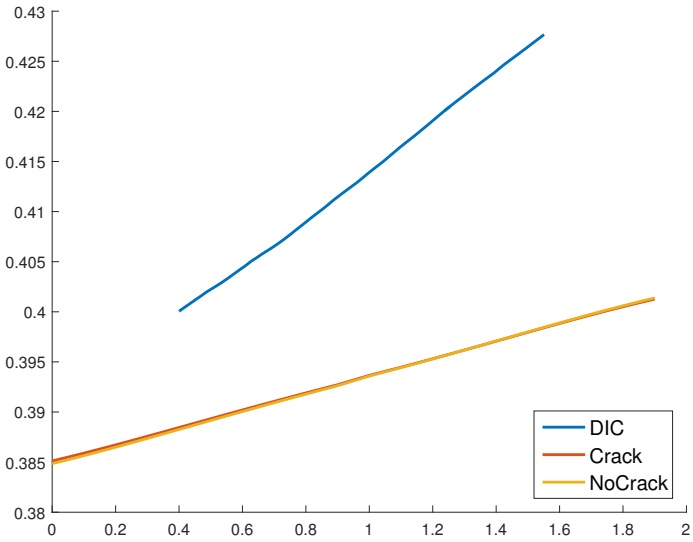

Figure 4.9: Path 3.

There is an error in both the size and slope in path 1 and 2. The error in path 3 is larger than the two others but this could be because the simplified geometry is too crude to represent the displacement around path 3 correctly. It is seen from the microscope pictures in section 2.2 that the length of the resin pocket extends further than the 3 mm modelled in the FE-model. It is an advantage if the simple geometry can be applied to every ply-drop configuration because the model will be more general. It is therefore beneficial to perform inverse modelling to see if the simple geometry can be used to model the ply-drop.

4.2.3 Inverse Modelling

The inverse modelling is done by formulating an optimisation problem and using MATLABs genetic algorithm to solve it. The object of the optimisation is to minimize the error between the DIC and the FE-model at the paths. This is done by using a least square formulation where each data point in the DIC measurements is compared with the equivalent in the FE-model. The objective function then becomes:

$$\begin{aligned} Error = &(\vec{P}1_{DIC} - \vec{P}1_{FEM}) \bullet (\vec{P}1_{DIC} - \vec{P}1_{FEM}) \\ &+ (\vec{P}2_{DIC} - \vec{P}2_{FEM}) \bullet (\vec{P}2_{DIC} - \vec{P}2_{FEM}) \\ &+ 0.1 \cdot (\vec{P}3_{DIC} - \vec{P}3_{FEM}) \bullet (\vec{P}3_{DIC} - \vec{P}3_{FEM}) \end{aligned} \tag{4.1}$$

Where P is vectors containing the data for the path. The path have different length leading to a natural weighting. Path 1 has 107 data points, path 2 401 and path 3 67. Thereby path 2 has approximately 4 times the weighting of path 1. Furthermore because of the geometry of path 3 the weight is reduced to 10%.

The optimisation input variables is listed in table 4.3 with their upper and lower bounds. The bounds of the geometry has been decided based on inspection of the specimen taking the worst case scenarios. The bounds of the material parameters are chosen to be ±20% of the original from ESAComp. The bounds of the experimentally determined material parameters are ±5%. The bounds of the materials parameters is implemented in the optimisation using factors between 0.8 and 1.2 instead of their real values listed in table 4.1. The reason for this is to lower the distance from the highest to the lowest number. The distance is reduced by approximately 10^{10}. The optimisation

Parameter name	Lower bound	Upper bound	Unit
$l_{specimen}$	110	120	[mm]
l_{drop}	2	7	[mm]
t_{ply}	0.85	0.95	[mm]
t_{resin}	0.05	0.1	[mm]
E_{resin}	2.4	3.6	[GPa]
ν_{resin}	0.2528	0.3792	
$E11_{ply}$	38.19	42.21	[GPa]
$E22_{ply}$	6.8	10.2	[GPa]
$G12_{ply}$	2.8	4.2	[GPa]
$\nu 12_{ply}$	0.24	0.36	

Table 4.3: Optimisation input variables with upper and lower bound.

is carried out using MATLAB's built in genetic algorithm with default solver parameters. The search based $fmincon$ optimisation algorithm in MATLAB is tried but yielded different results for different starting guesses.

4.2.4 Results of the optimisation

After 69 generations and 14000 function evaluations the results are obtained. The results are presented in figure 4.10 to 4.12 and the optimised input variables are listed in 4.4.

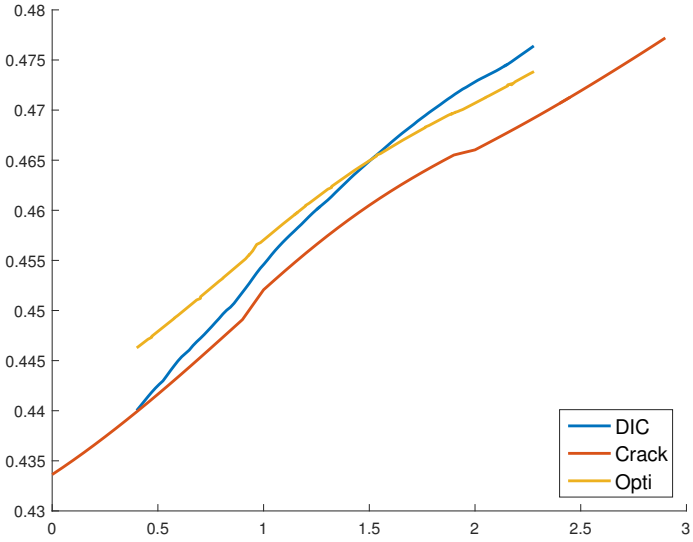

Figure 4.10: Path 1

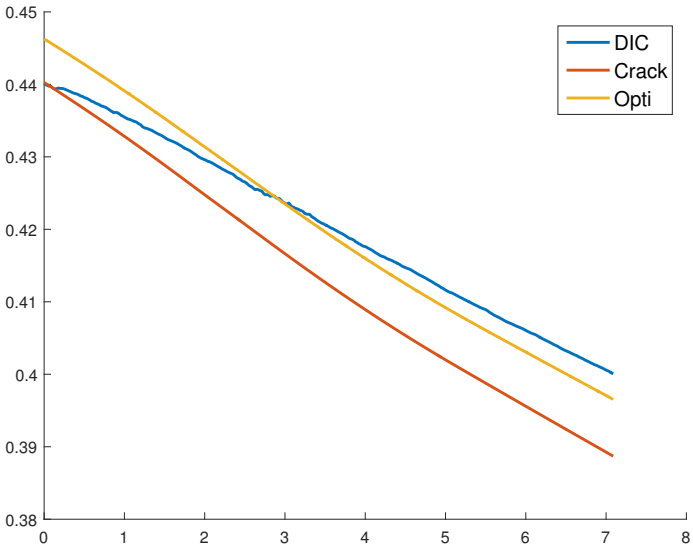

Figure 4.11: Path 2

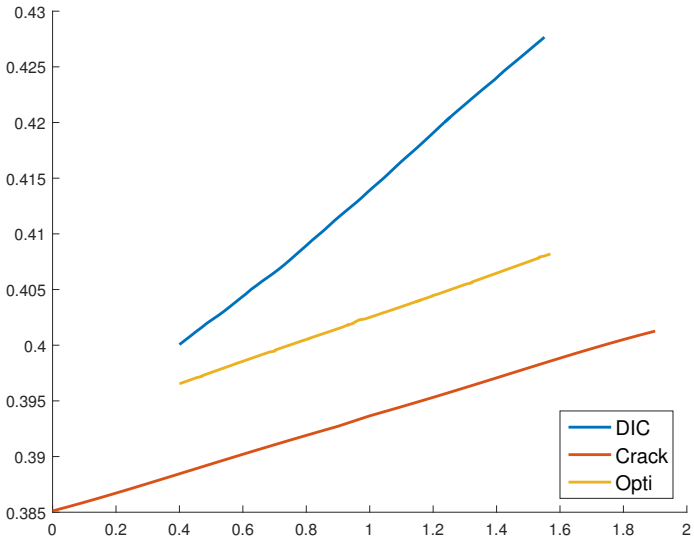

Figure 4.12: Path 3

Parameter name	Value	Unit
$l_{specimen}$	119.6	[mm]
l_{drop}	3.3	[mm]
t_{ply}	0.91	[mm]
t_{resin}	0.054	[mm]
E_{resin}	3.6	[GPa]
ν_{resin}	0.253	
$E11_{ply}$	41.5	[GPa]
$E22_{ply}$	10.2	[GPa]
$G12_{ply}$	3.6	[GPa]
$\nu12_{ply}$	0.24	

Table 4.4: Input variables after optimisation.

It is seen that the results have improved along all three paths. The results of the FE-model is still not on top of the DIC but that cannot be expected as the FE-model has a simplified geometry. These results are considered good enough to continue with the FE-modelling of the crack growth.

Following parameters is close to the boundary: $l_{specimen}$, t_{resin}, E_{resin}, ν_{resin}, $E22_{ply}$,. All of them expect $l_{specimen}$ and t_{resin} is directly related to the material parameters of the resin. This could be an indication of that the material parameters for the resin found in ESAComp does not correspond to the resin provided by LM Wind Power. Thereby the two largest contributors to the error in the elastic response according to the optimisation process are the simplified geometry and the material parameters of the resin.

4.3 Application of Fracture Mechanics

From the experiments it is known that the test specimen fails due to delamination. This section will therefore extend the FE-model developed in the previous section to also include fracture properties. Different approaches to fracture modelling using the finite element method has been presented in section 3.4. Besides the methods from section 3.4 the fracture properties can also be evaluated using either the J-integral or using cohesive elements.

Neither of the fracture mechanic implementations from section 3.4 will tell anything about the initiation phase of the failure. However cohesive zone elements can be used to simulate both crack initiation and growth. A drawback with cohesive zone elements is that they introduce discontinuities into the equilibrium curve and can therefore cause convergence issues. The ability to predict crack initiation gives the cohesive elements a clear advantage over the methods listed in section 3.4. It is for this reason that some effort is put into a model using cohesive elements.

4.3.1 Model Using Cohesive Zone Modelling

Knowledge of the crack path is needed prior to modelling because the cohesive elements forms the interface in which cracks can grow. Figure 4.13 shows how the cohesive elements have been implemented in the finite element model. Note that Abaqus does not seem to support zero thickness cohesive elements [8] and the resin layers are therefore replaced with cohesive elements.

To deal with the convergence issues the following solvers and solver options has been tested:

- Static model
- Transient model using mass scaling (Explicit solver)

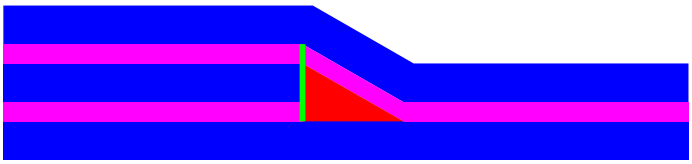

Figure 4.13: Overview of CZM based FE-model (not to scale). The blue area is the plies, the red area is the resin, the purple area is cohesive elements and the green line indicates the preexisting crack.

- Transient model using mass scaling until a point before the solution explodes after which mass scaling is disabled (Explicit solver)

In Abaqus not all elements are available when using the explicit solver this means that the continuum elements used for static simulation is a 4 node element with incompatible modes whereas when using the explicit solver a 4 node element with reduced integration is used.

Implicit solvers are usually gradient based and therefore has difficulties handeling discontinuous equilibrium curves. Explicit solvers are only conditional stable. For numerical stability it is required that the time step is so small that the stress wave cannot pass an element in one time step [11]. This condition means that the time step for the model becomes infeasible small. However for quasi static models mass scaling can be applied. Mass scaling works by scaling the material densities thereby lowering the speed of the stress wave resulting in an increase in the critical time step. Increasing the mass of the model increases inertial forces hence it should only be used when the simulation can be considered quasi static.

It was however not possible to obtain a solution using cohesive elements.

4.3.2 Model Using the Virtual Crack Closure Technique

When employing the Virtual Crack Closure Technique (VCCT) knowledge of the crack path is needed as with the cohesive elements. Furthermore is knowledge about where the crack starts and in which direction it grows needed. This information has been found from experiments in section 2.3.2. Utilizing the experimental data the cracks and initiation sites has been inputted into the model as shown in figure 4.14. The cracks are named as 1: BotThick, 2: TopThick, 3: ThinRight and 4: ThinLeft where the numbers are references

to the figure. The energy release rates are evaluated using the VCCT method

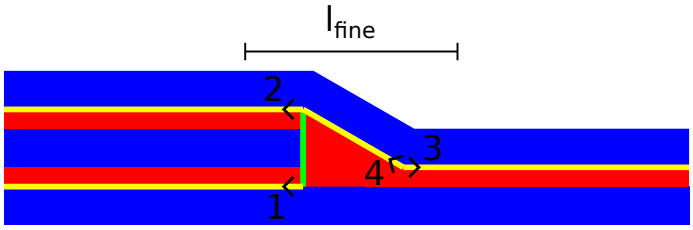

Figure 4.14: Overview of VCCT based FE-model (not to scale). The blue area is the ply, the red area is the resin, the yellow lines indicate crack paths with the arrows indicating the direction of crack growth and the green line indicates the preexisting crack. The black numbers indicate the naming of the cracks.

built into Abaqus. VCCT is, as stated in section 3.4.3, mesh sensitive why a study on mesh convergence is conducted. The mesh convergence study is performed using fractions of the experimentally obtained critically crack lengths with increasingly smaller elements. The Abaqus teaching licens is restricted to 250,000 nodes why the mesh is divided into a coarse and fine mesh as indicated in figure 4.14 such that smaller elements can be achieved in the region close to the ply-drop. For the mesh convergence study l_{fine} is 20 mm. Figures 4.16 and 4.15 is representive for the mode I and II energy release rates for the four cracks.

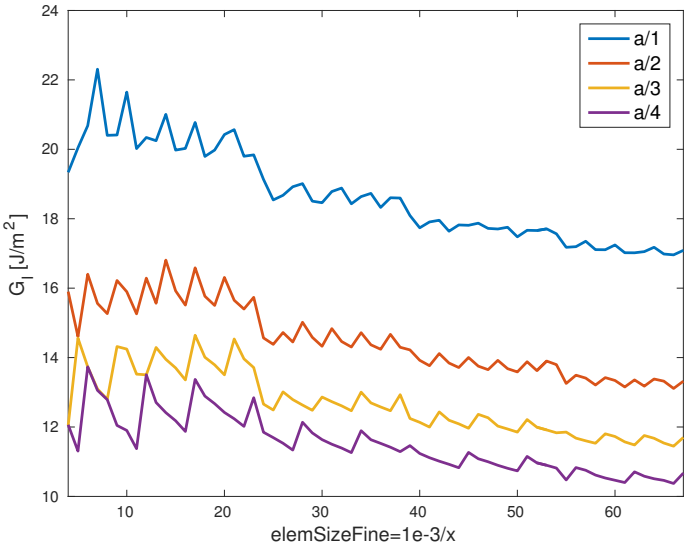

Figure 4.15: G_I from the crack growing in the thin section away from the ply-drop

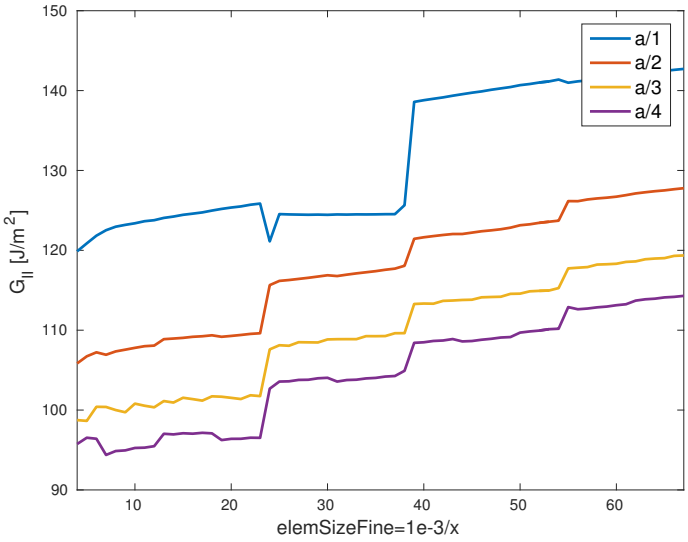

Figure 4.16: G_{II} from the bottom crack in the thick section

From figures 4.15 and 4.16 it is seen that mesh convergence has not been achieved. It is not possible to add more elements due to the 250,000 node restriction on the Abaqus teaching license. A follow up litterature study reveals that VCCT will not convergence on bi-material interfaces [12] due to oscillating stresses in the vicinity of the crack [13].

To determine the mode mixity a local approach is needed why it needs to be examined if VCCT can be used to approximate the mode mixity. A convergence study is conducted and the results is shown in figures 4.17 and 4.18.

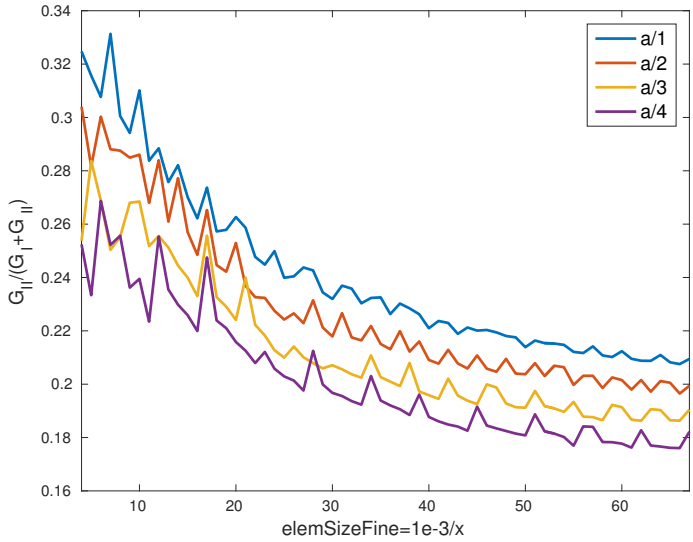

Figure 4.17: Mode mixity for the bottom crack in the thick section

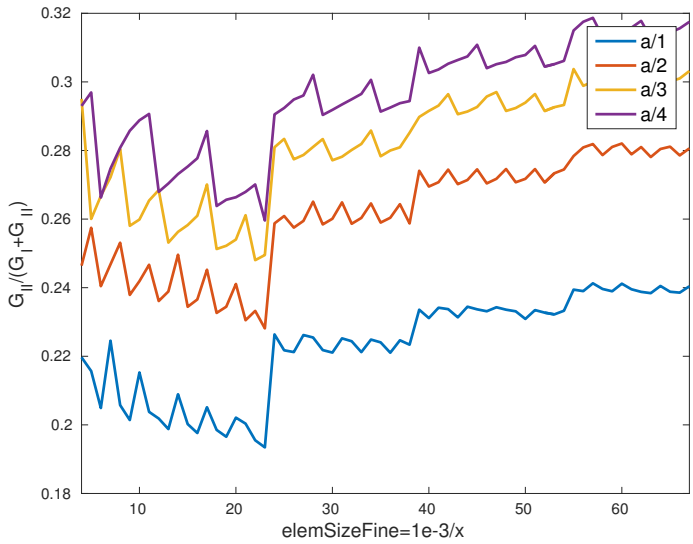

Figure 4.18: Mode mixity for the crack growing in the thin section away from the ply-drop

As with the energy release rates the mode mixities does not converge. Figure 4.17 shows a maximum difference in mode mixity between the coarsest and the finest mesh around 12%. The mode mixities is however still calculated using VCCT in lack of better options.

4.3.3 Model Using the Finite Crack Extension Method

Due to the problems with VCCT caused by the bi-material interface another method is needed for evaluating the energy release rates. Two methods are available for evaluating the energy release rates, the Finite Crack Extension Method (FCEM) or the J-integral however none of these methods provides any insight into the mode mixity. The J-integral is more efficient since it only requires one model however the J-integral requires a new model whereas the finite crack extension method only requires an addition to the VCCT model. By using the VCCT model as a base for the FCEM model VCCT can be used to approximate the mode mixity.

The mesh using FCEM is identical to the mesh using VCCT because FCEM is an addition to the VCCT model.

As with the VCCT model a study on convergence is conducted for the FCEM model. Representative convergence plots is shown in figures 4.19 and 4.20.

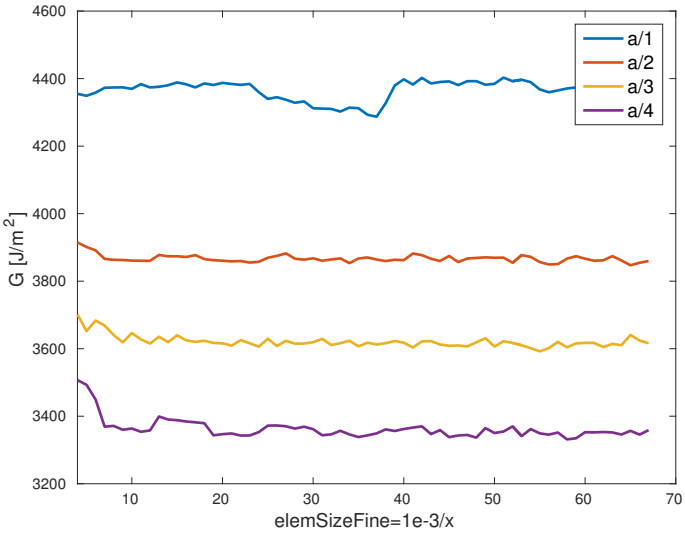

Figure 4.19: *G* from the bottom crack in the thick section

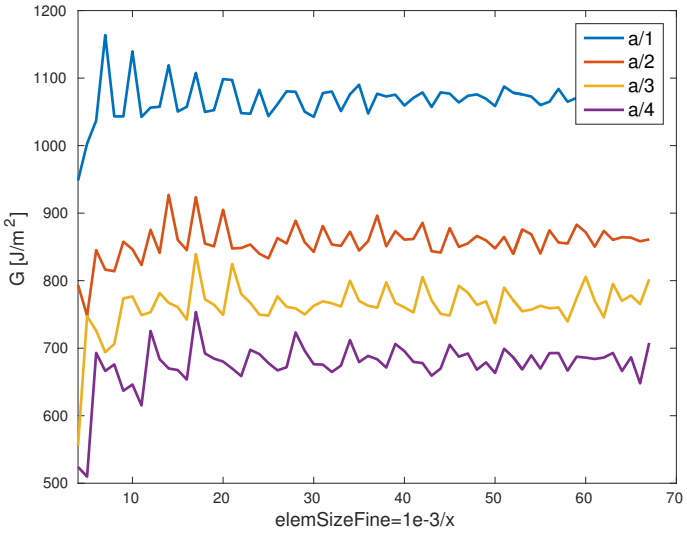

Figure 4.20: *G* from the crack growing in the thin section away from the ply-drop

From the convergence plots it is seen that FCEM convergence however with some spikes due to small variations in crack length because the crack length depends on the element size. Further it is seen that the energy release rates for FCEM is generally higher and closer to the critical energy release rates provided by Agastra [9].

Changes in Energy Release Rates Caused by Growing Cracks

The energy release rate vs crack length curves can be used to study the energy release rate at different crack lengths. In this FE-simulation there are four different cracks and it is therefore impossible to plot them all in one curve since it will require a plot with more than three dimensions. It is therefore chosen to divide the study into two parts, one where the crack development in the thin section is examined and one where the crack development in the thick section is examined.

Crack growth in the thick section is studied under two circumstances, one where the cracks in the thin section are closed and one where they are grown. In the case where the cracks in the thin section are grown the ThinRight crack is 15 mm and the ThinLeft crack is deactivated/fully grown. During the crack growth study in the thick section both cracks in the thick section are grown equally which corresponds to the experimental data that showed both cracks

were similiar in sizes. The results of the simulations are shown in figure 4.21.

The study of the two cracks in the thin section consists of simulations where the cracks in the thick section is closed and one where the cracks are grown 20 mm. The crack lengths of ThinLeft and ThinRight are varied equally until 3.3 mm where ThinLeft is fully grown and therefore excluded from the remaining simulations. The results of the simulations are shown in figure 4.22.

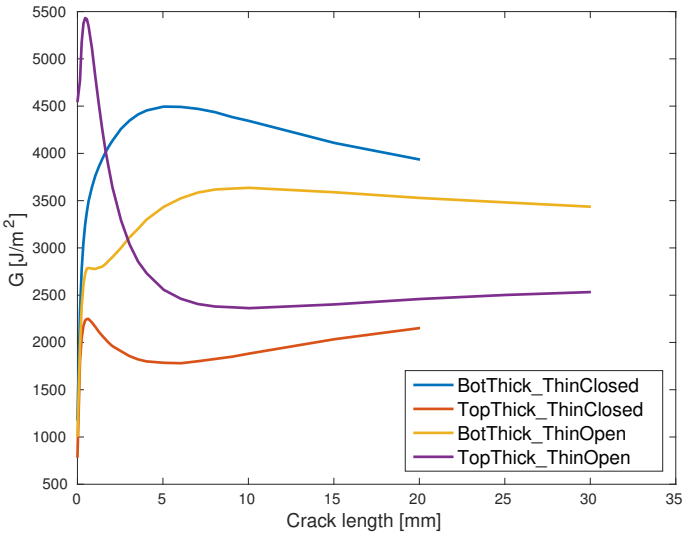

Figure 4.21: G-crack length curves for the thick section.

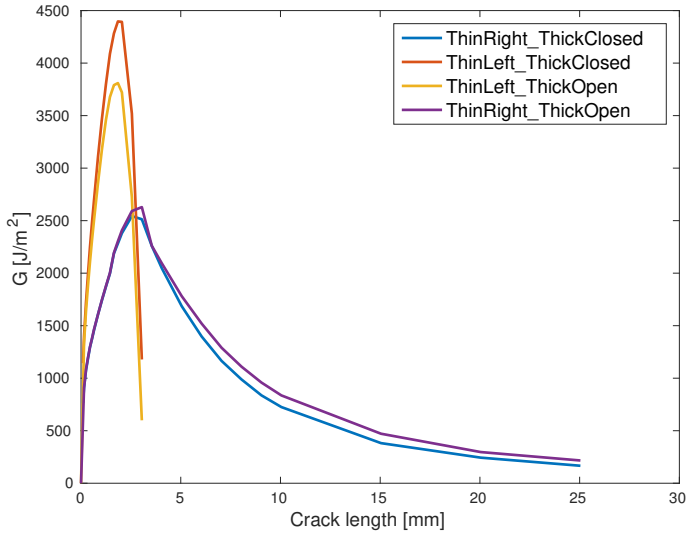

Figure 4.22: G-crack length curves for the thin section.

Based on figure 4.22 it is seen that the length of the cracks of the thick section has small influence on the energy release rates of the cracks in the thin section. Whereas figure 4.21 shows that the cracks in the thin sections have larger influence on the energy release rates of the cracks in the thick section.

4.4 Crack growth simulation

To finish the ply-drop model crack growth is added to the model. Furthermore is the model altered such that l_{fine} is 80 mm and using Q4-elements with incompatible modes in plane-strain with an element size in the fine-region of $\frac{1\text{ mm}}{20}$. Crack growth is implemented based on the Griffith criteria (see section 3.1) and the B-K criterion (see section 3.2). The Griffith crack growth criterion states:

$$G > G_c \Rightarrow \text{Unstable crack growth} \tag{4.2}$$

$$G = G_c \Rightarrow \text{Stable crack growth} \tag{4.3}$$

$$G < G_c \Rightarrow \text{No crack grwoth} \tag{4.4}$$

and the B-K criterion states:

$$G_c = G_{Ic} + (G_{IIc} - G_{Ic})m_2^{\eta} \tag{4.5}$$

The simulation is displacement controlled to simulate the experiments. In the simulation the displacement is increased in steps while growing the crack if $max\left(\frac{G}{G_c}\right) \geq 1$. During the simulation a crack is grown one element at a time after which the analysis is run again with the same displacement. This procedure is repeated until $max\left(\frac{G}{G_c}\right) < 1$ and the displacement is increased. The crack growth implementation includes a special case to handle when the ThinLeft crack is held together by only two nodes. In this case the energy release rate is evaluated by replacing the crack interface with a contact interface instead of growing the crack by one node and when the crack must grow the crack interface is permanently replaced with a contact interface.

The above implementation is inefficient for two reasons. The first reason is the usage of FCEM instead of the J-integral. This choice however made the implementation easier. The second reason is that the FE-solver starts from undeformed state for each analysis. If the FE-solver instead used the deformed state from the previous step as the starting point a significant number of iterations could be saved.

The crack growth simulation is run on an Intel Core I5-4590, a quad core processor clocked at 3.3 GHz. On this hardware the simulation runs for 5 days after which convergences issues are encountered. The convergence issues are probably caused by discontinuties originating from the contact elements however time constraints does not allow further investigation of the issue. Data is however outputted from the simulation between iterations. This data has been plotted in figures 4.23, 4.24 and 4.26.

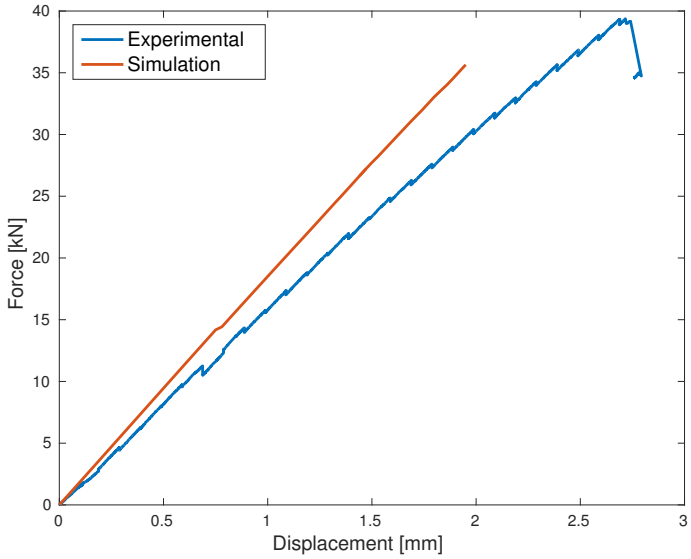

Figure 4.23: Comparison of load-displacement curves obtained experimental and by simulation.

From figure 4.23 it is seen that the simulation response is stiffer than the experimental data. This is probably due to the stiffness of the tensile test machine is included in the experimental data.

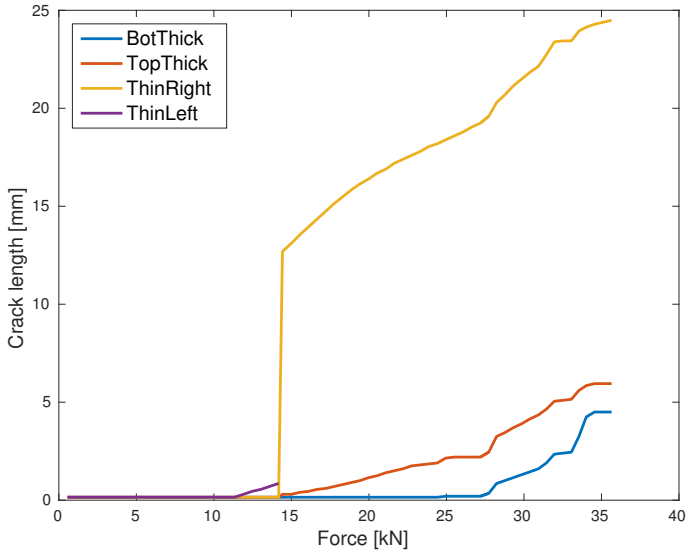

Figure 4.24: Crack lengths vs force obtained from simulations.

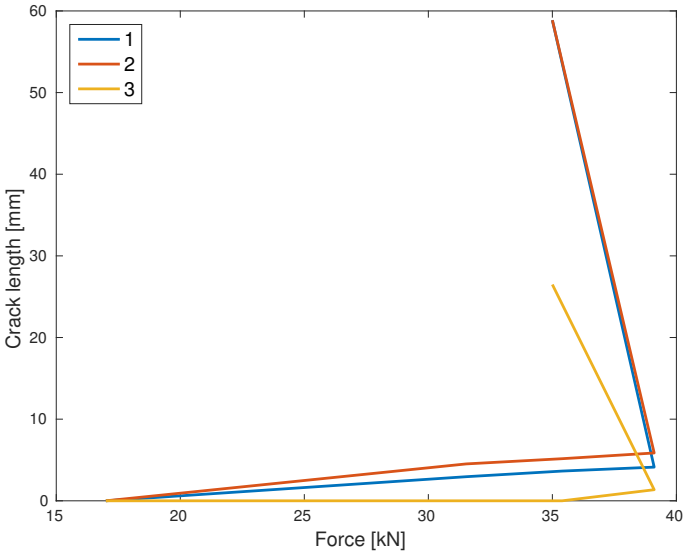

Figure 4.25: Crack lengths vs force obtained experimental.

Figures 4.24 and 4.25 shows crack lengths as a function of load for the simulation and experimental data respectively. From the figures it is seen that the simulation predicts crack growth in the thin section at around 15 kN but the experimental data it does not happen until approximately 35 kN. However better correlation between crack growth exists in the thick section where the simulation predicts approximately 15 kN and the experimental data shows around 17 kN. Furthermore does the crack length in the thick section at around 35 kN have similiar values for simulation and experimental data, around 5 mm. The fact that crack growth in the thin section does not correlate well with the simulation must be related to the geometry deviations in the thin section as shown by the DIC measurements.

Figure 4.26 shows the ratio $\frac{G}{G_c}$. The figure shows a region of unstable crack growth between iteration 50 and 350 where the cracks in the thin section grows which did not occur during experiments. This region is followed by 350 iterations with stable crack growth which fits reasonable well with the experiments. In the last part of the graph a new region of unstable crack growth is initiated. The simulation does not provide further information due to the convergence issues however from the energy release rate curves from section 4.3.3 it is seen that as soon as unstable crack growth is initiated in the thick section of the specimen the cracks will grow until they reach the

boundary. With this consideration it seems reasonable to conclude that the simulation has reached maximum force and that the failure load according to the simulation is 35.7 kN. This is a difference of 3.7 kN $\approx$ 10% between the simulation and experiments which is reasonable.

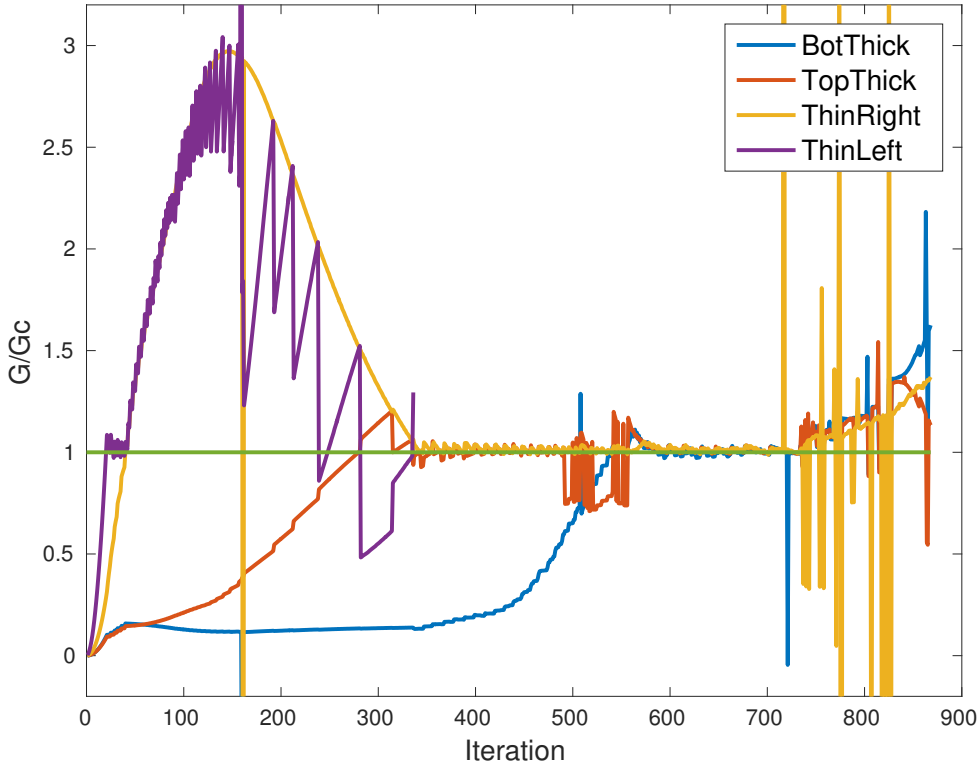

Figure 4.26: G to G_c ratio reveals if crack growth is stable, unstable or no growth occurs.

Overall there are a few parameters that could be a source for error:

Friction In cracks with compressive normal stresses friction could increase the strength of the interface.

Fibre volume fraction The data provided by Agastra [9] is for laminates with a fiber volume fraction of approximately 36.7% wheres the test specimen used in this report is around 55%.

Geometry The simple geometry used causes errors in the thin section when comparing with DIC measurements which will have an effect on the crack growth in the thin section.

Stiffness of tensile test machine The displacement data from the experiments also includes effects from deformation of the tensile test machine which means that the elastic response becomes too soft when comparing with finite element analysis.

Experimental Charactorisation of Failure in Ply-drops in Static Compression

5

The compression experiment deviate from the tension experiment only with respect to the failure hypothesis and the specimen. Due to a reversal of the forces regions with tension becomes regions with compression and vice versa. The force reversal also adds the need for considering buckling.

5.1 Failure Hypothesis for a Ply-drop Test Specimen in Uniaxial Compression

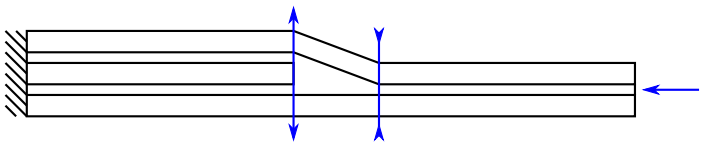

Figure 5.1: Illustration of the tension and compression regions of the ply-drop.

The failure hypothesis is:

1. A crack will initiate in the thick section of the specimen at the top of the ply-drop where opening stresses are present (see figure 2.30).
2. The crack will propagate parallel with the top fibre mat in both directions. The crack will not grow past the compressive stresses (see figure 2.30).
3. The growing crack will cause a redistribution of stresses and eventually the fibres reach the critical stress limit and the specimen fails.

As with the tension tests a USB microscope is used to capture the necessary data.

5.1.1 Specimen Selection

In compression, delamination cuts the laminate into two sublaminates with a combined buckling load lower than that for the complete laminate. This is illustrated in figure 5.2. As it is seen if the delamination grows in the middle of the laminate the height will be halved leading to, in case of a regtangular profile, a decrease of the buckling load with a factor 8.

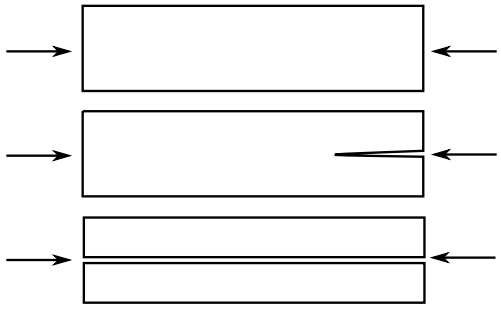

Figure 5.2: Delamination in compression.

If the delamination occur between the outer layers the laminate will not loose as much buckling strength because the laminate thickness is only reduced with one layer thickness. In case of an 11 layer laminate with delamination of the outermost layer the buckling strength will reduce to ≈ 0.75 of the complete laminate.

The dropped ply is therefore located with only one continuous ply above it. 7-1-1 is such a configuration. The buckling load is determined using a geometrical non-linear finite element analysis. The buckling load is found to be approximately -100 kN (see figure 5.3). The tensile test machine is limited to 100 kN and a 7-1-1 specimen should therefore resist buckling.

5.2 Results of Static Compression Test

The results of each of the static compression tests can be seen in appendix C.5, C.6, and C.7. The failure sequence is listed and illustrated in figure 5.4.

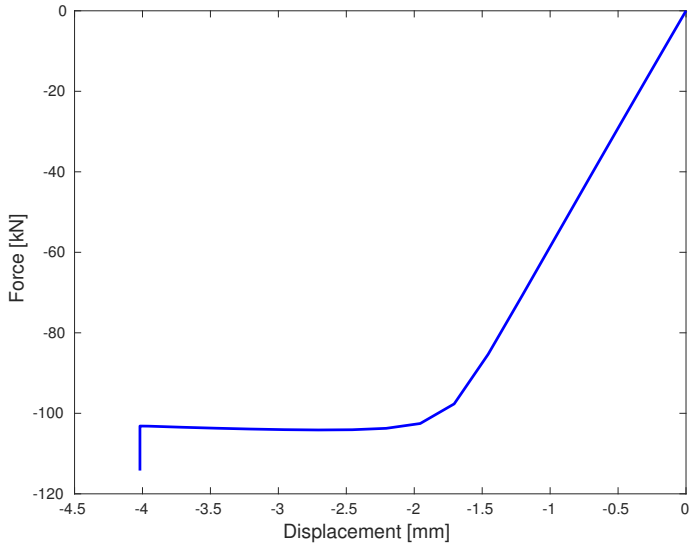

Figure 5.3: A force-displacement curve for a geometrical non-linear analysis indicates a buckling load of approximately -100 kN.

Figure 5.6 shows the different failure steps as pictures taken with the microscope.

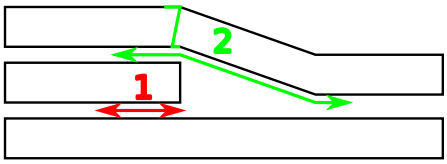

Figure 5.4: Illustration of failure sequence of the 7-1-1 static compression test specimen.

1. A crack initiates at the bottom of the dropped ply.
2. A second crack initiates at the top of the dropped ply and at the same time/load kink-band failure appear below the continuous layer on top of the dropped ply.
3. Further delamination of the top continuous ply and the dropped ply.
4. Delamination between all plies.

The force-displacement curve for test 7-1-1_7 is shown in figure 5.5. The curve shows two failures. The first failure occurs around -1.8 mm and is where the

kink band appears. The next failure occurs around -2.2 mm and is where clamp to clamp delamination in all interfaces happens.

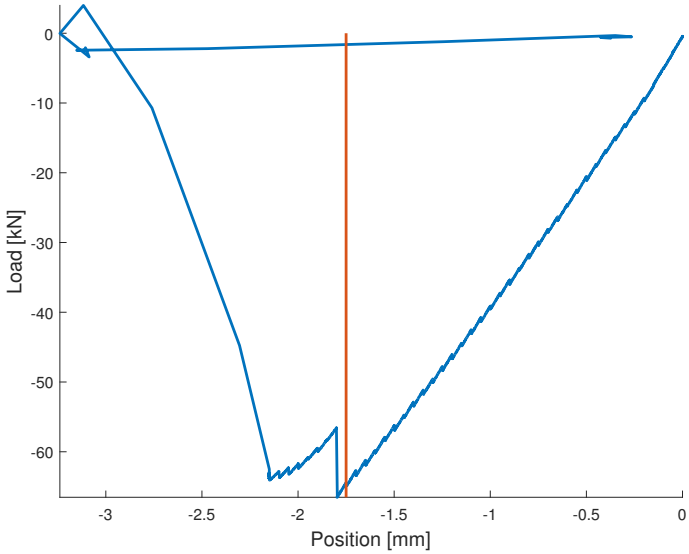

Figure 5.5: Load displacement curve for test 7-1-1_7. The vertical red line indicates the first observed crack.

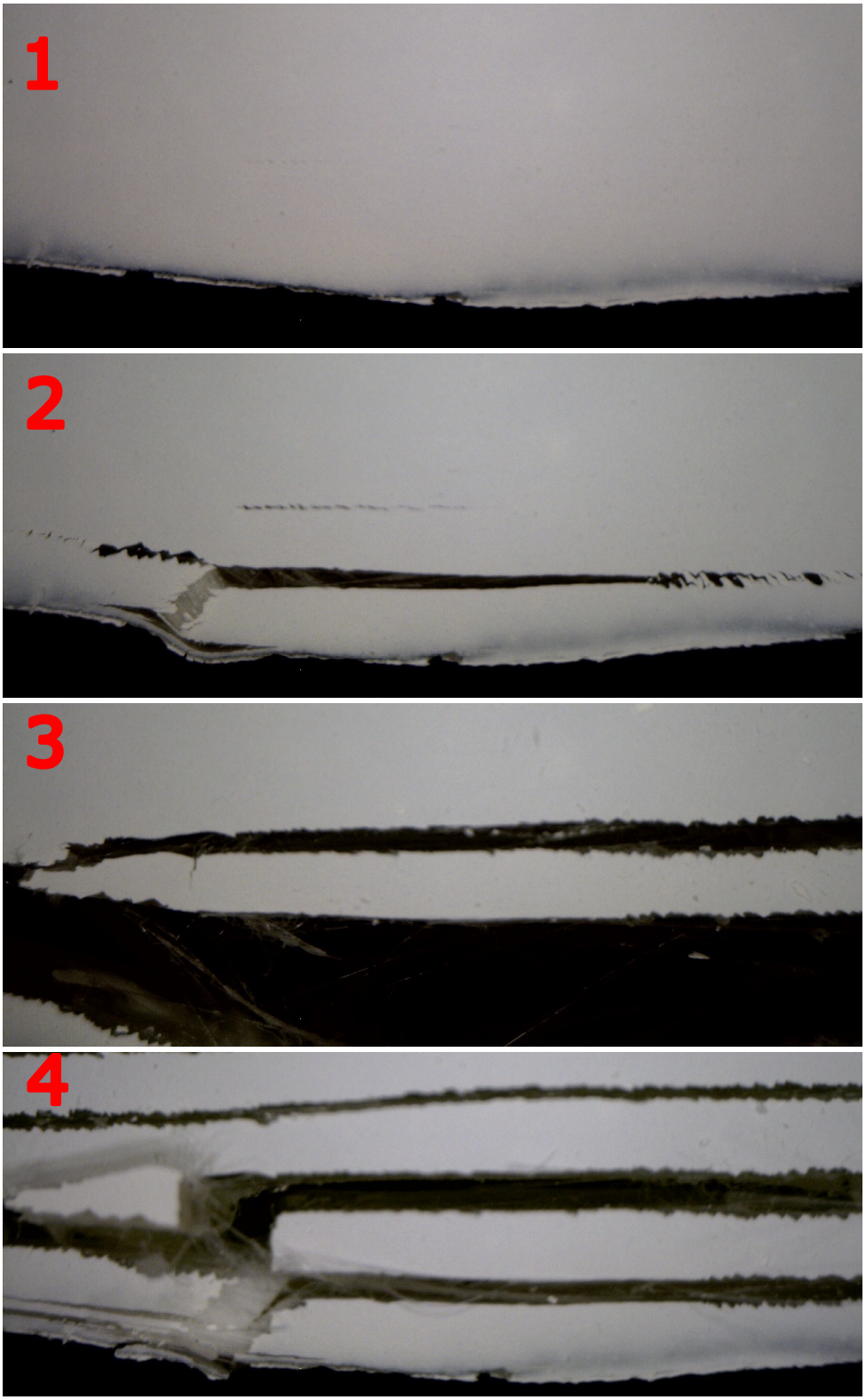

Figure 5.6: Pictures of failure sequence of the 7-1-1_9 static compression test specimen.

European Space Agency [2] has classified 12 possible failure modes for UD composites. Below is explanations of the failure modes observed during the static compression experiment.

Longitudinal compression In the compression specimen kink band was caused by the longitudinal compression. Kink band is illustrated in figure 5.7. Kink band failure mode is shear microbuckling with plastic

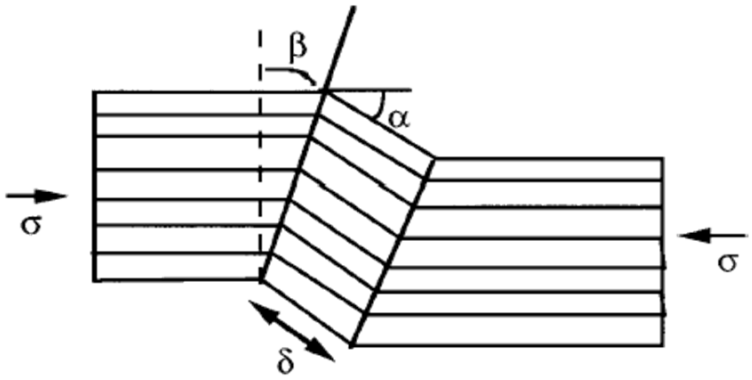

Figure 5.7: Drawings of longitudinal compression failure modes. [3]

deformation of the matrix. This can happen for both a single layer or the laminate.

Short transverse tension This is also known as mode I delamination where a crack opens in tension. This is an interlaminar failure mode where the crack propagates between layers. Even though the crack grows between layers fibre bridging may occur.

Short transverse shear This is also known as mode II delamination where a crack opens in shear. This is an interlaminar failure mode where the crack propagates between layers. Even though the crack grows between layers fibre bridging may occur.

5.3 Conclusion of Static Compression Test

The following parts of the failure hypothesis showed to be incorrect.

1. *A crack will initiate in the thick section of the specimen at the top of the ply-drop where opening stresses are present (see figure 2.30).* A crack initiates at the bottom of the dropped ply.

2. *The crack will propagate parallel with the top fibre mat in both directions. The crack will not grow past the compressive stresses (see figure 2.30).* A kink-band failure at the top ply and at the same time delamination occurs between the top ply. The crack at the bottom of the dropped ply is propagating.
3. *The growing crack will cause a redistribution of stresses and eventually the fibres reach the critical stress limit and the specimen fails.* Delamination between all plies occurs and no fibre breakage is observed.

All in all the governing failure modes for a laminate with a ply-drop loaded in compression are delamination and kink-band.

Fatigue Tests 6

Every structure is exposed to fatigue loadings. It is therefore necessary to examine the fatigue properties of laminates with ply-drops. Furthermore, the failure sequence can be different in fatigue when compared to static loadings. The purpose of the fatigue test is to achieve a failure sequence of the ply-drop test specimen loaded in fatigue and achieve and initial guess on the slope of the SN-curve.

6.1 Failure Hypothesis for a Ply-drop Test Specimen in Fatigue

The failure hypothesis in fatigue is obtained from the failure sequence for the static tests in 2.3.2 for tension and 5.2 for compression. The last step in the failure sequence is omitted because the specimens will break apart and thereby it is not possible to inspect the specimens after the test.

Failure hypothesis for ply-drop test specimen in fatigue tension

1. A crack initiates in the interface between the dropped ply and the resin pocket.
2. The crack at the end of the dropped ply extends in both directions causing crack growth into the thick section of the ply-drop both above and below the dropped ply. These cracks grows as the cycles increases.
3. A new crack appears where the top ply meets the bottom ply.
4. All cracks grow leading to delamination. The cracks along the dropped ply grows until the clamps of the tensile test machine while the last crack grows approximately half way to the clamps in the thin section of the specimen.

Failure hypothesis for ply-drop test specimen in fatigue compression

1. A crack initiates at the bottom of the dropped ply.
2. A second crack initiates at the top of the dropped ply and at the same time/load kink-band failure appear at the layer on top of the dropped ply.
3. Further delamination of the top ply and the dropped ply.

6.2 Method of Testing

The method of testing is based on using the same equipment and data acquisition as used in the static tests. The specimens are painted white on the sides to increase the contrast and crack growth is captured with an USB microscope. To protect the specimen from final failure a stopping criterion is implemented. The stopping criterion is defined such that the test stops as soon as the stiffness of the specimen falls below the stiffness equivalent to a fully delaminated specimen. This is shown in figure 6.1. The displacement

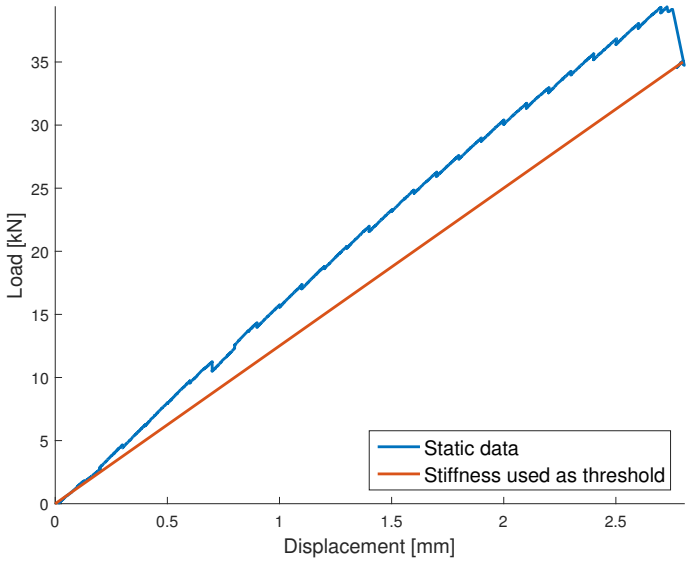

Figure 6.1: Plot of decreased stiffness for threshold in fatigue test.

threshold $U_{threshold}$ is calculated using equation (6.1).

$$U_{threshold} = \frac{F_{endS}}{U_{endS}} \cdot F_{MaxF} \tag{6.1}$$

Where F_{endS} is the final force value of the static test, U_{endS} the final displacement value of the static test and F_{MaxF} is the maximum force applied in the fatigue test.

The test sequence is:

1. Take a picture of the specimen in unloaded state.
2. Set up the test sequence with the mean and amplitude load, number of cycles per loop, number of loops and displacement threshold.
3. Set up the digital microscope to make a time lapse.
4. Start the test and time lapse at the same time.
    a) Load the specimen to the mean load.
    b) Run the number of cycles specified.
    c) Load the specimen to the mean load and hold for one minute while a picture is taken.
    d) Repeat until the displacement threshold is achieved or the maximum number of loops is reached.

6.3 Tension Fatigue Results

All the tension fatigue tests is conducted with the 1-1-1 test specimens. The results are listed in table 6.1. The specimens after testing are shown in figure 6.2.

Identifier	Max load [kN]	Min load [kN]	Hit $U_{threshold}$	Cycles	Frequency [Hz]
1-1-1_10	10	1	No	1690000	5-10
1-1-1_11	10	1	Yes	1620738	7
1-1-1_12	10	1	No	1197305	7
1-1-1_13	15	1.5	Yes	64913	7
1-1-1_14	10	1	No	2780000	10
1-1-1_15	15	1.5	Yes	118674	7
1-1-1_16	12.5	1.25	Yes	881724	7
1-1-1_17	12.5	1.25	Yes	255970	7

Table 6.1: Tension fatigue results

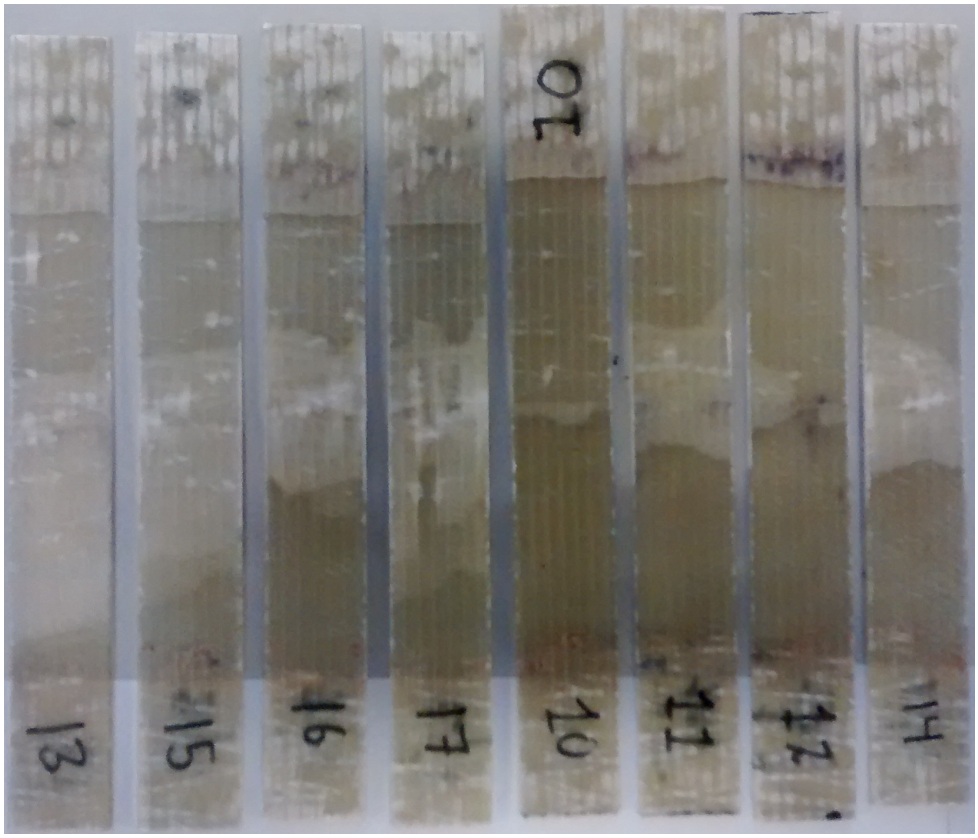

Figure 6.2: Fatigue tension test specimens.

The failure sequence of the fatigue tension test is illustrated in figure 6.3 and is:

1. A crack appears in the interface between the dropped ply and the resin pocket.
2. The crack at the end of the dropped ply extends in both directions causing crack growth into the thick section of the ply-drop both above and below the dropped ply.
3. After step two the tests show different failure sequences. For specimen 1-1-1_11 and 1-1-1_17 a new crack initiates where the top ply meets the bottom ply. For specimen 1-1-1_10 and 1-1-1_13 the crack at the end of the dropped ply changes direction and grows at the bottom of the dropped ply and at the underside of the resin pocket. For specimen 1-1-1_14 and 1-1-1_15 the crack at the end of the dropped ply splits into a crack growing in both directions along the top ply.
4. All cracks grow leading to delamination. The cracks along the dropped ply grows until the threshold value is reached. The delamination is not always all the way down to the clamps. Only exception the specimens loaded at 10 kN where the crack at the bottom of the dropped ply propagates significantly less than with the other loads.

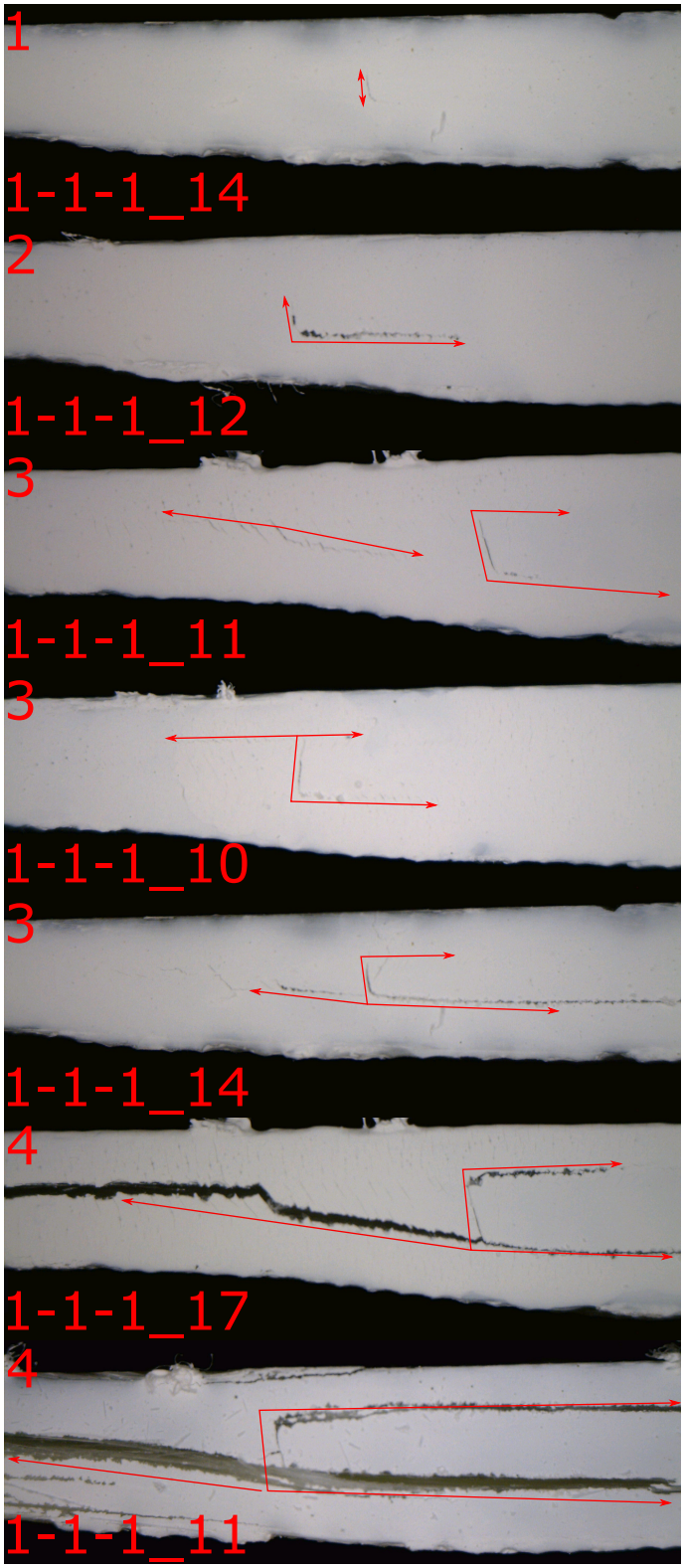

Figure 6.3: Failure sequence of fatigue tension test specimens.

Observations

The only test of the ones loaded with 10 [kN] that hit the threshold is 1-1-1_11 even though as it is seen in figure 6.2 1-1-1_14 has close to the same delamination. The delamination length is different in the specimens that reached the displacement threshold. This could be because damage occurs elsewhere than around the ply-drop. Specimen 1-1-1_17 has damage/cracks inbetween the fibre bundles, all specimens have damage around backing fibres most easily seen in specimen 1-1-1_13.

The failure modes observed during tension loadings in fatigue are identical to the ones observed during static testing.

SN-curve

The data is plotted in a SN-curve and a curve fit is made with the power law shown in equation (6.2).

$$\Delta\sigma = A \cdot (N)^b \tag{6.2}$$

Where A is the stress range at $N = 1$, b the slope, N the number of cycles and $\Delta\sigma$ the average stress range for the thin section of the ply-drop specimen.. The SN-curve data and the fit is plotted in figure 6.4. The slope is -0.1112 and the intercept is 946. The slope is similar to the slope of a neat laminate which according to Sutherland [14] is between -0.14 and -0.1.

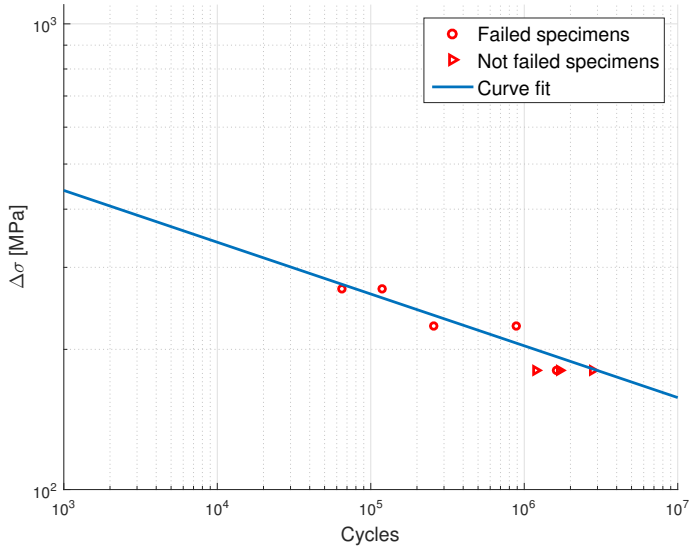

Figure 6.4: SN-curve of the fatigue tension tests R=0.1.

6.4 Compression Fatigue Results

All the compression fatigue tests is conducted with the 7-1-1 test specimens. The results are listed in table 6.2. The specimens after testing are shown in figure 6.5. None of the test specimen hit the threshold calculated from the static test. This could be because there are slight buckling in the static tests after failure and thereby leading to a less stiff specimen when the top ply is delaminated compared to the to a fatigue test specimen with the top ply delaminated. Therefore the tests were stopped manually.

Identifier	Max load [kN]	Min load [kN]	Hit $U_{threshold}$	Cycles	Frequency [Hz]
7-1-1_18	-3	-30	No	194178	3
7-1-1_19	-3	-30	No	370324	6
7-1-1_20	-2	-20	No	2590000	10
7-1-1_21	-2.5	-25	No	2794000	6
7-1-1_22	-2.75	-27.5	No	3276000	6
7-1-1_23	-2.75	27.5	No	2383571	10

Table 6.2: Compression fatigue results

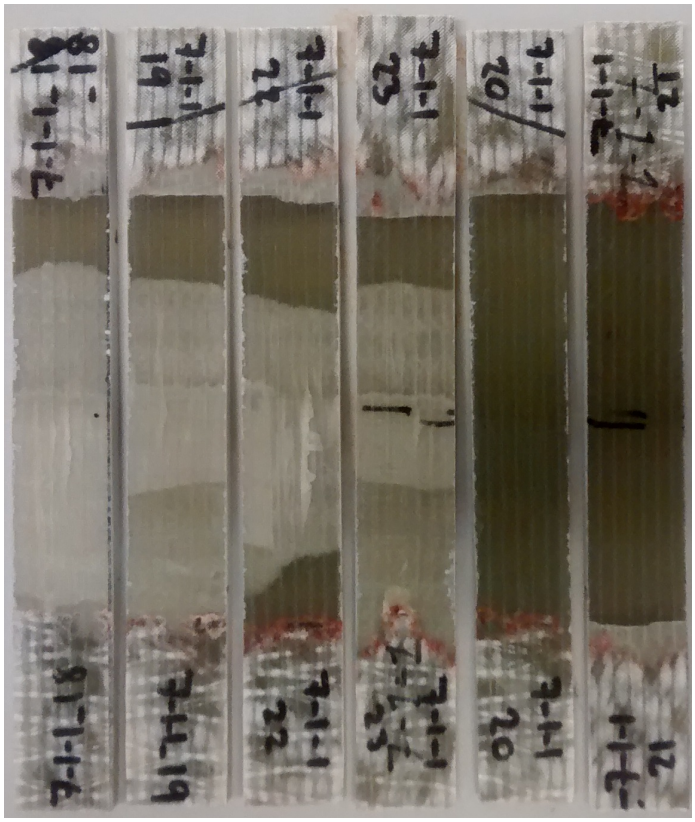

Figure 6.5: Fatigue compression test specimens.

The failure sequence of the fatigue compression test is illustrated in figure 6.6 and is:

1. A crack initiates at the bottom of the dropped ply.
2. The crack at the bottom of the dropped ply propagates in both directions.
3. A new crack initiates at the top of the dropped ply and grows along the top ply to the bottom crack.
4. Further delamination of the top ply and the dropped ply.

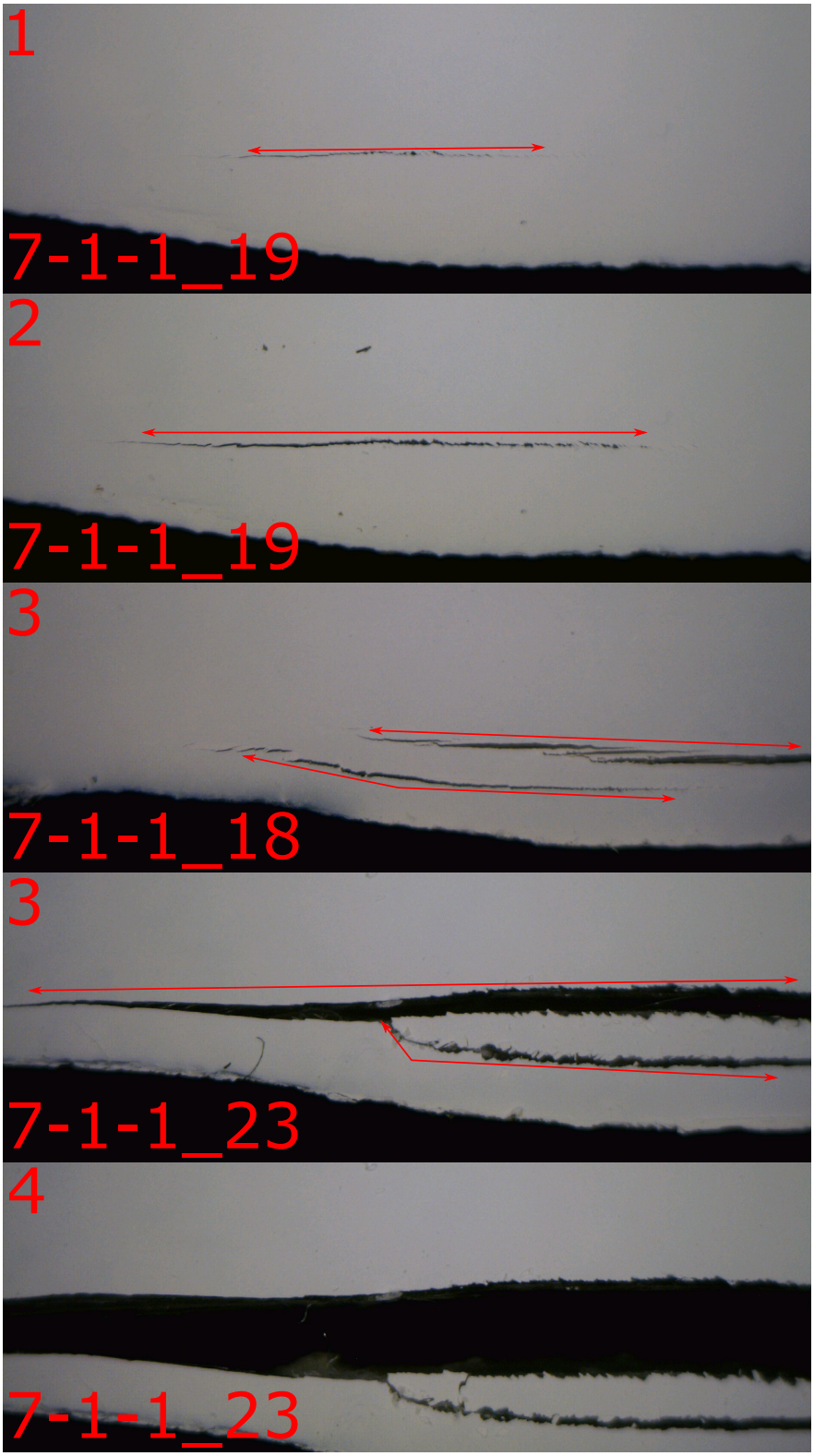

Figure 6.6: Failure sequence of fatigue compression test specimens.

Observations

There is no kink-band failure in the fatigue tests. The remaining failure modes are similar with the static tests. The 7-1-1_22 specimen has damage between the fibre bundles because the delamination did not occur equally across the width of the specimen.

SN-curve

The data is plotted in a SN-curve and a curve fit is made with the power law shown in equation (6.2). The SN-curve data and the fit is plotted in figure 6.7. The slope is -0.03531 and the intercept is 210. The slope is lower than the slope of a neat laminate which according to Sutherland [14] is between -0.07 and -0.11.

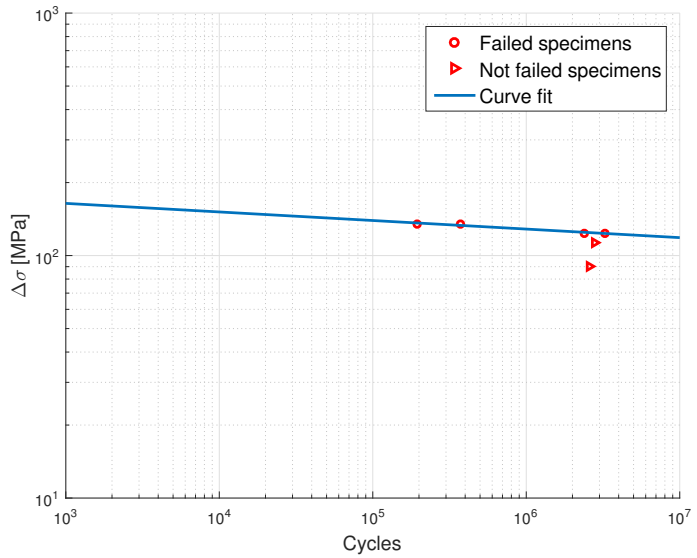

Figure 6.7: SN-curve of the fatigue compression tests R=10.

7 Conclusion

To analyse ply-drops in composite structures both experimental and numerical methods were used. The experimental tests were conducted at the facilities and with the means available at the Department of Mechanical and Manufacturing Engineering at Aalborg University.

The experimental tests were conducted with an USB microscope observing the crack initiation and propagation from the side of the specimen. The specimens were painted white to increase the contrast thereby making it easier to study the cracks. However some problems with the data acquisition during especially the fatigue tests were seen. The crack did not grow equally on both sides of the specimen and in some of the tests the cracks initiated and grew in one side before expanding across the width of the specimen.

Another hurdle was the paint. The paint was too elastic or not brittle enough and thereby hiding the crack masking the true cycle count for crack initiation and growth.

The results from the experimental tests were that delamination was the governing failure mode. Furthermore were the experiments used to determine failure loads for both tension and compression tests. The delamination expand from the crack that initiates at the end of the dropped ply in the static tension tests. The initial failure of the compression tests is delamination that originates from below the dropped ply.

The failure modes in the static and fatigue tension tests were similar. A difference between the failure modes during compressive static and fatigue loadings was observed. There was no kink-band failure in the fatigue compression tests.

Several different methods were used to model the crack propagation, but each of them had advantages and drawbacks. The modelling technique that proved most successful was FCEM in combination with VCCT. FCEM was used to

calculate the energy release rates and VCCT to calculate the mode mixity. VCCT can not be used to calculate the energy release rates because of the bi-material interface causing oscillating stresses in front of the crack tip, but it is used as the only option to calculate the mode mixity. FCEM is an expensive method since it requires one plus the number of cracks simulations. CZM has the benefit of being able to predict both crack initiation and propagation but had convergence issues that could not be solved within the given time frame.

The results of the FE-modelling showed agreement between the elastic response of the FE-model and the DIC-measurements. This agreement was obtained using inverse modelling on the FE-model by minimising the error between the DIC-measurements and the FE-model by optimising geometrical and material parameters.

The crack growth model is successful in capturing the crack growth in the thick section of the ply-drop. It does also predict the failure load of the ply-drop within 10% on the conservative side. It does however not predict the crack growth in the thin section very well. The convergence issues however shows that the model still needs work before it can be used in industry.

One source of error is that friction has not been included in the FE-model even though is must be present in the specimen due to compressive forces. If this friction is modelled it should increase the failure load of the model. Another source of error is the simplified geometry where it increases the tractions in the thin section of the ply-drop and thereby leading to crack growth at a lower load.

Future Work 8

The future work that can be performed in relation to this project is outlined below.

The crack growth model is expensive taking five days to run and this could be made more efficient by implementing the starting guess from the last or base simulation to the current simulation. This should lower the number of equilibrium iterations needed to achieve the solution. Another method could be that more than one node should be loosened at each iteration. The crack at the inclined section at the resin pocket could maybe be neglected and thereby saving one simulation at each iteration.

The method for determining the energy release rate could be exchanged with the J-integral. The J-integral is a path independent integral and can therefore be evaluated away from the crack tip.

This project focused on UD laminates with ply-drops but composite structures are rarely made of pure UD. It would therefore be of interest to examine the effect of different lay-ups. Thereby the model would become more general by being able to predict the behaviour and strength of universal composite structures.

Since data already has been obtained for a ply-drop in compression a new model based on the work done with the tension test could be developed for the compression tests. If this is done new models could be developed for other load or mixed load situations. The same argument can be made for the fatigue tests where the model can be expanded to be able to predict the crack growth as a result of fatigue loading.

If the FE-model can be optimised with respect to computational power a parametric study could be performed. The parametric study can be used for design guidelines on what tolerances is necessary to keep the strength intact. This could be further expanded into a 3D model to study the effects of for

example fibre-alignment or distortions of the fibre mat.

In the model friction was neglected this could be introduced into the model and should increase the accuracy of the model but increase the computation time. There would be a problem with obtaining the friction coefficients since there is fibre bridging and other effects.

In the fatigue test it was observed that the crack front was not growing evenly across the width of the specimen. Therefore the experimental set-up could be changed to either have a camera on both sides or have an extra camera at the front. Having an extra camera at the front would make it possible to evaluate the total delamination, but it would require good illumination to be able to differentiate between the cracks.

At last a model with several ply-drops could be analysed and thereby the current "rule of thumb", of the length between ply-drops should be ten times the thickness change, could be verified or a new proposed.

Bibliography

[1] R. Jones. Mechanics of Composite Materials. Taylor & Francis, 1998. ISBN 1-56032-712-X.

[2] European Space Agency. Structural materials handbook - Part 2: Design calculation methods and general design aspects. ESA Requirements and Standards Division, 2011.

[3] Erik Lund and Lars Overgaard. Mechanics of composite materials and structures, 2015.

[4] ESAComp. ESAComp - DataBank, 2016.

[5] A. S. Kaddour and M. J. Hinton. Maturity of 3D failure criteria for fibre-reinforced composites: Comparison between theories and experiments: Part B of WWFE-II. Journal of Composite Materials, 47: 925–966, 2013.

[6] Jens Henrik Andreasen. Fracture mechanics, 2014.

[7] A.T. Zehnder. Fracture Mechanics. Springer, 2012.

[8] Dassault systèmes. Abaqus 6.14 Documentation, 2014.

[9] Pancasatya Agastra. Mixed mode delamination of glass fiber/polymer matrix composite materials. Master's thesis, MONTANA STATE UNIVERSITY—BOZEMAN, 2004.

[10] D. Carrella-Payan, L.F. Kawashita, and G. Allegri. Tensile testing characterization of asymmetrically tapered composite laminates. 18th International Conference on Composite Materials, 2011.

[11] Erik Lund and Esben Lindgaard. Finite element methods, 2014.

[12] C.T. Sun and C.J. Jih. On strain energy release rates for interfacial cracks in bi-material media. Engineering Fracture Mechanics, 28:13–20, 1987.

[13] M.L. Williams. The stresses around a fault or crack in dissimilar media. Bulletin of the Seismological Society of America, 49:199–204, 1959.

[14] Herbert J. Sutherland. A summary of the fatigue properties of wind turbine materials. Technical report, Sandia National Laboratories Wind Energy Technology Department, 1999.

Weight of Fibre Mat A

The data for calculating the weight per square meter of the mat is listed in table A.1. The width is measured at the roll with mats and the length is measured when the section is cut off.

Name	Value	Unit
Length	300	[mm]
Width	800	[mm]
Weight	0.343	[kg]
Weight per square meter	1.429	$\left[\mathrm{kg/m^2}\right]$

Table A.1: Data for calculating the weight per square meter for the glass fibre mat.

Production Data B

This appendix contains the sizes of material used for the infusion chambers. It also contains the data needed for calculating the fibre volume fraction.

B.1 Materialplate

Name	Total number	Length	Width	Unit
Aluminium plate	1	>700	>700	[mm]
Slip foil	1	600	600	[mm]
Fibre mats	4	600	600	[mm]
Peel ply	1	610	610	[mm]
Distribution medium	1	500	500	[mm]
Vacuum bag	1	>800	>800	[mm]

Table B.1: Sizes of infusion chamber layers for the material plate

Name	Value	Unit
$m_{specimenIN}$	92.05e-3	[kg]
$m_{specimenOUT}$	97.65e-3	[kg]
$m_{bucketIN}$	263.14e-3	[kg]
$m_{bucketOUT}$	262.64e-3	[kg]
$m_{afterBurnIN}$	330.30e-3	[kg]
$m_{afterBurnOUT}$	335.80e-3	[kg]
V_f^{in}	58.1 %	
V_f^{out}	55.6 %	

Table B.2: Data for calculating volume fractions of the material plate.

B.2 Ply-drop Plate 1-1-1 130316

Name	Total number	Length	Width	Unit
Aluminium plate	1	>500	>300	[mm]
Slip foil	1	400	200	[mm]
Fibre mats	2	400	200	[mm]
Fibre mats	1	200	200	[mm]
Fibre mats	1	150	200	[mm]
Peel ply	1	420	210	[mm]
Distribution medium	1	350	180	[mm]
Vacuum bag	1	>600	>400	[mm]

Table B.3: Sizes of infusion chamber layers for the ply-drop plate 1-1-1 130316.

Name	Value	Unit
$m_{specimenIN}$	56.69e-3	[kg]
$m_{specimenOUT}$	71.71e-3	[kg]
$m_{bucketIN}$	222.77e-3	[kg]
$m_{bucketOUT}$	222.19e-3	[kg]
$m_{afterBurnIN}$	263.80e-3	[kg]
$m_{afterBurnOUT}$	274.80e-3	[kg]
V_f^{in}	54.9 %	
V_f^{out}	56.1 %	

Table B.4: Data for calculating volume fractions of ply-drop plate 1-1-1 130316.

B.3 Ply-drop Plate 7-1-1 230316

Name	Total number	Length	Width	Unit
Aluminium plate	1	>500	>300	[mm]
Slip foil	1	400	200	[mm]
Fibre mats	8	400	200	[mm]
Fibre mats	1	200	200	[mm]
Fibre mats	1	150	200	[mm]
Peel ply	1	420	215	[mm]
Distribution medium	1	350	180	[mm]
Vacuum bag	1	>600	>400	[mm]

Table B.5: Sizes of infusion chamber layers for the ply-drop plate 7-1-1 230316.

Name	Value	Unit
$m_{specimenIN}$	169.24e-3	[kg]
$m_{specimenOUT}$	200.94e-3	[kg]
$m_{bucketIN}$	222.42e-3	[kg]
$m_{bucketOUT}$	221.82e-3	[kg]
$m_{afterBurnIN}$	346.51e-3	[kg]
$m_{afterBurnOUT}$	370.83e-3	[kg]
V_f^{in}	55.7 %	
V_f^{out}	57.1 %	

Table B.6: Data for calculating volume fractions of ply-drop plate 7-1-1 230316.

B.4 Ply-drop Plate 1-1-1 120416

Name	Total number	Length	Width	Unit
Aluminium plate	1	>500	>300	[mm]
Slip foil	1	400	200	[mm]
Fibre mats	2	400	200	[mm]
Fibre mats	1	200	200	[mm]
Fibre mats	1	150	200	[mm]
Peel ply	1	420	210	[mm]
Distribution medium	1	350	180	[mm]
Vacuum bag	1	>600	>400	[mm]

Table B.7: Sizes of infusion chamber layers for the ply-drop plate 1-1-1 120416.

Name	Value	Unit
$m_{specimenIN}$	67.24e-3	[kg]
$m_{specimenOUT}$	72.28e-3	[kg]
$m_{bucketIN}$	222.34e-3	[kg]
$m_{bucketOUT}$	221.97e-3	[kg]
$m_{afterBurnIN}$	271.12e-3	[kg]
$m_{afterBurnOUT}$	273.93e-3	[kg]
V_f^{in}	55.1 %	
V_f^{out}	54.3 %	

Table B.8: Data for calculating volume fractions of ply-drop plate 1-1-1 120416.

B.5 Ply-drop Plate 1-1-1 220416

Name	Total number	Length	Width	Unit
Aluminium plate	1	>500	>300	[mm]
Slip foil	1	400	200	[mm]
Fibre mats	2	400	200	[mm]
Fibre mats	1	200	200	[mm]
Fibre mats	1	150	200	[mm]
Peel ply	1	420	210	[mm]
Distribution medium	1	350	180	[mm]
Vacuum bag	1	>600	>400	[mm]

Table B.9: Sizes of infusion chamber layers for the ply-drop plate 1-1-1 220416.

Name	Value	Unit
$m_{specimenIN}$	69.83e-3	[kg]
$m_{specimenOUT}$	76.06e-3	[kg]
$m_{bucketIN}$	222.63e-3	[kg]
$m_{bucketOUT}$	221.96e-3	[kg]
$m_{afterBurnIN}$	273.01e-3	[kg]
$m_{afterBurnOUT}$	277.37e-3	[kg]
V_f^{in}	54.6 %	
V_f^{out}	55.5 %	

Table B.10: Data for calculating volume fractions of ply-drop plate 1-1-1 220416.

B.6 Ply-drop Plate 7-1-1 220446

Name	Total number	Length	Width	Unit
Aluminium plate	1	>500	>300	[mm]
Slip foil	1	400	200	[mm]
Fibre mats	8	400	200	[mm]
Fibre mats	1	200	200	[mm]
Fibre mats	1	150	200	[mm]
Peel ply	1	420	215	[mm]
Distribution medium	1	350	180	[mm]
Vacuum bag	1	>600	>400	[mm]

Table B.11: Sizes of infusion chamber layers for the ply-drop plate 7-1-1 220146.

Name	Value	Unit
$m_{specimenIN}$	177.15e-3	[kg]
$m_{specimenOUT}$	227.46e-3	[kg]
$m_{bucketIN}$	222.15e-3	[kg]
$m_{bucketOUT}$	221.67e-3	[kg]
$m_{afterBurnIN}$	352.60e-3	[kg]
$m_{afterBurnOUT}$	391.72e-3	[kg]
V_f^{in}	56.5 %	
V_f^{out}	57.9 %	

Table B.12: Data for calculating volume fractions of ply-drop plate 7-1-1 220146.

Static Test Campaign C

For the static tests the loading is performed stepwise, in increments in displacement, because it has been observed that the crack needs time to develop. Cracks has grown under the waiting periods of the test. The specimen is loaded using prescribed displacement because cracks grow more stable under prescribed displacement than prescribed load. A USB microscope is used to capture cracks in the specimen. The specimen is painted with white paint on the edges to increase contrast to make the crack easier to observe.

The test procedure is:

1. Take a picture without paint
2. Paint specimen
3. Take a picture with paint
4. Start the loading sequence and the photo time-lapse simultaneous
    a) Wait 10 seconds
    b) Increase displacement
    c) Wait 50 seconds
5. Stop testing when delamination has occurred

The results from the static tests are presented on the following pages. Each test is described using the same format except for test 7-1-1_6 because the crack grew opposite of the USB microscope.

The format is: First pictures of the front and back of the specimen where the thick section is on the right side of the specimen. Next a picture combining a picture of the unpainted specimen with a picture where the crack is initiated. This will allow to view the location of the crack with respect to the plies. This is followed by a load-displacement curve where crack initiation is marked using a red line. The crack initiation is determined by examining the microscope pictures for areas where darkening appears. Lastly a four frame summary of the crack development is shown.

C.1 Test 1-1-1_1

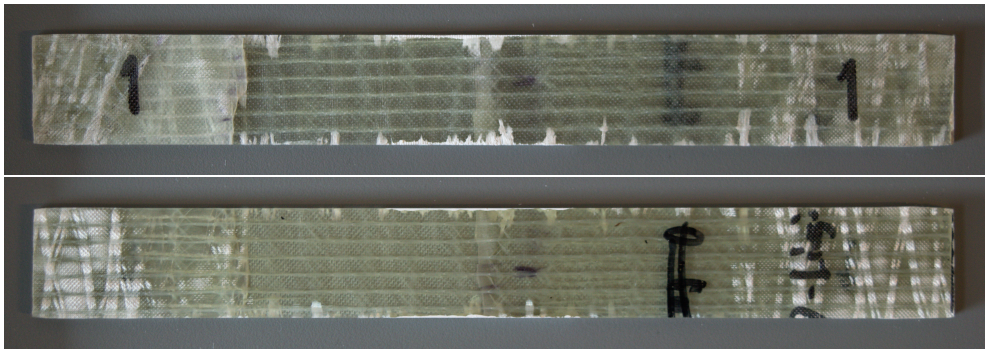

Figure C.1: Top picture is front view and bottom picture is back view of specimen 1-1-1_1 after testing has been performed.

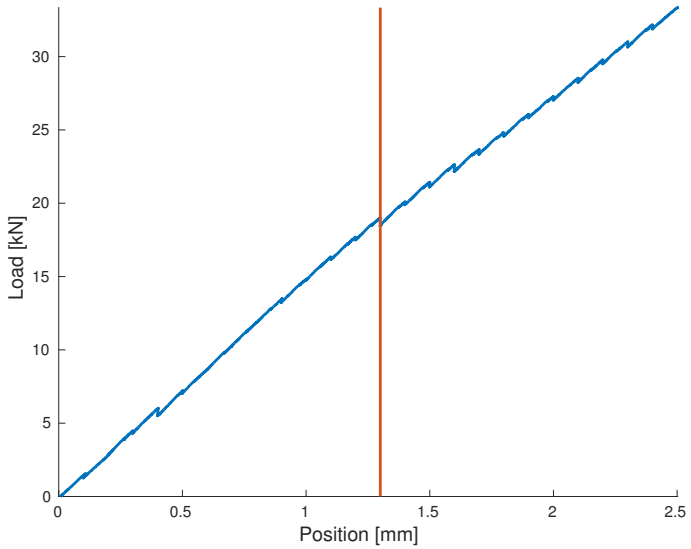

Figure C.2: Load displacement curve for the test. The vertical red line indicates the first observed crack.

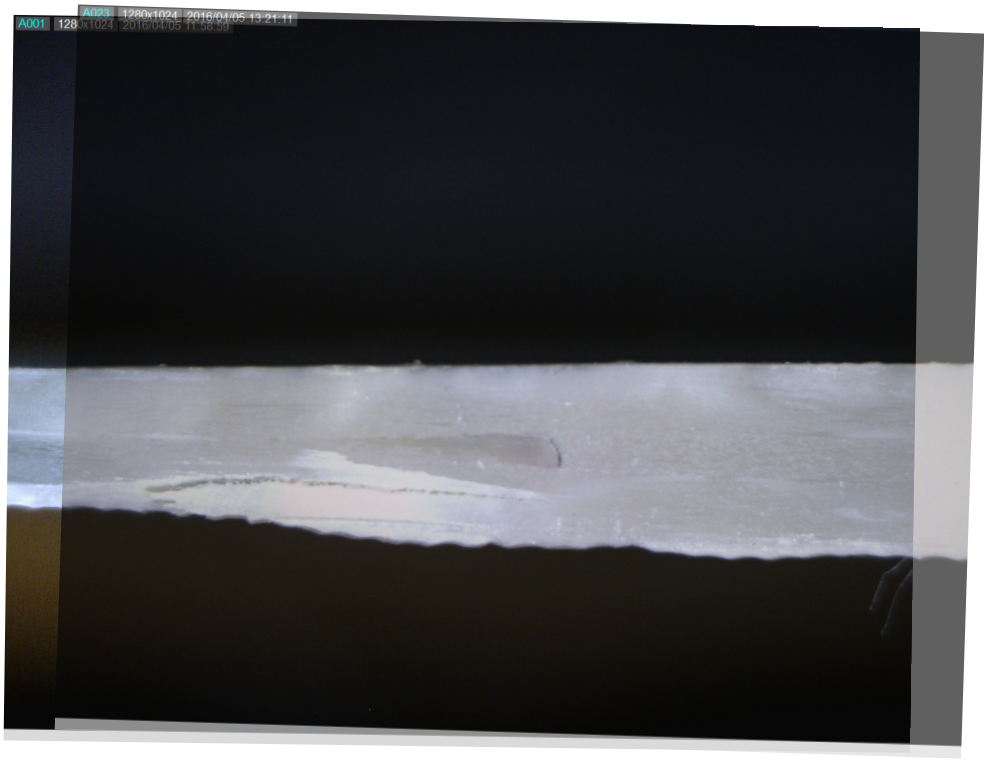

Figure C.3: Picture with cracks overlayed on the unpainted specimen. A crack is seen in front of the dropped ply and in the top layer (bottom of the picture).

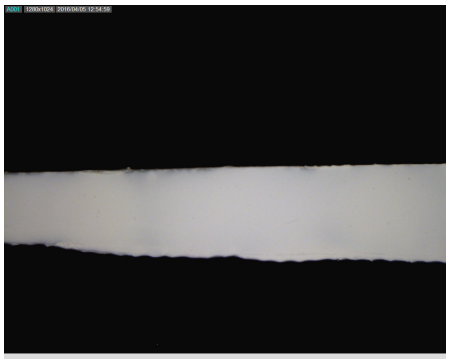

Figure C.4: Specimen in unloaded state.

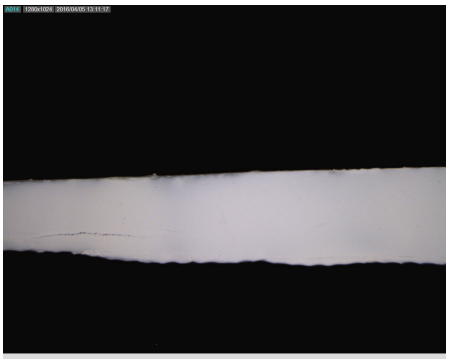

Figure C.5: Specimen at 1.3 mm displacement.

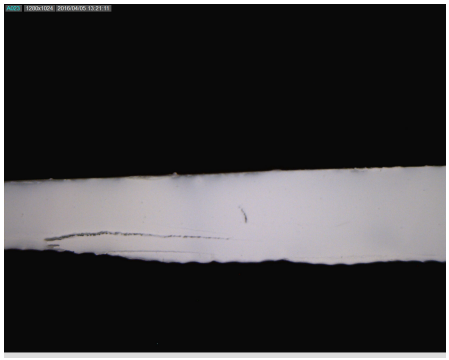

Figure C.6: Specimen at 2.2 mm displacement.

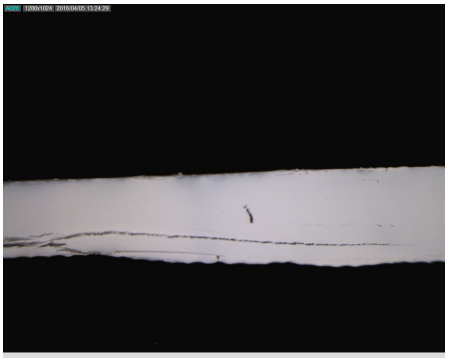

Figure C.7: Specimen at 2.5 mm displacement.

C.2 Test 1-1-1_2

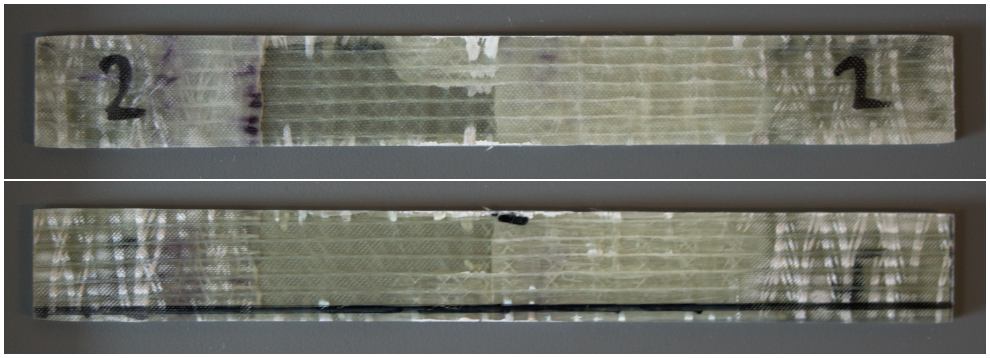

Figure C.8: Top picture is front view and bottom picture is back view of specimen 1-1-1_2 after testing has been performed.

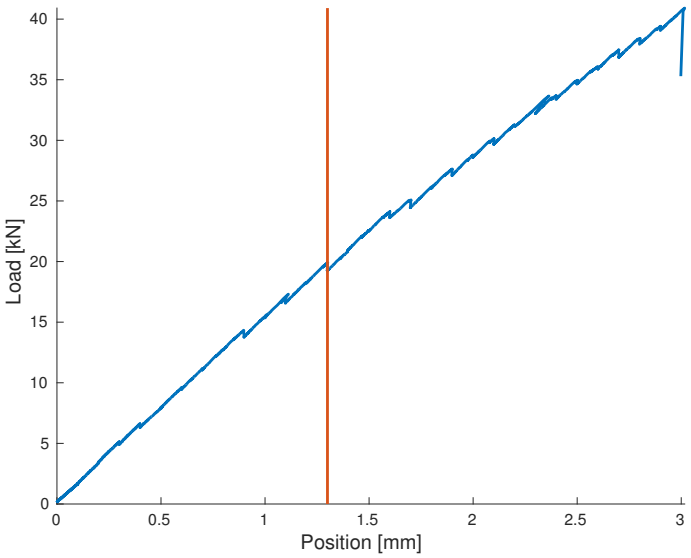

Figure C.9: Load displacement curve for the test. The vertical red line indicates the first observed crack.

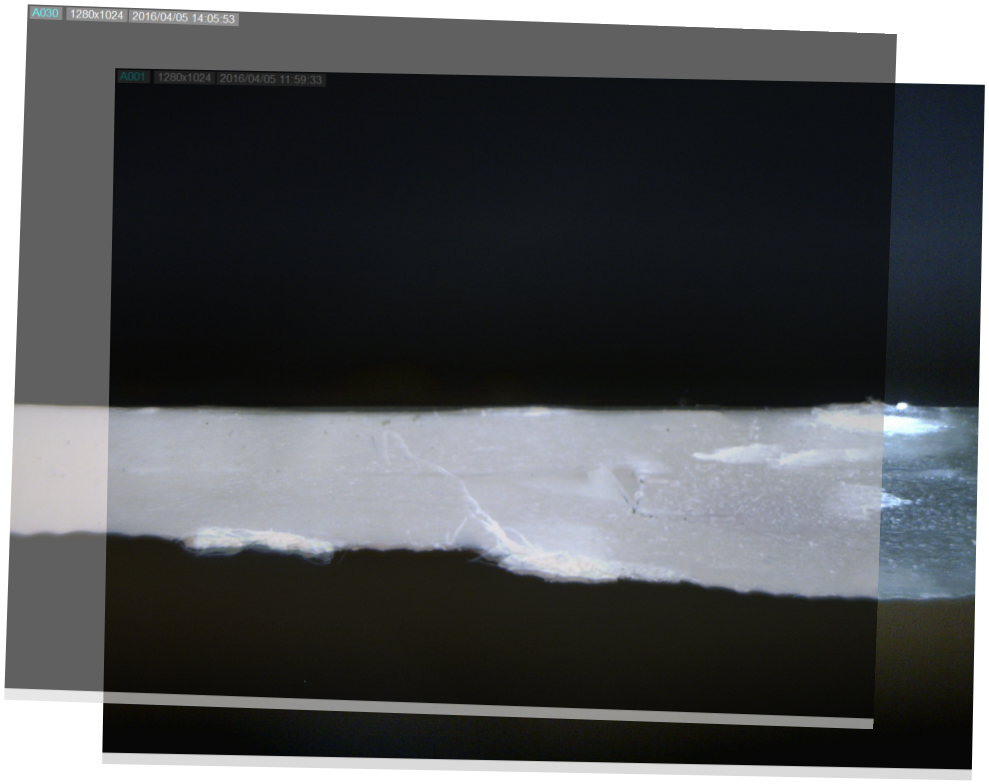

Figure C.10: Picture with cracks overlayed on the unpainted specimen. A crack is seen in front of the dropped ply and one a little ahead of the dropped ply.

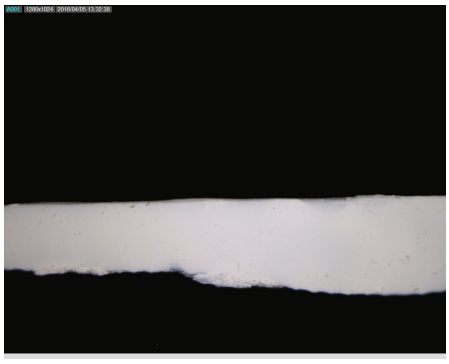

Figure C.11: Specimen in unloaded state.

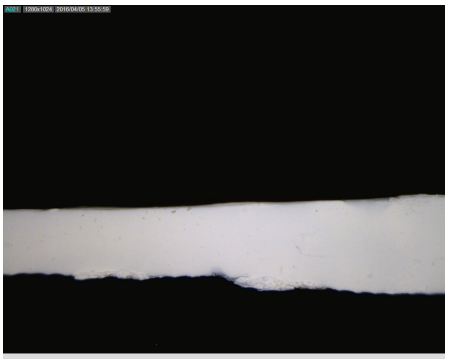

Figure C.12: Specimen at 2.0 mm displacement.

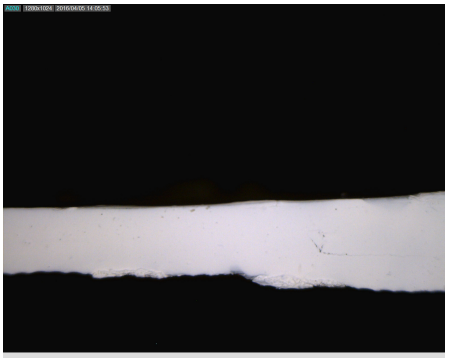

Figure C.13: Specimen at 2.9 mm displacement.

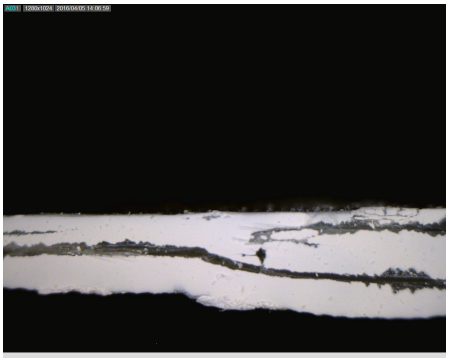

Figure C.14: Specimen at 3.0 mm displacement.

C.3 Test 1-3-2_3

Figure C.15: Top picture is front view and bottom picture is back view of specimen 1-3-2_3 after testing has been performed.

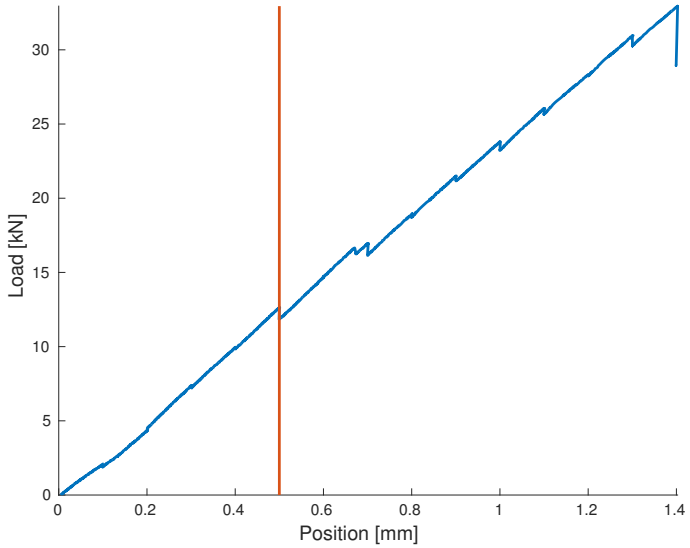

Figure C.16: Load displacement curve for the test. The vertical red line indicates the first observed crack.

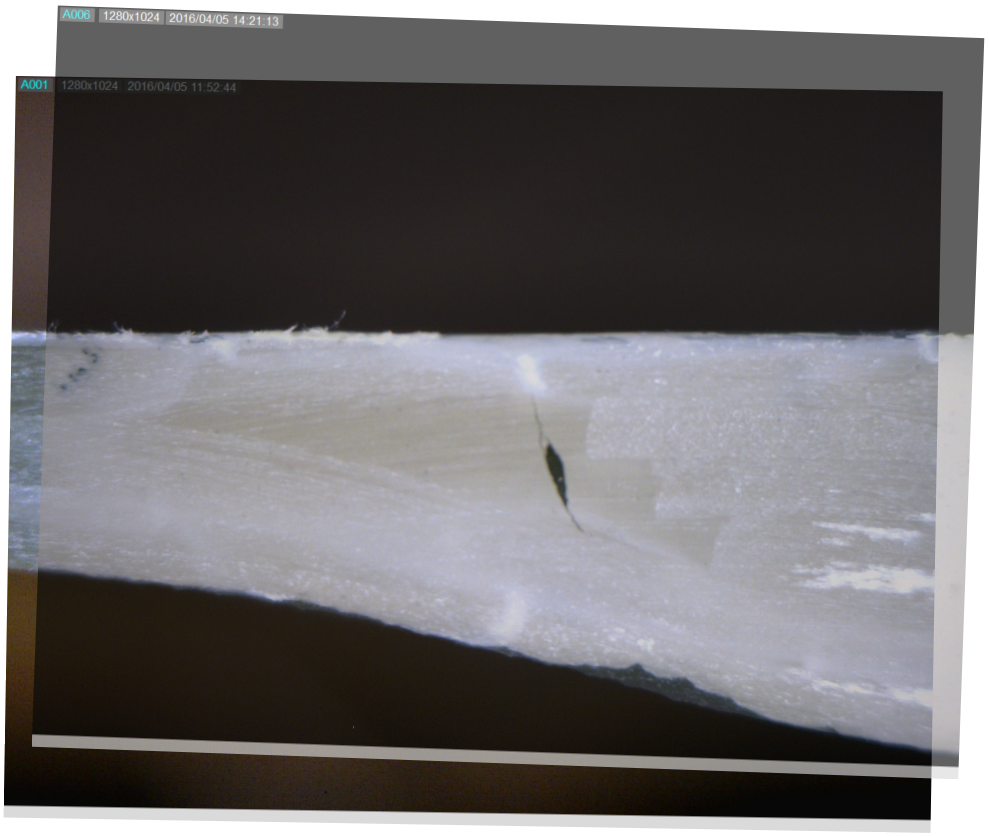

Figure C.17: Picture with cracks overlayed on the unpainted specimen. A crack is seen a little ahead of the dropped plies.

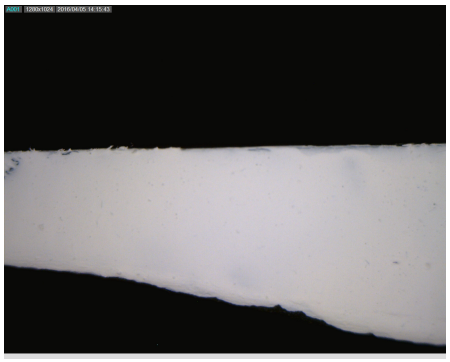

Figure C.18: Specimen at 0.1 mm displacement.

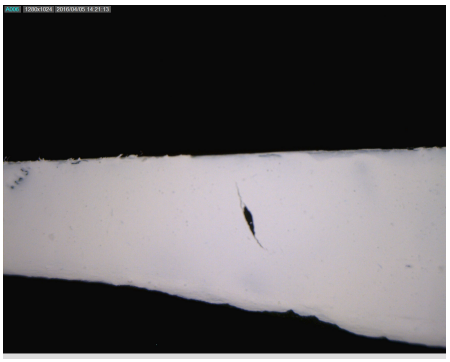

Figure C.19: Specimen at 0.6 mm displacement.

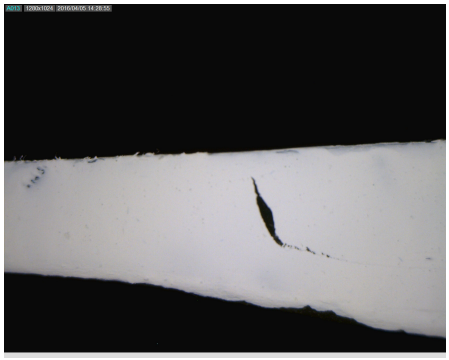

Figure C.20: Specimen at 1.3 mm displacement.

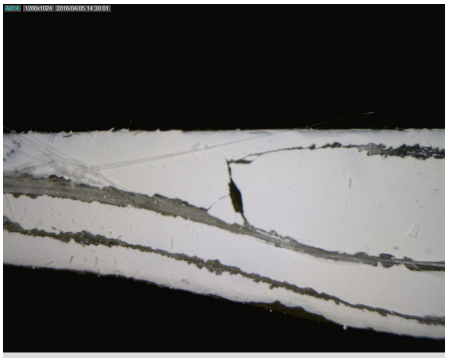

Figure C.21: Specimen at 1.4 mm displacement.

C.4 Test 1-3-2_4

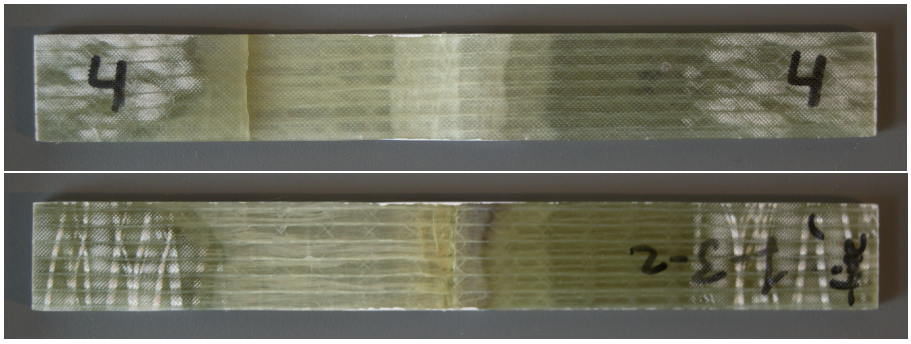

Figure C.22: Top picture is front view and bottom picture is back view of specimen 1-3-2_4 after testing has been performed.

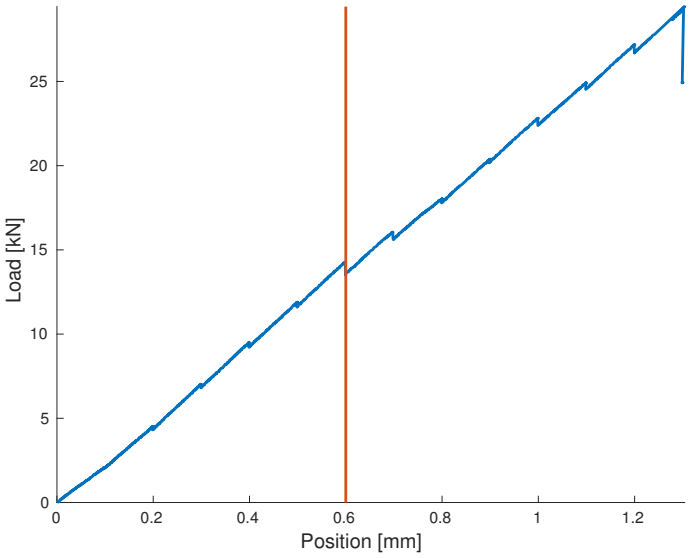

Figure C.23: Load displacement curve for the test. The vertical red line indicates the first observed crack.

Figure C.24: Picture with cracks overlayed on the unpainted specimen. A crack is seen a little ahead of the dropped plies.

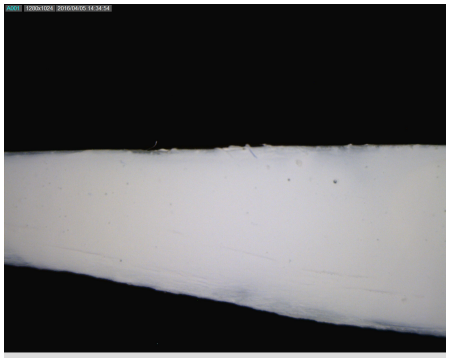

Figure C.25: Specimen in unloaded state.

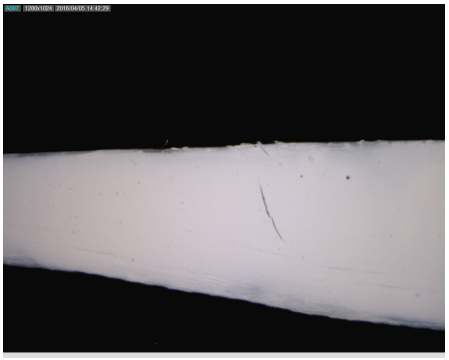

Figure C.26: Specimen at 0.6 mm displacement.

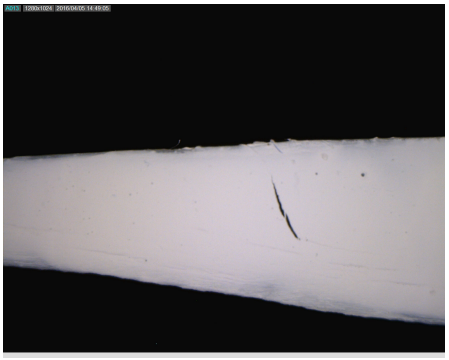

Figure C.27: Specimen at 1.2 mm displacement.

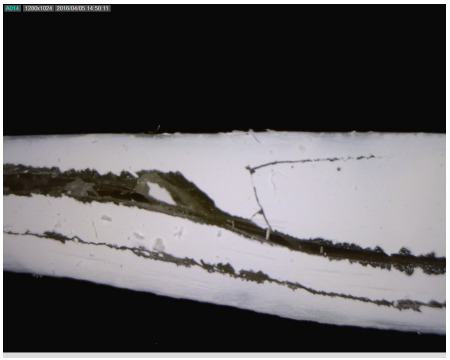

Figure C.28: Specimen at 1.3 mm displacement.

C.5 Test 7-1-1_5

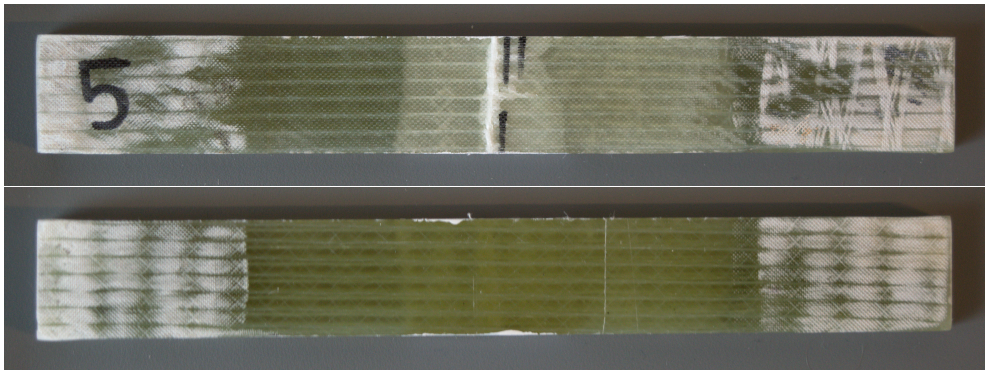

Figure C.29: Top picture is front view and bottom picture is back view of specimen 7-1-1_5 after testing has been performed.

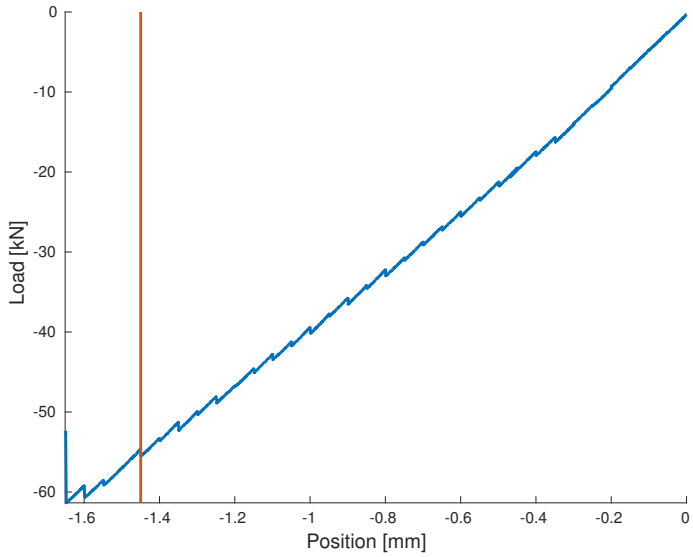

Figure C.30: Load displacement curve for the test. The vertical red line indicates the first observed crack.

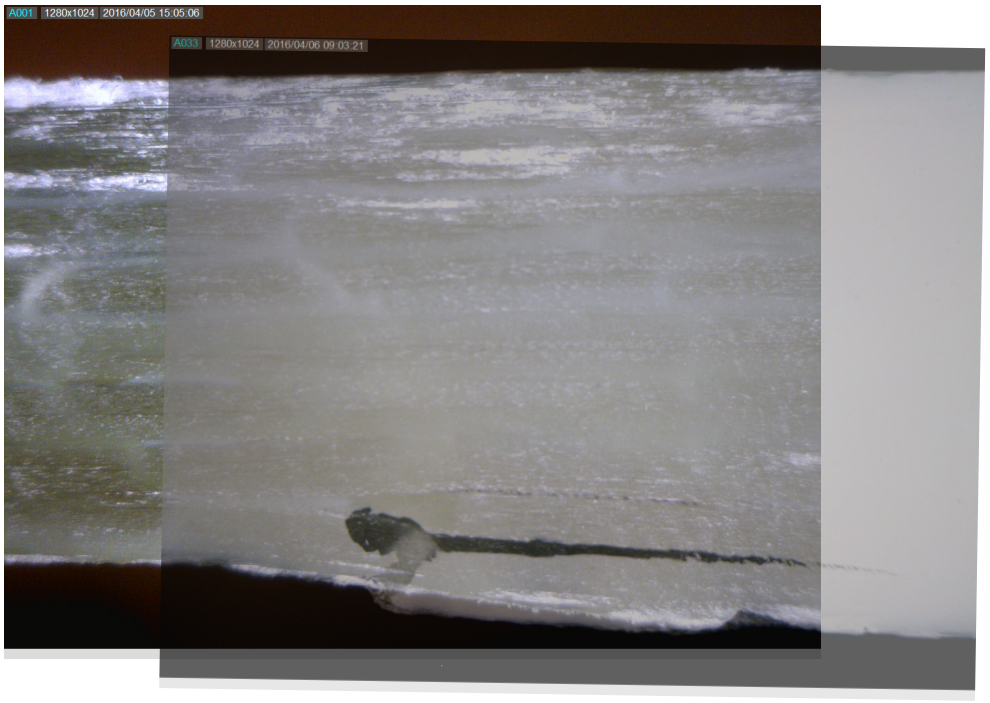

Figure C.31: Picture with cracks overlayed on the unpainted specimen. Delamination is seen between the top and dropped ply. A crack is also seen below the dropped ply. A kinkband is seen in the top layer.

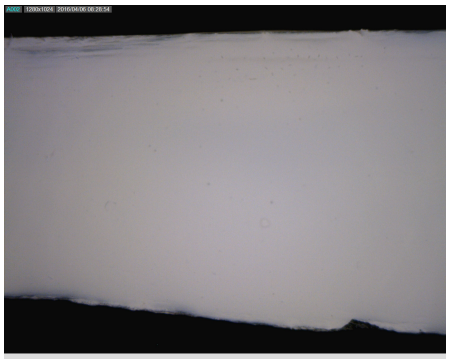

Figure C.32: Specimen in unloaded state.

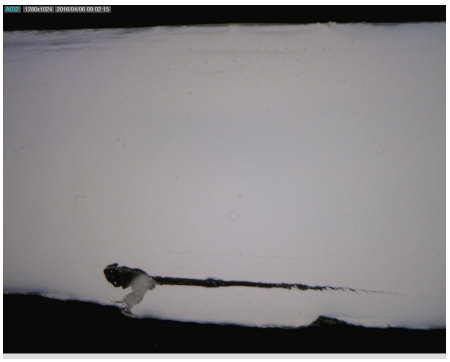

Figure C.33: Specimen at 1.5 mm displacement.

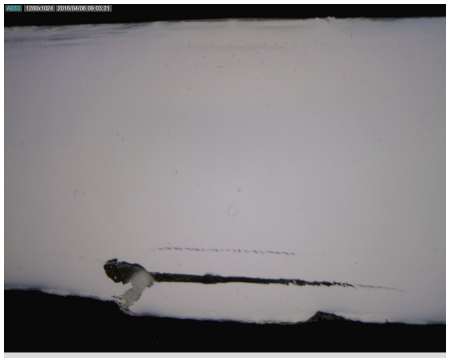

Figure C.34: Specimen at 1.55 mm displacement.

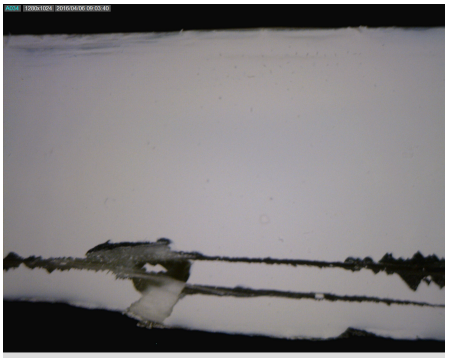

Figure C.35: Specimen at 1.6 mm displacement.

C.6 Test 7-1-1_6

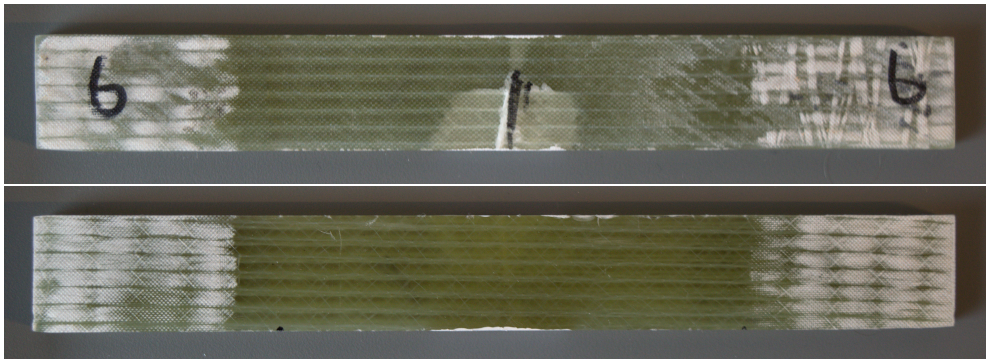

Figure C.36: Top picture is front view and bottom picture is back view of specimen 7-1-1_6 after testing has been performed.

The crack appeared opposite of the camera and has therefore not been captured

C.7 Test 7-1-1_7

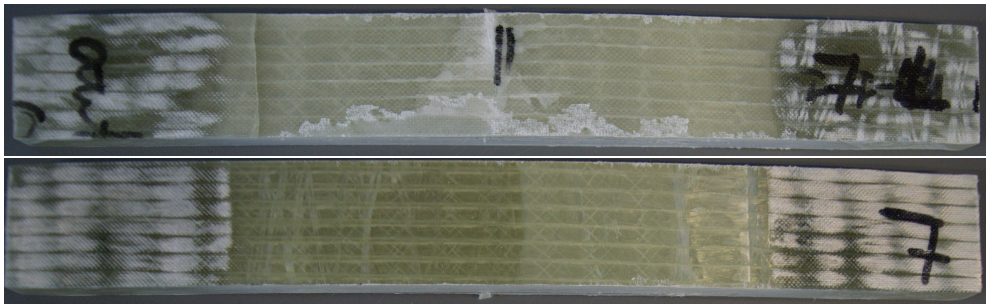

Figure C.37: Top picture is front view and bottom picture is back view of specimen 7-1-1_7 after testing has been performed. The white regions are remains from spray paint.

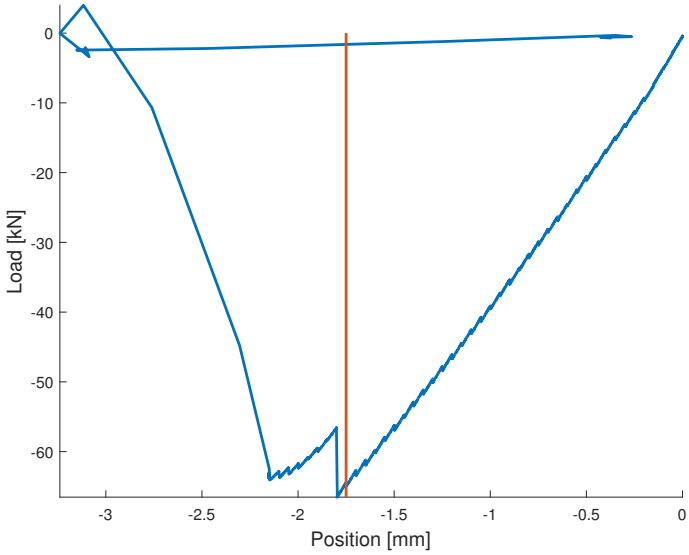

Figure C.38: Load displacement curve for the test. The vertical red line indicates the first observed crack.

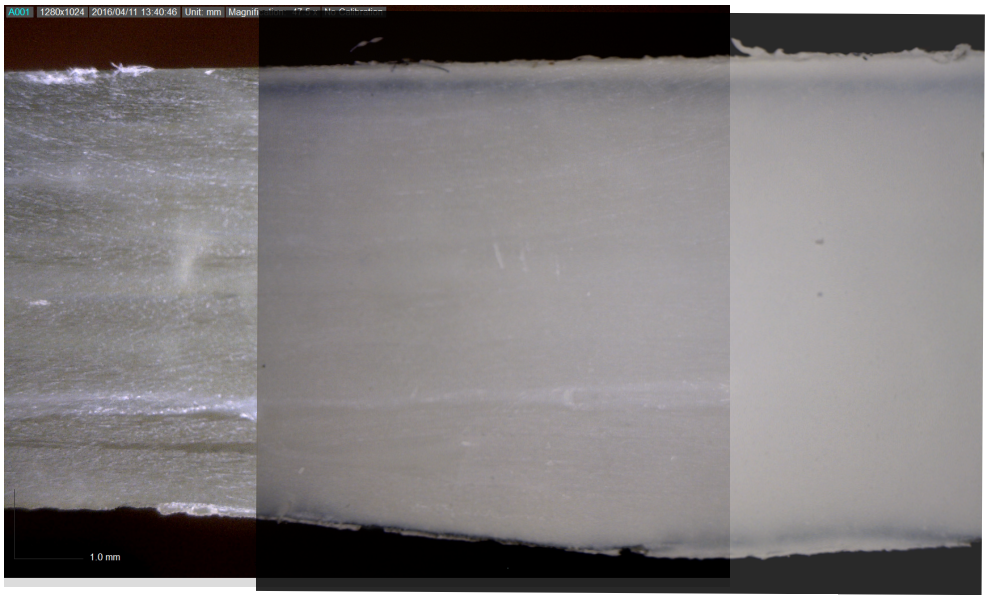

Figure C.39: Picture with cracks overlayed on the unpainted specimen. A crack is seen below the dropped ply. This happens at displacement 1.75 mm .

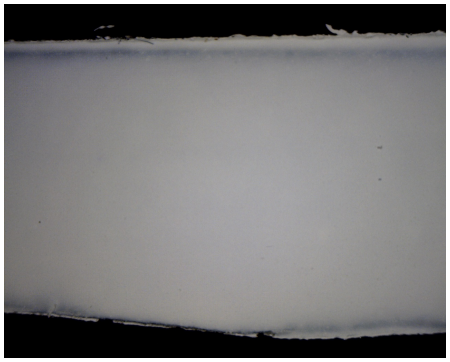

Figure C.40: Specimen in unloaded state.

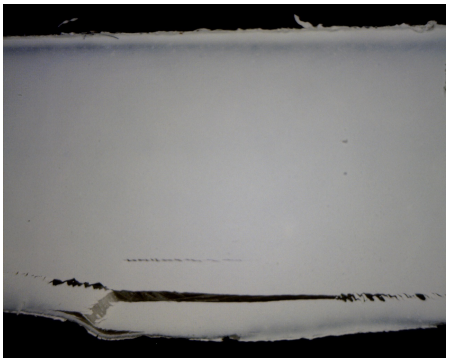

Figure C.41: Specimen at 1.8 mm displacement.

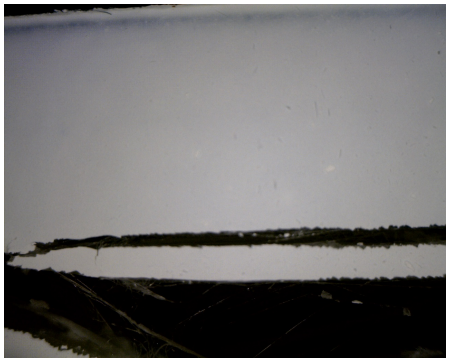

Figure C.42: Specimen at 2.0 mm displacement. Notice the specimen has started to buckle. It can also be seen in the load-displacement curve.

Figure C.43: Specimen at 2.2 mm displacement. Delamination in all layers.

C.8 Test 1-1-1_8

Figure C.44: Top picture is front view and bottom picture is back view of specimen 1-1-1_8 after testing has been performed. Fibre breaking has occurred close to the grips.

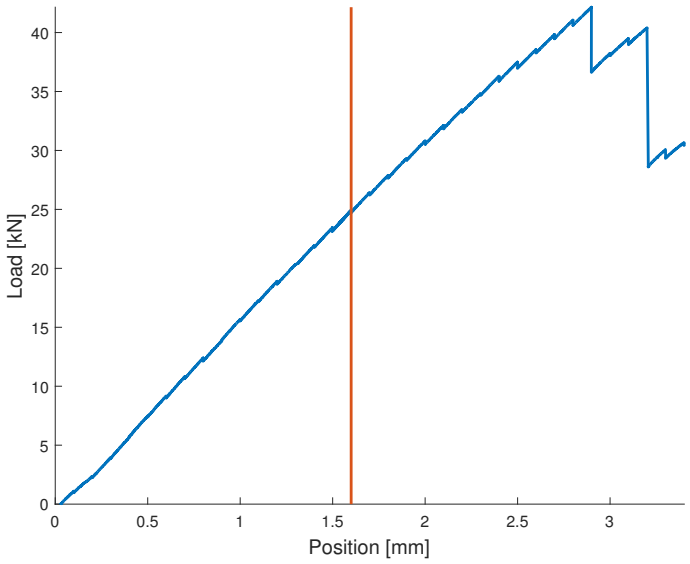

Figure C.45: Load displacement curve for the test. The vertical red line indicates the first observed crack.

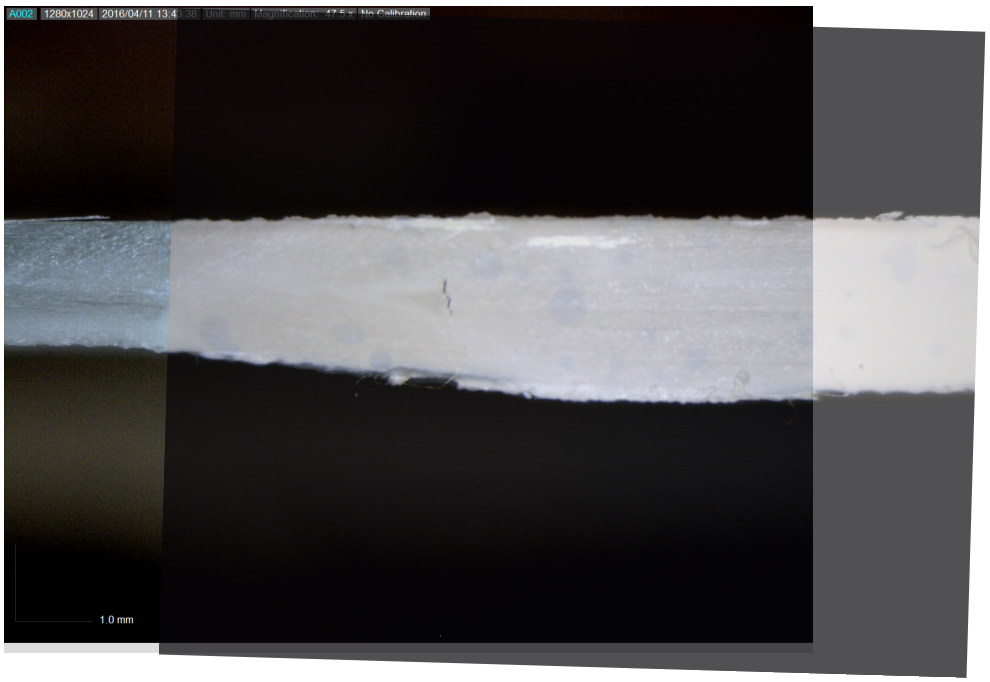

Figure C.46: Picture with cracks overlayed on the unpainted specimen. A crack is seen in front of the dropped ply.

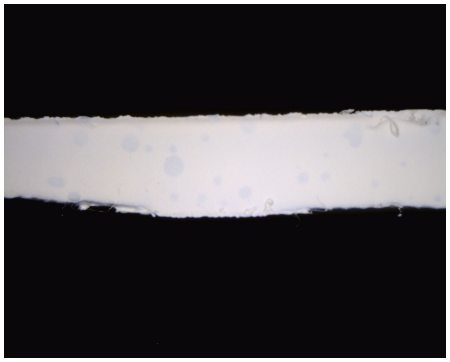

Figure C.47: Specimen in unloaded state.

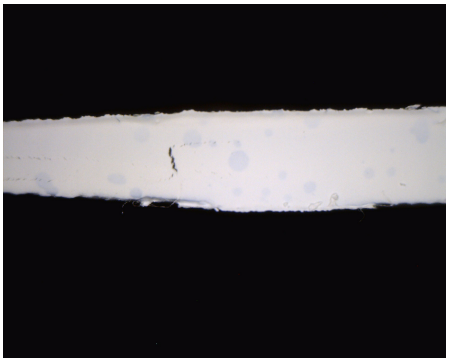

Figure C.48: Specimen at 2.8 mm displacement.

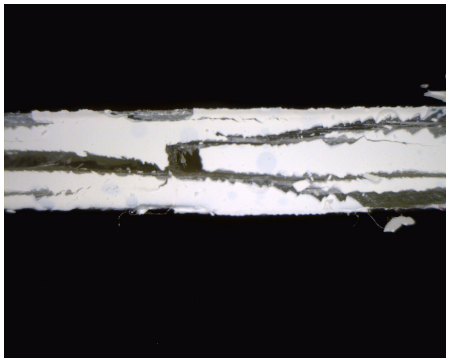

Figure C.49: Specimen at 2.9 mm displacement.

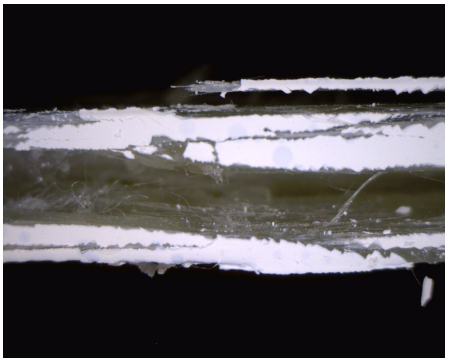

Figure C.50: Specimen at 3.3 mm displacement.

C.9 Test 1-1-1_9

Figure C.51: Top picture is front view and bottom picture is back view of specimen 1-1-1_9 after testing has been performed. The white regions are remains from spray paint.

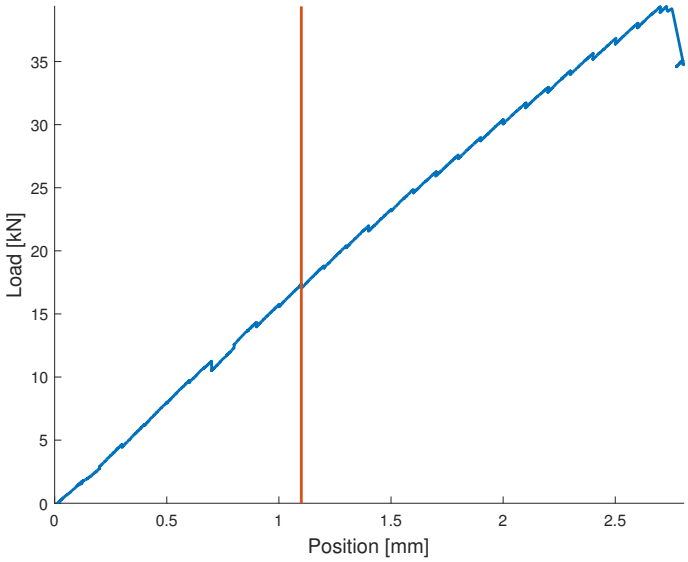

Figure C.52: Load displacement curve for the test. The vertical red line indicates the first observed crack.

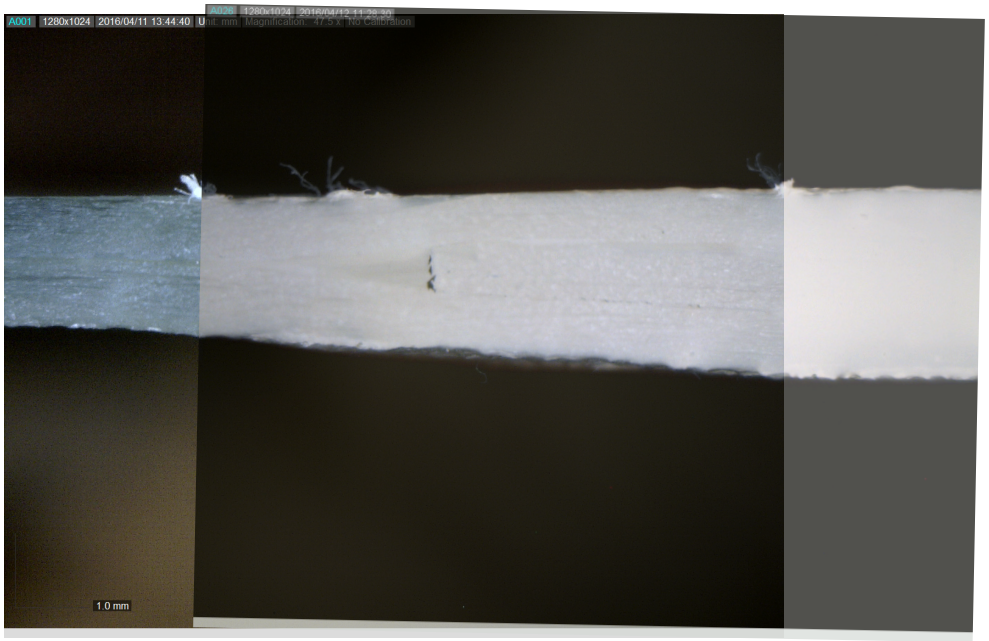

Figure C.53: Picture with cracks overlayed on the unpainted specimen. A crack is seen in front of the dropped ply.

Figure C.54: Specimen in unloaded state.

Figure C.55: Specimen at 1.7 mm displacement.

Figure C.56: Specimen at 2.5 mm displacement.

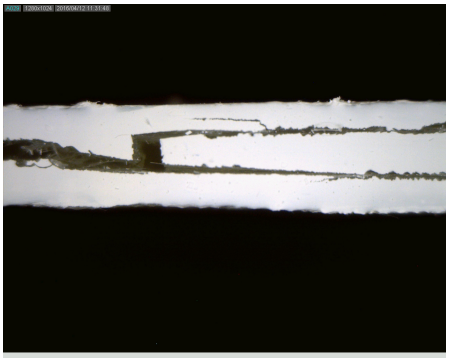

Figure C.57: Specimen at 2.8 mm displacement.

Digital Image Correlation

D

This appendix contains the DIC measurements of a ply-drop loaded with a 10363 N force. The images has been treated using the open source software NCORR.

D.1 Longitudinal Displacement

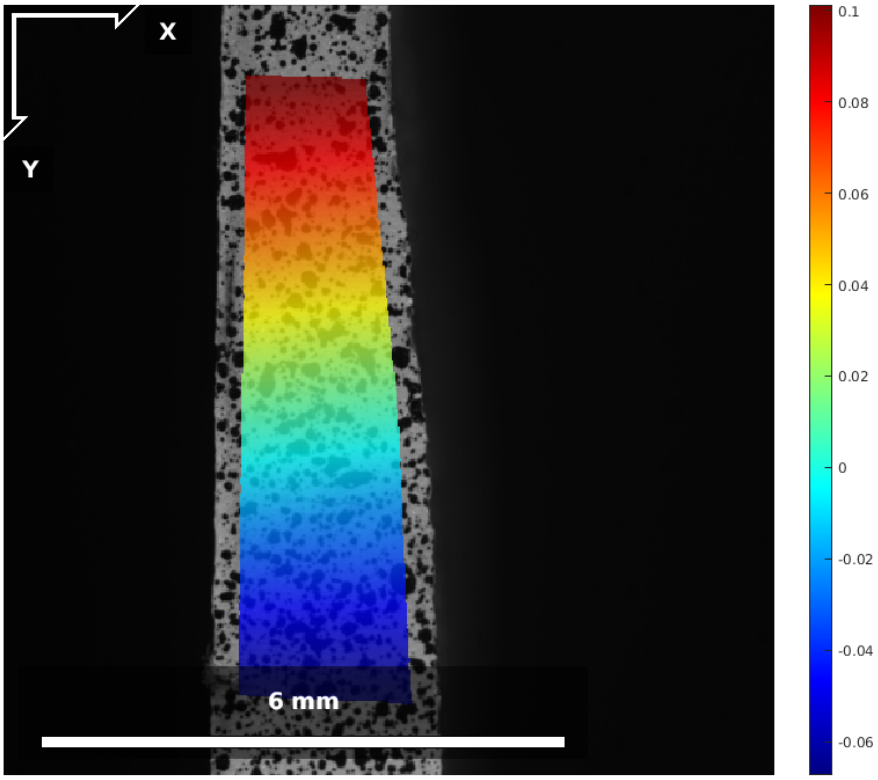

Type: u-plot
Reference Name: d2-brud_0.tiff
Current Name: d2-brud_2.tiff
Analysis type: regular
RG-DIC Radius: 40 | Subset Spacing: 3
Diffnorm Cutoff: 1e-06 | Iteration Cutoff: 50 | Threads: 2
Step Analysis: Disabled
RG-DIC Subset Truncation: Disabled
Image Correspondences: [0 6]
Units/pixels: 0.0043113 mm/pixels
Correlation Coefficient Cutoff: 0.1585
Radial Lens Distortion Coefficient: 0
Max: 0.1047 mm | Median: 0.0068 mm | Min: -0.0703 mm

Figure D.1: Longitudinal displacement for load 10363 [N]

D.2 Transverse Displacement

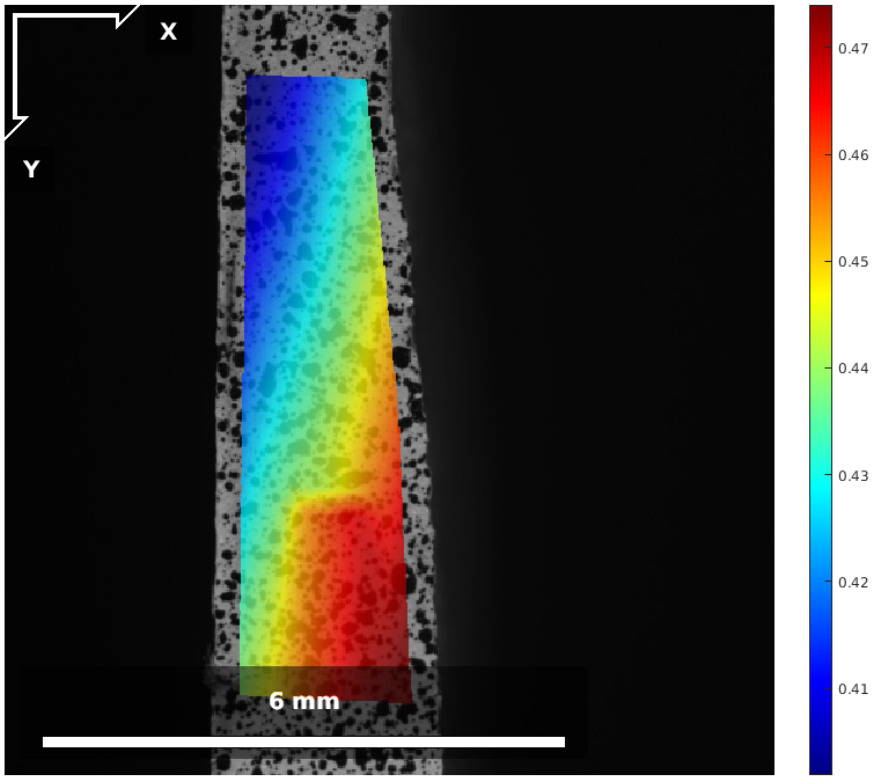

Type: v-plot
Reference Name: d2-brud_0.tiff
Current Name: d2-brud_2.tiff
Analysis type: regular
RG-DIC Radius: 40 | Subset Spacing: 3
Diffnorm Cutoff: 1e-06 | Iteration Cutoff: 50 | Threads: 2
Step Analysis: Disabled
RG-DIC Subset Truncation: Disabled
Image Correspondences: [0 6]
Units/pixels: 0.0043113 mm/pixels
Correlation Coefficient Cutoff: 0.1585
Radial Lens Distortion Coefficient: 0
Max: 0.4785 mm | Median: 0.4387 mm | Min: 0.3966 mm

Figure D.2: Transverse displacement for load 10363 [N]

D.3 Longitudinal Strain

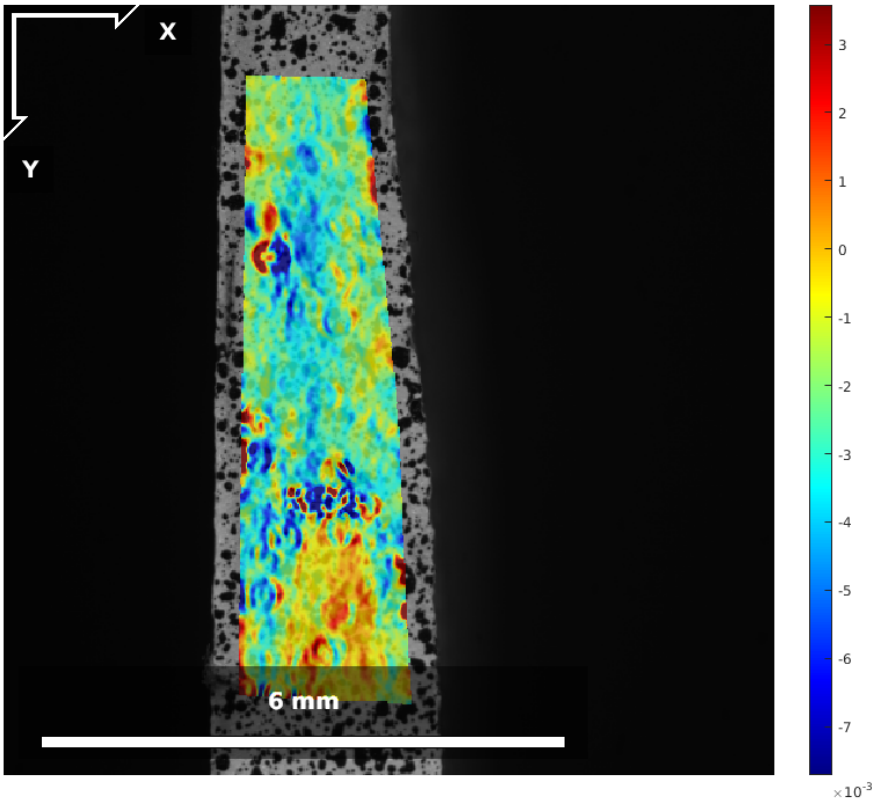

Type: exx-plot
Reference Name: d2-brud_0.tiff
Current Name: d2-brud_2.tiff
Analysis type: regular
RG-DIC Radius: 40 | Strain Radius: 3 | Subset Spacing: 3
Diffnorm Cutoff: 1e-06 | Iteration Cutoff: 50 | Threads: 2
Step Analysis: Disabled
RG-DIC Subset Truncation: Disabled | Strain Subset Truncation: Disabled
Image Correspondences: [0 6]
Units/pixels: 0.0043113 mm/pixels
Correlation Coefficient Cutoff: 0.1585
Radial Lens Distortion Coefficient: 0
Max: 0.0224 | Median: -0.0022 | Min: -0.0167

Figure D.3: Longitudinal strain for load 10363 [N]

D.4 Transverse Displacement

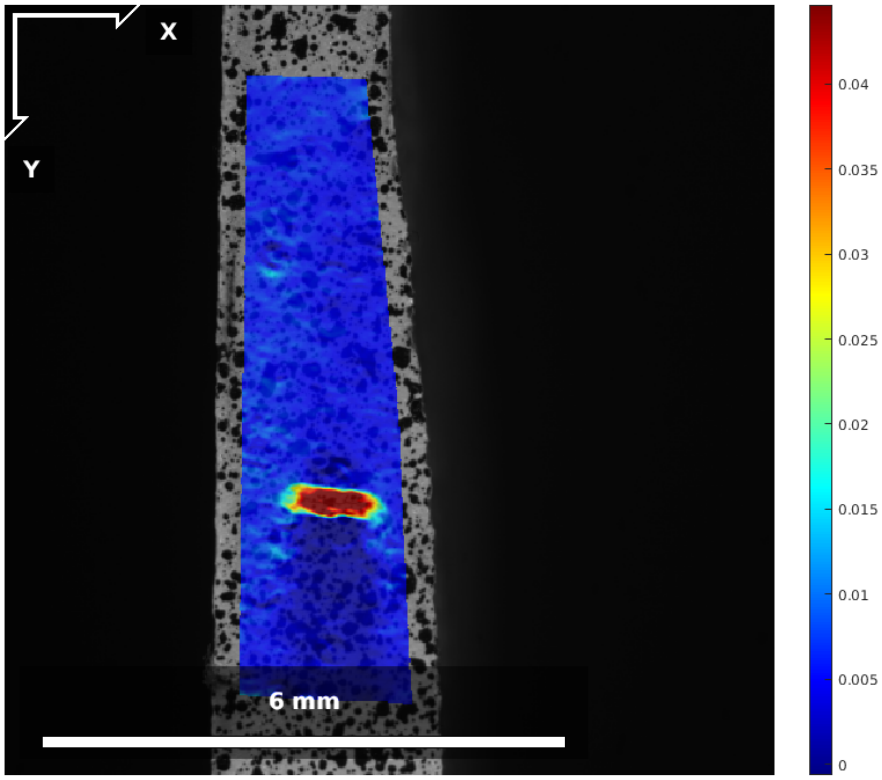

Type: eyy-plot
Reference Name: d2-brud_0.tiff
Current Name: d2-brud_2.tiff
Analysis type: regular
RG-DIC Radius: 40 | Strain Radius: 3 | Subset Spacing: 3
Diffnorm Cutoff: 1e-06 | Iteration Cutoff: 50 | Threads: 2
Step Analysis: Disabled
RG-DIC Subset Truncation: Disabled | Strain Subset Truncation: Disabled
Image Correspondences: [0 6]
Units/pixels: 0.0043113 mm/pixels
Correlation Coefficient Cutoff: 0.1585
Radial Lens Distortion Coefficient: 0
Max: 0.0689 | Median: 0.0052 | Min: -0.0076

Figure D.4: Transverse strain for load 10363 [N]

D.5 Shear Strain

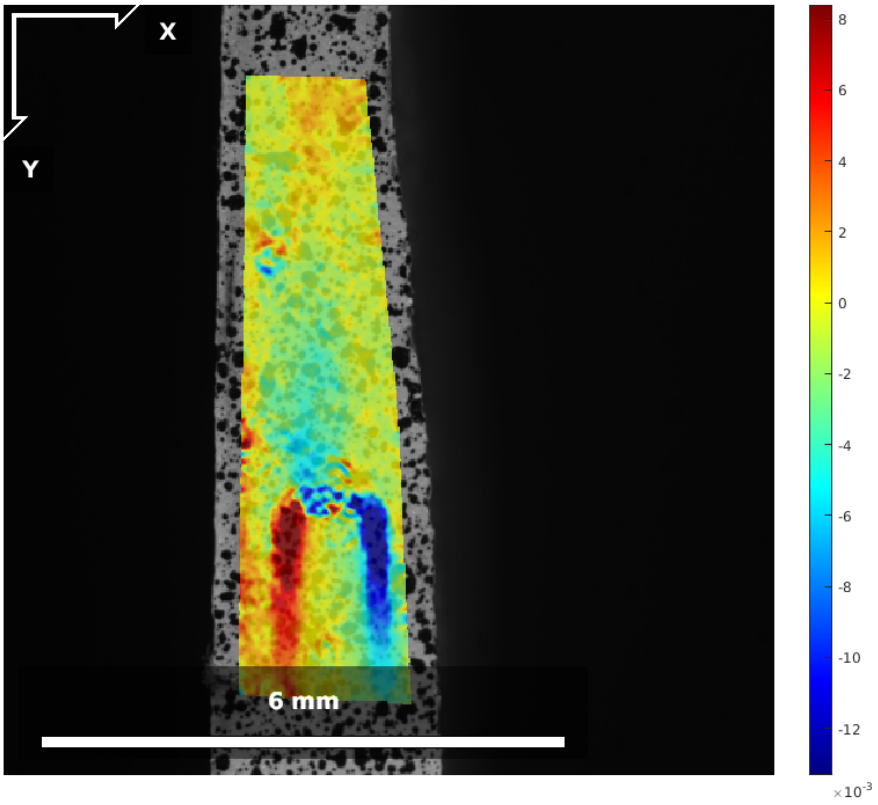

Type: exy-plot
Reference Name: d2-brud_0.tiff
Current Name: d2-brud_2.tiff
Analysis type: regular
RG-DIC Radius: 40 | Strain Radius: 3 | Subset Spacing: 3
Diffnorm Cutoff: 1e-06 | Iteration Cutoff: 50 | Threads: 2
Step Analysis: Disabled
RG-DIC Subset Truncation: Disabled | Strain Subset Truncation: Disabled
Image Correspondences: [0 6]
Units/pixels: 0.0043113 mm/pixels
Correlation Coefficient Cutoff: 0.1585
Radial Lens Distortion Coefficient: 0
Max: 0.0168 | Median: -0.0008 | Min: -0.0186

Figure D.5: Shear strain for load 10363 [N]